PETER AZOR OKORUGBO

EFFECT OF IMPACT VELOCITY ON THE ENERGY ABSORPTION CHARACTERISTICS OF CRASH BOXES

NEU 2019

EFFECT OF IMPACT VELOCITY ON THE ENERGY ABSORPTION CHARACTERISTICS OF CRASH BOXES.

A THESIS SUBMITTED TO THE GRADUATE SCHOOL OF APPLIED SCIENCES

OF

NEAR EAST UNIVERSITY

By

PETER AZOR OKORUGBO

In Partial Fulfillment of the Requirements for

the Degree of Master of Science

in

Mechanical Engineering

NICOSIA, 2019

EFFECT OF IMPACT VELOCITY ON THE ENERGY ABSORPTION CHARACTERISTICS OF CRASH BOXES.

A THESIS SUBMITTED TO THE GRADUATE SCHOOL OF APPLIED SCIENCES

OF

NEAR EAST UNIVERSITY

By

PETER AZOR OKORUGBO

In Partial Fulfillment of the Requirements for the Degree of Master of Science

in

Mechanical Engineering

NICOSIA, 2019

Peter Azor OKORUGBO: EFFECT OF IMPACT VELOCITY ON THE ENERGY ABSORPTION CHARACTERISTICS OF CRASH BOXES.

Approval of Director of Graduate School of

Applied Sciences

Prof. Dr. Nadire ÇAVUŞ

We certify this thesis is satisfactory for the award of the degree of

Masters of Science in Mechanical Engineering

Examining Committee in Charge:

Prof. Dr. Yusuf Şahin	Committee Chairman, Department of Mechanical Engineering, NEU
Prof. Dr. Mahmut Ahsen Savaş	Co-Supervisor, Department of Mechanical Engineering, NEU
Assoc. Prof. Dr. Fa'eq Radwan	Department of Biomedical Engineering, NEU
Assoc. Prof. Dr. Kamil Dimililer	Department of Automotive Engineering, NEU
Assist. Prof. Dr. Ali Evcil	Supervisor, Mechanical Engineering Department, NEU

I hereby declare that all information in this document has been obtained and presented in accordance with academic rules and ethical conduct. I also declare that, as required by these rules and conduct, I have fully cited and referenced all material and results that are not original to this work

Name, last name: Peter Azor Okorugbo

Signature:

Date:

ACKNOWLEDGEMENTS

The success of this thesis is due to the immeasurable support of my principal supervisor Assist. Prof. Dr. Ali Evcil; and co-supervisor Prof. Dr. Mahmut Ahsen Savaş whose guidance, patience and instructions has yielded this work.

Not forgetting to acknowledge the effort of Prof. Dr. Mehmet Ali Guler, Assist. Prof. Dr. Ing Hüseyin Camur who endlessly and tireless made themselves available to give me instructions as needed through the period of my study and this work.

And most importantly, I want to appreciate my Family in Nigeria and Cyprus for their love, support and encouraging words that kept me going all through the process of this study. I'm greatly indebted to my Parents **Captain and Mrs. Amos Azor Okorugbo** for their unending love and supports all through the period of my study. I would like to thank my Fathers in the Faith Apostle Sylvester Newman Bebenimibo and Apostle Dr. Ifeanyi Obi for their prayers and encouragements. Not forgetting to appreciate my Pastor in the Person of Pastor Patrick Nonso Nwaogaranya for his counsel, prayers and love in difficult times and also Pastor Princewill Okudah Amarachi you are a gift.

Apparently the list is endless but I want to say thank you to everyone God placed in my life and whose presence in my life has made this work a success, May God Almighty Bless them all.

This research work and experiment was supported by the Department of Mechanical Engineering of the Near East University.

To my parents…

ABSTRACT

The automotive industry has implored the use of thin walled structure known as the crash box to increase the level of safety of passenger vehicles in the event of frontal collision. The crash box is characterized by its progressive folding which absorbs the energy of the collision through its plastic deformation by converting the kinetic energy to plastic strain energy. In this study, the effect of impact velocity on the energy absorption characteristic of four thin-walled square frusta steel specimen used as energy absorbing elements will be numerically analyzed. For each specimen, four runs were made with four different velocity characterizing from low velocity to high velocity. The specimens are impacted axially with a striking mass moving only in the axially direction of the specimens. Assessment of the performance of these specimens are done using five metrics: Energy Absorbed (EA), Specific Energy Absorbed (SEA), Initial Peak Force (IPF), Mean Load (P_{mean}), and Crush Force Efficiency (CFE). The results shows that as the velocity increases the initial peak force increases and the energy absorption increases alongside while crush force efficiency decreases at high impact velocity. The quasi-static analysis is done using LS-Dyna.

Keywords: Automotive; crash box; crashworthiness; energy; LS-Dyna; safety; thin-walled structure.

ÖZET

Otomotiv endüstrisinde yolcu güvenliğini artırmak amacı ile araçların ön kısımlarında darbe emiciler kullanılmakta ve geliştirilmektedir. Darbe emiciler ince cidarlı yapılar olup çarpışmadan kaynaklanan enerji transferini kademeli olarak plastik deformasyona uğrayarak emme prensibi ile çalışırlar. Bu çalışmada çarpma hızının enerji emiş karakterine olan etkisi dört farklı konik çelik model kullanılarak sayısal olarak incelenmiştir. Her model dört farklı çarpma hızı kullanılarak analiz edilmiştir. Çarpma modeli eksenel olarak hareket eden bir kütlenin numune ile teması sonrası numuneye yapışarak hareket etmesi şeklinde oluşturulmuştur. Numune performansları beş farklı değer ile değerlendirilmişir. Bunlar enerji emilmesi, spesifik enerji emilmesi, en yüksel başlangıç kuvveti, ortalama kuvvet ve ezme kuvveti verilmliliği olarak sıralanabilir.Sonuçlar çarpma hızının artması ile en yüksek başlangıç kuvvetinin ve enerji emilişinin arttığını ancak ezme kuvveti verimliliğinin azaldığını göstermektedir. Analizler LS-Dyna yazılımı ile gerçekleştirilmiştir.

Anahtar Kelimeler: Çarpışma dayanıklılığı; darbe emici; enerji; güvenlik; ince cidarlı yapı; LS-Dyna; otomotiv.

TABLE OF CONTENTS

LIST OF TABLES

LIST OF FIGURES

CHAPTER 1
INTRODUCTION

1.1.General Information

According to the 2018 edition of global status report on road safety launched by the World Health Organization, statistical report shows that about 1.35 million deaths were recorded annually as a result of road traffic accident (world health organızatıon , 2019).

The automotive industry which is one of the largest and fastest growing industries in the world today is constantly reaching out to increasing the level of safety of each vehicle produced. Manufacturers and passengers are having increasing concerns about the safety of automobiles. In order to assess the safety of vehicles often times the Insurance Institute for Highway Safety (IIHS) and National Highway Traffic Safety Administration (Euro-NCAP) carry out regulations for safety and one of these regulations require that the vehicle undergo a crash test, and it involves both low and high velocity tests.

The low velocity test is conducted to examine damages done to the car while the high velocity test is useful in assessing the effect of crash on humans. Crash tests are usually conducted to assess the deformation of the chassis of a vehicle as well as the energy absorbing elements such as the crash box.

The crash box absorbs crash energy by undergoing plastic deformation axially in the case of frontal collision. Plastic deformation is benefiting for the purpose of reducing the force transmitted to the passenger compartment of the vehicles thereby improving the safety of the vehicle (Y Nakazawa, 2005).

The scope of this project is to observe and analyze how crash boxes perform under low speed and high speed crushing. The parameters used to characterize the performance are the specific absorbed energy, the impulse on the crash box, initial peak force, crush force efficiency. This analysis is done by fixing one end of the crash box and allowing a striker mass limited to translational motion in the axial direction of the crash box to simulate a frontal collision of the crash box.

The crash box is usually positioned at the front of the chassis of the vehicle as shown in Figure 1.1 below.

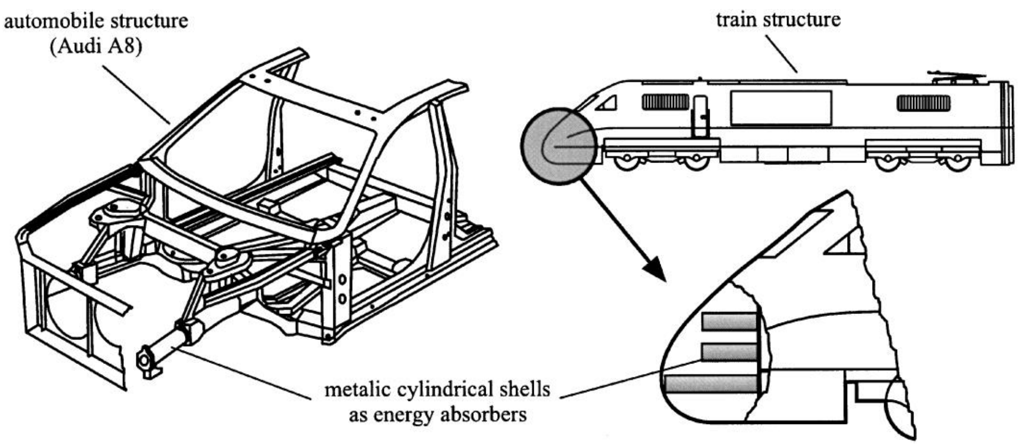

Figure 1. 1: Position of energy absorbing element in a vehicle

1.2. Brief History of the Developments in Automotive Safety

The first recorded fatal car crash dates back to the 18th century in Ireland, they've been other claims of earlier dates of crashes but they were disputed therefore are not officially accepted as the first recorded fatal car crash. The accident in Ireland was recorded as the first because of the fact that safety development was introduced after the crash.

In the year 1922, vehicles were then being fitted with braking systems. Seat belts was introduced in vehicles in the year 1930 by physicians and surgeons. In the year 1959, seat belts were standardized in Volvo (Crash Test: Vehicle Safety and Accident Prevention, 2019).

1.3.Types of Collision Test

There are basically three (3) major types of collision tests done by vehicle safety assessment programs and these tests are as follows (A.I. RADU, 2015)

1. Axial (Front or Rear) collision test
2. Side collision test
3. Roll over crash test

Frontal Collision test is a vital aspect of the test procedures because according to the ANCAP reports, over 60% of serious crashes are frontal (offset and full width) (ANCAP, 2018). This test is done to simulate head on collision of cars travelling at about 50km/h, (64km/h for offset collision) (ANCAP, 2018) and the effect of this collision on human being is analyzed with the use of dummies placed inside the vehicle and the effect on the car is analyzed visually and also using readings obtained from the sensors placed inside and around the vehicles. Figure 1.2 shown below is an image of a BMW SUV undergoing an full width frontal collision test.

Figure 1. 2: Frontal full width collision test

In Figure 1.3, an offset collision test at the moment of obstacle and car contact is shown from a plan view. This photo is intended to graphically display the setup of a frontal offset collision test.

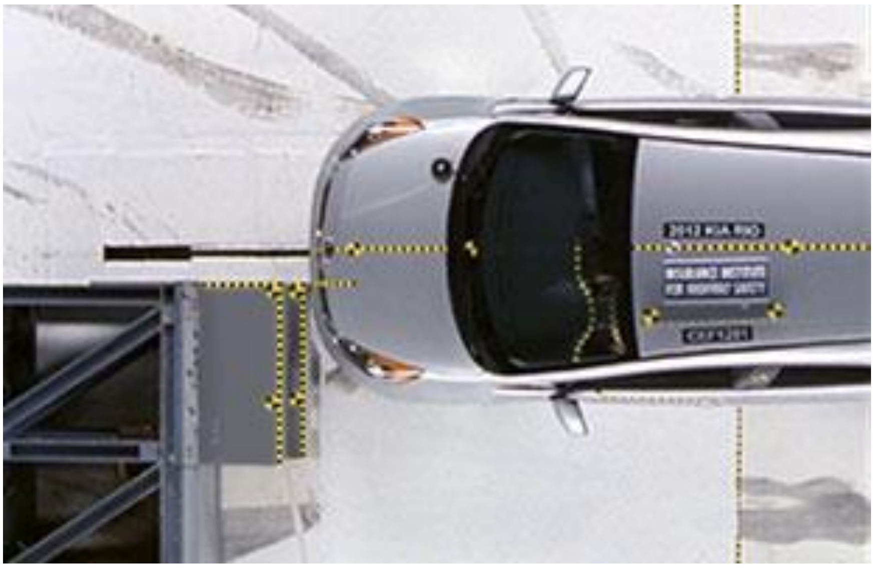

Figure 1. 3: Frontal Offset collision test

The Side impact test is necessary as statistics shows that about 30% of serious crashes are side impacts (ANCAP, 2018). Therefore, the side impact test is done to simulate a collision of two cars perpendicular to each other with one impacted at the side.

Figure 1. 4: Side Collision Test

At the NCAP test center, a trolley of 1300kg moving at the speed of 50km/h is used to impact the side of the vehicle undergoing the test. The New Car Assessment Program (NCAP) has a standard side impact setup shown in Figure 1.4.

The Rollover crash test is needful in the event of a car tip over, this crash test is done to test the structural integrity of the roof of the car in order to determine the level of safety a vehicle occupant can get in the event of a car tipping over so as to minimize compression of the roof on the vehicle occupant. Figure 1.5 illustrates a rollover crash test setup.

Figure 1. 5: Rollover Crash Test

1.4. Literature Review

Literature has shown that several studies has been done by researchers over the years to improve on the designs and manufacturing methodology of crash boxes, and these researches are geared towards obtaining better, lighter and cost effective designs of crash boxes with different geometrical characteristics to better enhance the energy absorption capacity of these energy dissipating elements known as crash boxes.

There are experimental and numerical studies which include dynamic or quasi-static simulations in literatures. However, in studies given in literature, it is observed that the energy absorption characteristics of thin walled structures have a direct link to their cross-sectional area, material property, wall thickness, and corrugations if any.

It is conventional to use thin walled structures for the purpose of crash energy dissipation in automobiles, this thin walled structures are commonly having circular or square cross sections, and they may be either straight or tapered depending on the aim of the researcher. Literature has shown that the focus has recently shifted towards tapered tubes as they appear to serve better in dissipating crash energy as compared to the same tube when not tapered. Tapered tubes perform better than straight tubes both in oblique impact loading as well as axial impact loading. In the study of Nagel and Thambiratnam (G.M Nagel, 2004). They investigated the dynamic energy absorption response of both straight and tapered rectangular tubes under impact loading using FE simulation and it was concluded that tapered tubes have higher advantages in energy absorption than the straight tubes. (Guler et.al, 2010) investigated and compared the crush behavior of tapered and straight tubes with circular, hexagonal and square cross sections concluded from their crush force efficiency curves that the circular cross-sectioned absorber with 12.5 degree semi-apical angle and 2 mm wall thickness is the most efficient absorber. Zhang et.al (Zonghua Zhang, 2011) conducted a numerical study of the crashworthiness of kagome sandwich column under axial crushing and the effects of geometrical parameters, wall interaction, mode of deformation and the energy absorption characteristics were studied and a new concept of honeycomb sandwich column was introduced in their work. Duarte et.al (Isabel Duarte, 2015) evaluated the failure mechanisms, deformation modes and mechanical properties of in-situ foam filled tubes as quasi-static and dynamic axial crush performance using compression tests supported by IR thermography. Costas et.al, 2016 proposes designing crash box using Glass Fiber Reinforced Polymer and polyurethane as a filler material in an aluminum tube and comparison was made on the performances under axial crushing and they observed that there was about a 100%

increase in energy absorption of the PET foam and GFRP filled aluminum tube in comparison to the empty aluminum tube. Tastan et al, 2016 used surrogate models to analyze the energy absorption capabilities of thin walled structures and multi objective optimization was used to determine the local and global geometrical properties of tapered tubes with lateral cutouts for maximum crush force efficiency and specific energy absorption and to identify the effect of having lateral cutouts on crash boxes. Zhu et.al, 2017 conducted simulations to investigate the collapse behavior of thin walled tube filled with CFRP in two inner reinforcements and they investigated the crashworthiness advantages of having two inner reinforced thin walled tube. Alkhatib et.al, 2017 conducted a numerical study of the collapse behavior and energy absorption performance of corrugated tapered tubes with circular cross section and concluded that the main influencer of the characteristics of the force to displacement curve was the amplitude of the corrugations which was benefitting in decreasing the initial peak force but at the cost of reducing the specific energy absorbed. Mahshid Mahbod, 2018 studied the effect of corrugations on composite tubes under axial and oblique loading conditions and concluded that corrugated composite tubes possess superior crushing characteristics when compared to cylindrical tubes and they highlighted that the corrugation on the tubes increased the crush force efficiency significantly both in the axial and oblique loading condition. Mamalis et.al, 2001 used finite element simulations to compare results obtained from experimentally crushing a mild steel with 4 distinct geometrical parameters, they observed that the finite element model was able to capture the collapse mode and characteristics of the experimental square frusta. Altin et.al, 2017 investigated the effect of the combination of cross section, taper angle and cell structure on the crashworthiness of multicell tubes. Literature showed that they've been little or no work done related to the effect of velocity on the energy absorption performance of thin walled tubes.

In this project, the effect of velocity on the energy absorption of 4 specimen of mild steel having 4 different taper angle will be investigated numerically. A finite element computer generated models with the validation study done using already existing geometrical parameters from the work done by Mamalis et.al, 2001.

1.5. Thesis Overview

This thesis has 7 chapters; Chapter 1 deals with the introduction of the work. The definition and aim of the thesis is outlined and a brief literature review of the work is discussed. Chapter 2 deliberates on an overview of crash box design. Chapter 3 deals with the modelling and the interpretation of parameters used in this study. Chapter 4 is dedicated to the validation of crash box models. Chapter 5 gives an extensive analysis of the present study. Chapter 6 is deals with result and discussion while Chapter 7 is dedicated to the conclusion of this study.

CHAPTER 2
OVERVIEW OF CRASH BOX DESIGN

Crash boxes are known for their progressive deformation pattern and large energy absorption under impact loading. This project is intended to investigate the effect of impact velocity on the energy absorption characteristics of thin-walled conical columns used as energy absorption elements in the automotive industry. Although there have been quite a number of studies relating to axial crushing behavior of conical crash box for a specific desired crashing performance but the effect of velocity on the energy absorption capacity of crash boxes were not specifically studied. In order to investigate this behavior due to velocity, the Specific Energy Absorption (SEA), Crush Force Efficiency (CFE) and Peak Load will be analyzed and optimized by varying the velocity from low to high impact velocity.

The objective of this project is to investigate the performance of the thin-walled tubes used as energy absorbing elements under different velocity conditions. The specimens are obtained from the work of Mamalis et.al, 2001. Therefore this project gained from the work done in the literature.

On 26 February 1980 was the first patent of the crash box published. The patent for deformable impact absorbing device was awarded to Tomoyuki Hirano, Akira Yamanaka, Koichi Tonai (Mitsubishi Jidosha Kogyo Kabushiki Kaisha). The patented crash box is shown in Figure 2.1.

In the quest to produce safer cars, car manufacturers always seek out the best design parameters for energy absorbers. This quest causes manufacturers to look out for research materials done by diverse researchers in different aspects of the vast array of this topic. The crash box topic has proven to be a topic of interest as there are many studies related to this field and these studies independently covers different materials and different shapes that give best performance in absorbing crash energy.

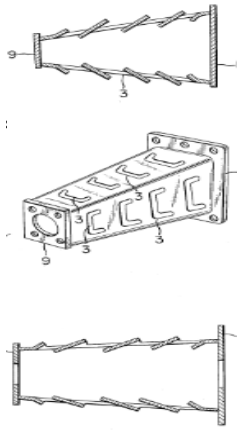

Figure 2. 1: Patented Crash Box (U.S.A Patent No. 4 190 276, 1980)

There are different types of energy absorber designed over the years but in the Figure 2.2 below there is a graphical representation of basic four types of energy absorbers as found in literature.

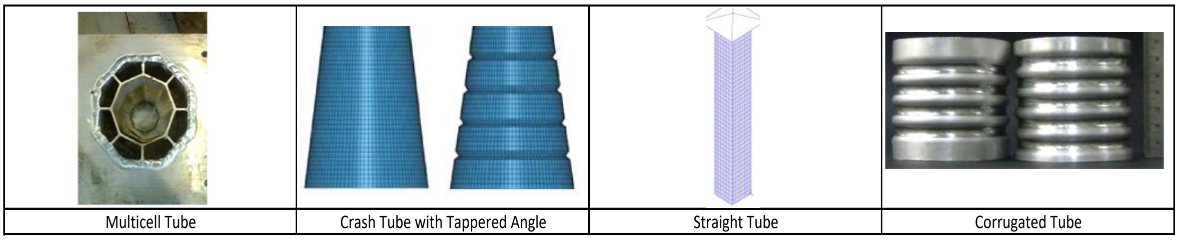

Figure 2. 2: Basic Types of Energy Absorbers (E. Acar, 2011)

2.1 Finite Element Method

There are 3 major field in mechanics that involves calculations. Furthermore, Solid and Structures are divided into 2. Finite Element Method is a linear static calculation. Finite element method is used to determine the stress distribution patterns on solids.

Finite Element Method is generally governed by the equation characterized by hooks law as shown below in Equation 2.1.

$$[f] = [K]\{u\} \tag{2.1}$$

The finite element method is often used to obtain an approximate result similar to results obtained in experiments. The finite element method gains its name from dividing a solid parts into finite smaller sections known as elements. It is a common knowledge and practice that a finer mesh gives more accurate results.

Finite element method provide solutions either through implicit approach or explicit approach. Problems involving dynamic motions are solved using the explicit approach, examples of such problems include

1. Crash test
2. Shock
3. Explosion

While the Implicit approach is used to solve static and quasi-static problems. Just as the names implies, static problems are problems with relatively low velocity in comparison with dynamic problems. Therefore, the major difference between implicit and explicit approach in solving Finite Element Method problems is the acceleration or velocity of the body in question.

The explicit approach is characterized by Equation 2.2 below while the implicit approach is characterized by Equation 2.3.

$$F\big(y(t)\big) = y(t + \Delta t) \tag{2.2}$$

$$F\big(y(t), y(t + \Delta t)\big) = 0 \tag{2.3}$$

2.2 Hypermesh

As mentioned in chapter 2, Hypermesh gains its relevance in converting solid 3D models into Finite Element Meshes by dividing the solid part into small parts. The quality of the mesh determines the degree of accuracy of the results of finite element analysis in simulations. The quality of mesh is determined by some criteria such as the aspect ratio of the meshes, the warpage and the geometry clean up.

2.2.1 Geometry clean up

It is important to erase every form of unneeded parts and edges in a finite element model because if the geometry is not cleaned up, it may affect the running time adversely. Figure 3.3 graphically explains areas where finer meshes are needed. Too much smaller meshes than needed will cause an increase in the running time while a lesser amount of larger meshes might negatively affect the accuracy of the result. Therefore, it is a matter of experience and good knowledge to know when and where finer meshes are necessary.

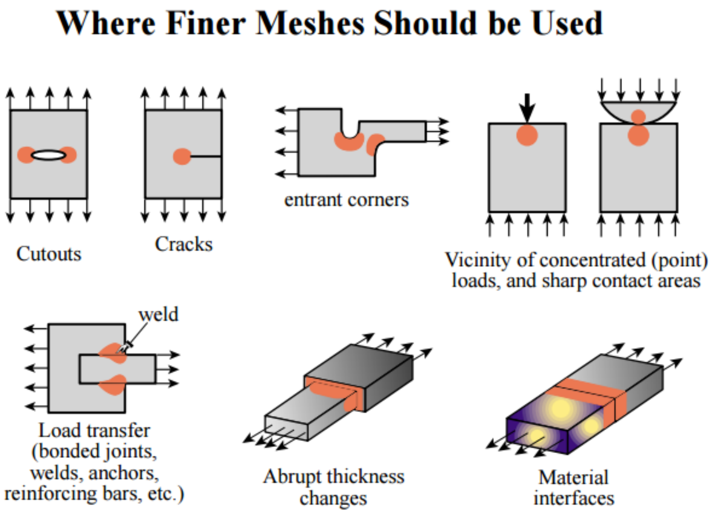

Figure 2. 3: Area of Application of Finer meshes (College of Engineering and Applied Science, 2015)

2.2.2 Meshing

To get an accurate result it is compulsory that there should be a proper connection between all joining edges if the mesh involves more than one materials. In merging sharp corners, it is important to divide the edge into smaller parts with curve for better result when processed. An explanation of this is shown in Figure 2.4.

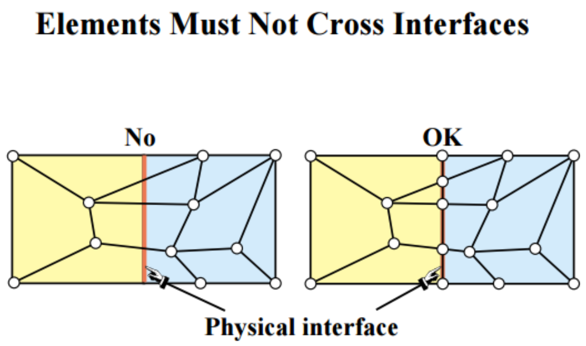

Figure 2. 4: Meshing two parts

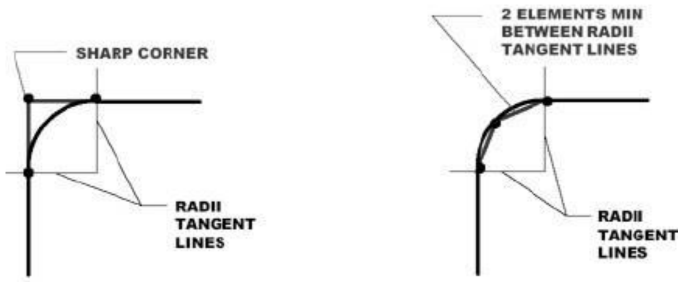

Figure 2. 5: Meshing Fillets (johan, 2000)

2.2.3 Jacobian ratio

The term Jacobian is used to measure how an element differs from an ideal formed shape element. It is a value ranging from 0 to 1. The Jacobian ratio of 1 explains an ideal element which might be theoretical, in reality a Jacobian is usually less than 1 but greater than 0.

The calculation for the Jacobian Ratio is done at the Gauss Point of element integration. Jacobian determinant is calculated at each integration points.

The ratio of the maximum and minimum Jacobian determinant value is called the Jacobian value. The calculation of Jacobian determinant for 2D element is different from the procedure of calculation for 3D elements.

For 2D elements, the element must be projected onto a plane where the calculation will be done while calculation is done directly on the 3D elements.

An incorrect result will be obtained when an element is having a negative Jacobian ratio. A negative Jacobian ratio is obtained if the quadrilateral element is not convex.

2.2.4 Aspect ratio

This relates to the ratio of the length of the shortest edge of a shape to its longest edge. A triangular shape has a smaller aspect ratio when compared to a square; this is illustrated in Figure 4.6 below.

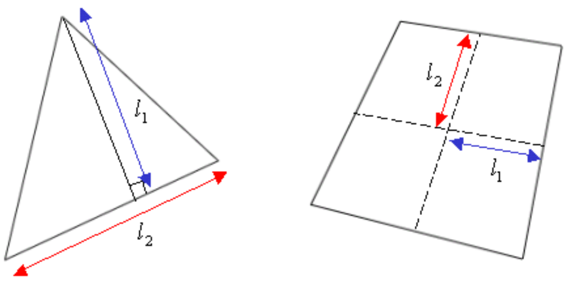

Figure 2. 6: Aspect Ratio of Quad and Triangular element

The aspect ratio of an element is calculated using the Equation 2.4 shown below

$$Aspect\ Ratio_{Triangular} = \frac{1}{\max(\frac{\sqrt{3}l_2}{2l_1})} \tag{2.4}$$

$$Aspect\ Ratio_{Quad} = min\frac{l_1}{l_2} \tag{2.5}$$

Sharp edges in meshes are not desirable therefore are considered bad meshes due to their poor aspect ratio.

2.2.5 Warpage

This measure the degree of bending on the mesh plane. This relates to situations in which any nodes of a quadrilateral element is placed on another plane different from the originating plane in which the other nodes are placed. Figure 2.7 below is a graphical display of a quad element on warpage.

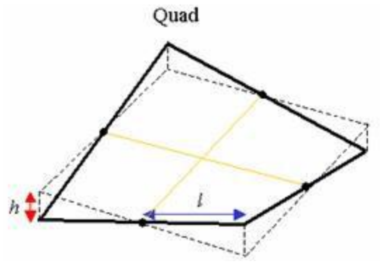

Figure 2. 7: Quad Element experiencing warpage

The warpage of elements can be calculated using Equation 2.6 below.

$$\text{Warpage} = 1 - \frac{\text{h}}{\text{min(l)}} \tag{2.6}$$

2.3 Ls-Dyna Application

Ls-dyna as mentioned earlier is used to solve linear and non-linear finite element problems using simulations. Both linear and non-linear equations are used repeatedly in a loop so long the boundary conditions are satisfied. Ls-dyna uses time step when running simulations, this is due to the iterative pattern of operation.

2.3.1 Time step size

Ls-Dyna is programed to satisfy predefined boundary conditions therefore it is a necessity for iterations until the boundary conditions specified are satisfied. The degree of precision of results and simulation run time is greatly dependent on the Time step size specified by the user. The time step size is directly proportional to the element size, i.e for a small element size, the time step size will be smaller thus the degree of accuracy and precision of results obtained from simulations will increase. But on the adverse side, the total time needed to run the simulation will increase significantly.

Time step integration process is governed by Equation 2.7 shown below.

$$\Delta t_n+1= \alpha\times m\{\Delta t_1,\Delta t_2,\ldots,\Delta t_N\} \qquad (2.7)$$

2.3.2 Consistency of units

Ls-dyna uses five (5) different sets of units that means when feeding in values into the software for simulation the user must firstly ensure that the choice of unit being used is clarified in order to get a proper result. The magnitudes of quantities are fed into the software without the unit specified because the program uses a method called consistent unit.

Table 2. 1: Consistent Unit Set

	1	**2**	**3**	**4**	**5**
Length	m	mm	mm	in	mm
Time	s	ms	s	s	ms
Mass	kg	kg	ton	Ib	g
Force	N	kN	N	Ibf	N
Stress	Pa	GPa	MPa	psi	MPa
Energy	kN.mm (J)	kN.mm	N.mm	Ibf.in	N.mm

Table 2.1 shows 5 sets consistent unit sets usable in conducting LS-Dyna simulations

In this project set number 2 is used that is length is measured in millimeter (mm), time in milliseconds (ms), mass in Kilograms (Kg), force in Kilo newton (kN), Stress in GigaPascal (GPa) and energy in KiloNewton millimeter (kN.mm).

2.4 Crash Box Assessment Parameters

In this section, the major parameters used to judge the performance of a crash box will be discussed briefly. These parameters include;

1. Energy absorbed (EA)
2. Specific energy absorbed (SEA)
3. Initial peak force (IPF)
4. Mean Load (P_{mean})
5. Crush force efficiency (CFE)
6. Undulation of load carrying capacity (ULC).

2.4.1 Energy absorbed (EA)

This parameter is vital to judge the amount of energy absorbed by the tube. This parameter is usually identified as the area under the Force-Displacement curve of the crushing. This energy is the energy converted from kinetic energy to plastic strain energy due to the material deforming beyond its elastic limit, therefore for better energy absorption the material of the tube should be ductile.

$$EA = \int_0^{displacement} F\,dx \qquad (2.8)$$

Where F is the crush force in the axial direction and dx is the crushed displacement.

2.4.2 Specific energy absorbed

This parameter is used to calculate the amount of energy absorbed per mass of the tube. This is defined as the amount of energy absorbed divided by the mass of the tube in kg.

$$SEA = \frac{Amount\ of\ Absorbed\ Energy\ (EA)}{mass\ (kg)} \qquad (2.9)$$

2.4.3 Initial peak force (IPF)

This is another parameter used to assess the performance of crash boxes. This force is the related to the initial peaking of the load due to the impact of the striking mass in the axial direction. This is the force needed to cause the first folding of the material. This force needs to be as low as possible because it determines how much force is needed to cause the crash box to deform before transferring the effect of the force to the body of the car.

2.4.4 Mean load (F_{mean})

This is the mean force defined as the ratio of total absorbed energy to the total crushing distance. The mean load is defined by equation 2.10 below.

$$F_{mean} = \frac{\int_0^{displacement} F\ dx}{x} \qquad (2.10)$$

Where *F* is the force, *dx* is the change in displacement and *d* is the total displacement

2.4.5 Crush force efficiency (CFE)

This is defined as the mean force divided by the maximum peak force as shown in Equation 2.11 below;

$$CFE = \frac{F_{Mean}}{F_{Max}} \tag{2.11}$$

2.4.6 Undulation of load carrying capacity (ULC)

This is defined as the ratio energy absorption stability mathematically using Xiang et.al 2014. This is represented with the Equation shown below.

$$ULC = \frac{\int_0^d |F(x) - P_m| dx}{\int_0^d F(x) dx} \tag{2.12}$$

The amount of absorbed energy determines the mean load used to calculate the ULC. The smaller the value of ULC the better an energy absorber performs.

CHAPTER 3
MODELLING AND INTERPRETATION

3.1 Analysis Tools

In this section, the program tools used in the analysis of this work will be discussed briefly.

3.1.1 Altair HyperMesh

The hypermesh program is a product of Altair Hyperworks. It is a high performance and broad mesh generation finite element pre-processing program, it is commonly used and compatible with commercially available CAD and CAE systems. In this project, the finite element model of each specimen is generated using the Hypermesh program. This program is needful in generating a finite element model of an already existing CAD model of a specimen needed for finite element analysis.

Hypermesh has evolved over the past 2 decades into the leading pre-processor for FEA high fidelity modeling, and its ability to quickly generate mesh for complex geometry has made hypermesh popular amongst FEA researchers. This program supports a broad range of CAD and solver interfaces (Altair Hyperworks, n.d, 2019).

Hypermesh gains its relevance in the following

1. Automatic Shell Mesh generation
2. Model Morphing
3. Automatic Solid mesh generation
4. Manual mesh generation
5. Geometry Dimensioning
6. CAD Interoperability and compatibility
7. Batch Meshing for fast automatic high quality finite element mesh generation for assembly
8. Vast array of CAE solvers, etc…

Hypermesh is an advanced easy to use tool capable of editing CAE models and also capable of generating meshes in different element sizes and geometry as shown below.

1. Tetra meshing
2. CFD meshing
3. High fidelity meshing
4. Solid map hexa meshing
5. Surface meshing

3.1.2 Ls- Dyna

Ls-Dyna is a product of the Livermore Software Technology Corporation. It is a finite element analysis solver program used to simulate complex real life scenario in a computer environment. This program has its application crossing over the automobile industry, military, bioengineering, construction industry, aerospace industry (LSTC, n.d. http://www.lstc.com/products/ls-dyna Retrieved 26 April, 2019). This solver is capable of solving nonlinear, transient dynamic element analysis.

The term nonlinear is used in association to the following complicated situations.

1. When the boundary conditions of a solution is changing i.e a change in contact algorithm between parts over time
2. Situations involving materials not exhibiting an ideal elastic behavior
3. Solving complicated solutions involving large deformations.

The application of Ls-Dyna is broad and its numerous features can be used to analyze and simulate a physical event.

In this project Ls-Dyna finds its application in running the simulation of the crushing of the tubes. This is done using Ls-Dyna because this simulation involves large plastic deformation within a short time frame. This type of simulation is considered a transient dynamic simulation as the program captures enormous data of simulations done to simulate real life situations happening at a fast rate such as explosions, automotive crashing (this project) and sheet metal stamping related to manufacturing.

3.1.3 Catia

CATIA is one of the tools also used in this project (Dassault Systemes, n.d.). It is one of the World's leading design program for products both in 2D and 3D. This program is used by most international leading organizations in the design industry to model products that are identical and can capture the real life characteristics of the actual product with ease. CATIA is widely used by professionals in the automotive industry, architectural organizations, and engineers in manufacturing.

The CAD 3D solid model of the specimens used in this project were drawn using CATIA and then saved in an IGS format which is compatible with the hypermesh solver deck for mesh generation.

3.1.4 GetData Graph Digitizer

Often time curves are seen in literature, and this curves might be needful in the validation stage of the study and the authors or researchers who obtained these curves might not be within reach to obtain the raw digital data used to define these curves therefore GetData Graph Digitizer (GetData Graph Digitizer, n.d.) Finds its relevance in this project in obtaining data points of graphs found in literature. Examples of such curves that this program is needful to obtain their digital data include stress-strain curves of materials. This program converts graphical curves to numerical values with simple steps.

The following features are found in the GetData graph digitizer.

1. Supports the following image format
    a. TIFF
    b. JPEG
    c. BMP
    d. PCX

2. Easy manual digitization of graphs
3. Automatic Digitization in two algorithms
4. Easy copy of obtained data to a clipboard
5. Can export obtained data in the following format
    a. TXT
    b. XLS for MS excel
    c. XML AND DXF for Autocad
    d. EPS for PostScripts

3.2 Methodology

The energy absorption capacity of the crash boxes varies depending on the plastic deformation. Total Energy Absorption, Specific Energy Absorption (SEA), Mean Crush Force, Crush Force Efficiency (CFE) and Peak Crush Force are generally used to determine the energy absorption capacity of the crash boxes.

Four (4) crash boxes will be designed with different geometric features and their energy absorption characteristics will be analyzed under different specified impact velocity axially.

Finite element analyses of the crash boxes will be carried out using the non-linear finite element code Ls-Dyna software. The crash box models will have one side fixed. A rigid plate, considered as a moving wall, will be placed to the other end which will create the deformation force. A contact algorithm will be used to simulate the contact between the rigid plate and crash box.

The models will be generated by CAD programs such as SolidWorks or Catia, and then imported to Hypermesh for automatic mesh generation. Simulation will be conducted using Ls-Dyna. Finally, the post-processor Ls-PrePost will be used for result visualization and data acquisition and also using Microsoft Excel sheet to manage and draw curves using the data obtained from simulations.

This project began with the study of the literatures related to this work and afterwards started several test run with several other models and simulations for validations were done.

The material stress-strain curve was obtained from literature using the GetData graph digitizer.

The CAD solid model of the specimen is generated using CATIA, then exported to Hypermesh for mid plane mesh generation and then exported in the format of a keyword file ready to be run in Ls-Dyna in which all the boundary conditions and material properties are included before the run is made.

After the run is completed the Ls-Post processor is used to read and visualize the results.

CHAPTER 4

VALIDATION OF CRUSH BOX MODELS

Validation study is important in order to compare results obtained in the present study with studies from literature using same models with same material and geometrical parameters and boundary conditions. Before the present study can be furthered it is important that a minimal level of discrepancies or minimal level of error between the previous study and the present study is reached. Once validation study is successful, the next phase of the study is to use similar parameters and identical material as it applies to the present study in the design and development phase.

The validation of this work is done in accordance to the work of Mamalis et al, 2001 in which thin walled tapered tubes are fixed on one end and impacted axially on the other end with a striking mass of 60kg.

4.1 CAD modelling of specimen

The 3D CAD model of the specimens are drawn using CATIA and saved as an “igs” format which is compatible with Hypermesh for meshing. Figure 4.1 below shows a 3D CAD model of specimen 1 displayed in CATIA work bench.

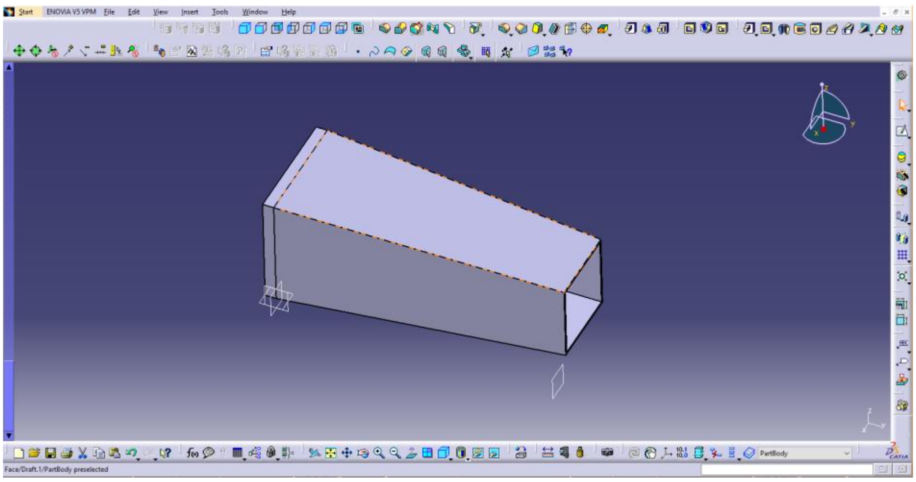

Figure 4. 1: 3D CAD Model of specimen 1 in CATIA work space

4.2 Finite Element Modelling

The mesh for finite element model was generated using the Hypermesh and this model is divided into 2 physical parts which are the rigid wall (fixed end) and the thin wall tube (crash box) while the drop mass (moving wall) is defined in the Ls-Dyna code.

The parts are meshed individually using their unique part identification number (part ID) with the rigid wall numbered 1 and the tube numbered 2 as shown in Figure 4.2.

In Hypermesh, the midplane of the model is obtained before mesh is done in order to simplify the process of meshing and it reduces simulation time and the number of element formed. Using the midplane, no overwhelming negative effect of the processing of the model especially when Ls-Dyna is used to run the simulation, this is because in Ls-Dyna you can input the thickness of the section directly into the code without having to depend on the design thickness parameter given in the CAD 3D model.

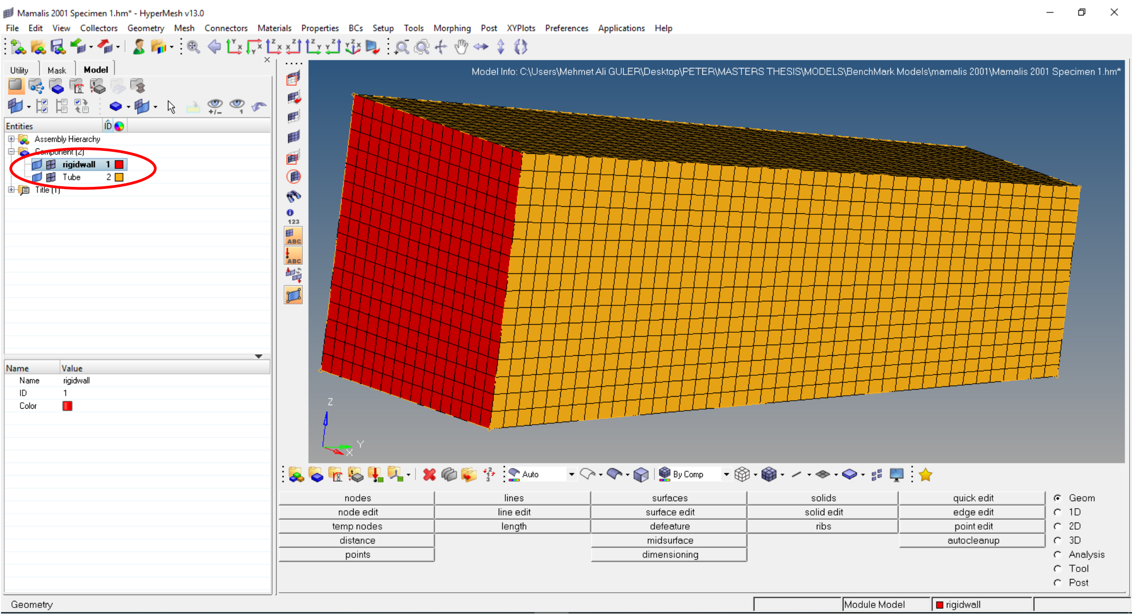

Figure 4. 2: Finite Element Mesh of Specimen 1 on Hypermesh Workbench

Once the model is finished, it is important to clean the geometry, check the element for failed meshes then renumber the nodes and elements.

The model must be saved and exported using the Solver Deck command as "nodes_elements.k".

The specimens were modelled using the 4-node "shell" element enlisted in the Ls-Dyna element library. This choice of element type is because the 4-node element gives a better presentation of macroscopic mesh distortion.

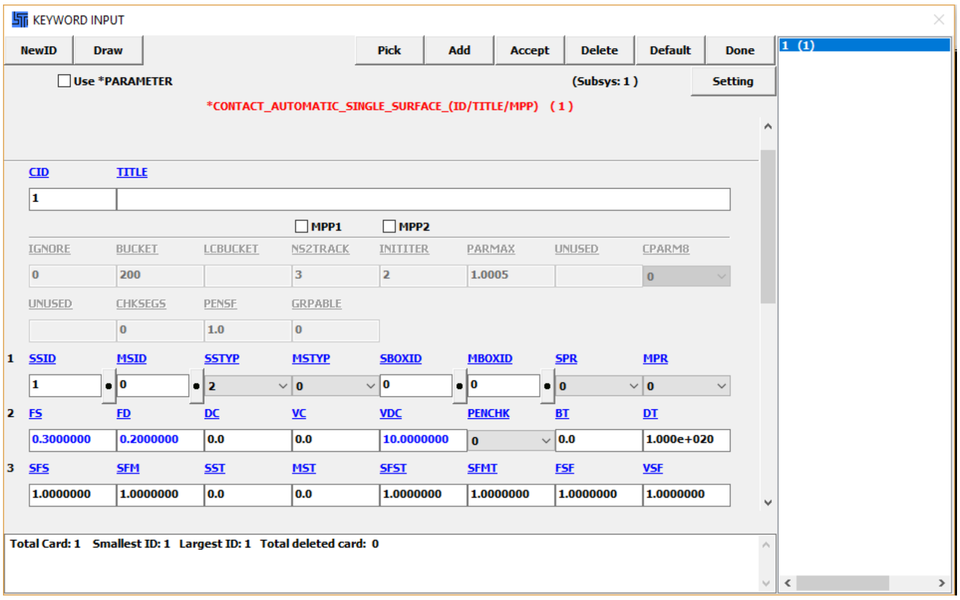

Figure 4. 3: Contact definition of model

The crash box is modelled as an isotropic elastic-plastic material with strain hardening. Discretization of the material property values was done before they were inserted into Ls-Dyna. The purpose of value discretization is because it gives a better fitting to the actual material properties of the real material.

The fixed wall and the moving wall (dropped mass) are both modelled as "Rigid bodies". The dropped mass was set up to have only one degree of freedom which is in the direction of impact.

The contacting surfaces between the crash box and the drop mass (moving wall) is modelled using the “automatic single surface” contact definition with details shown in Figure 4.3.

4.3 Material Property and Preparation of Material Card In Ls-Dyna

The material used to design the crash box is an annealed low carbon steel (AISI 1021). The mechanical properties of low carbon steel are given in Table 4.1.

Table 4. 1: Mechanical properties of mild steel

Material	Mild Steel (AISI 1021)
Density	7800 kg/m^3
Young’s Modulus	207 GPa
Poisson’s Ratio	0.28
Yield Stress	370 Mpa
Ultimate Stress	440 Mpa

Figure 4.4 shows the true stress – true strain curve of the mild steel used in this project. This graph is plotted with data obtained from experimentation done by (A.G. Mamalis, 2001) in their study.

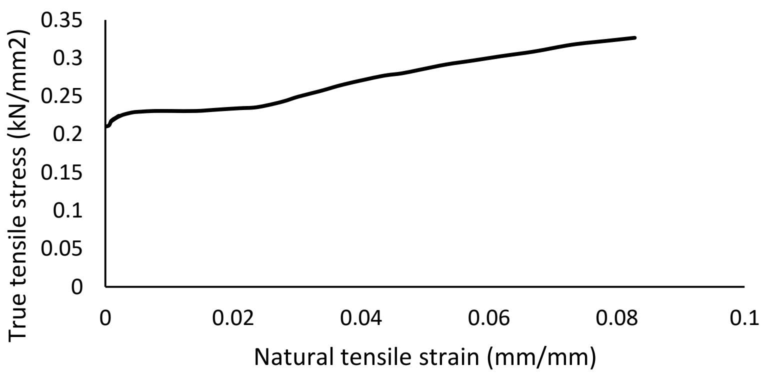

Figure 4. 4: True Stress - True Strain curve of annealed low carbon steel (AISI 1021)

4.4 Validation of Specimens

A Finite Element representation of specimen 1 is shown in Figure 4.5. This model was generated using hypermesh and Table 4.2 shows the design parameters of specimen 1.

Table 4. 2: Material and simulation characteristics of specimen 1

Geometrical and simulation characteristics	Values
Bottom Dimensions (mm)	50.0x51.9
Top Dimensions (mm)	34.5x35.6
Height (mm)	127
Wall thickness (mm)	0.97
Semi Apical Angle (^{o})	5
Drop mass (kg)	60
Impact velocity (m/s)	6.05
Number of element used by Mamalis et al	3300
Number of Elements used in present study	2772
Number of elements used by Altin et al	N/a

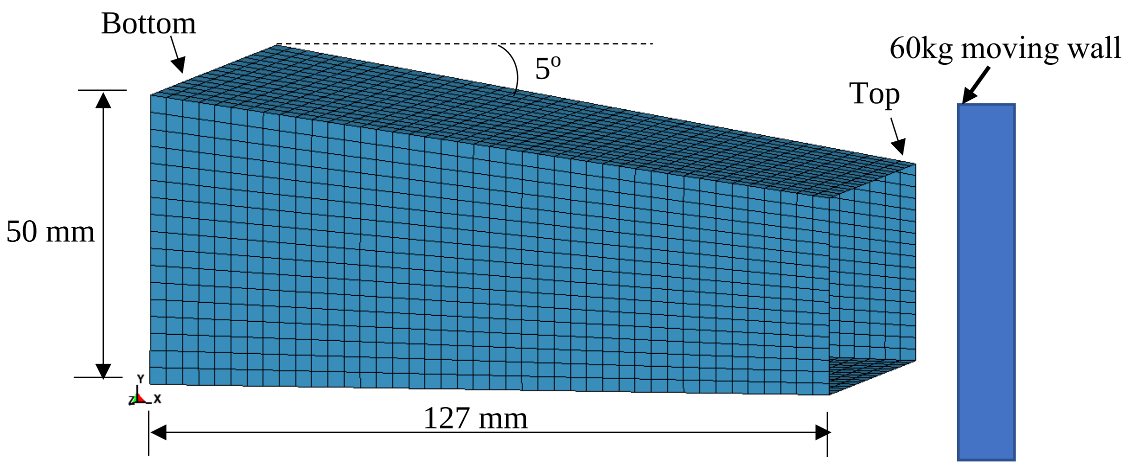

Figure 4. 5: Finite Element Model of Specimen 1

Shown in Figure 4.6 below is a side view of an illustration of the collapse behavior and fold formation of specimen 1 undergoing crushing at different time intervals. It is seen from the Figure 4.6 that the collapse of the walls of the tube forms concentric lobes. While Figure 4.7 is an axial view of specimen 1 after a complete simulation of the run. From Figure 4.7, it is seen that the four walls have identical collapse behavior.

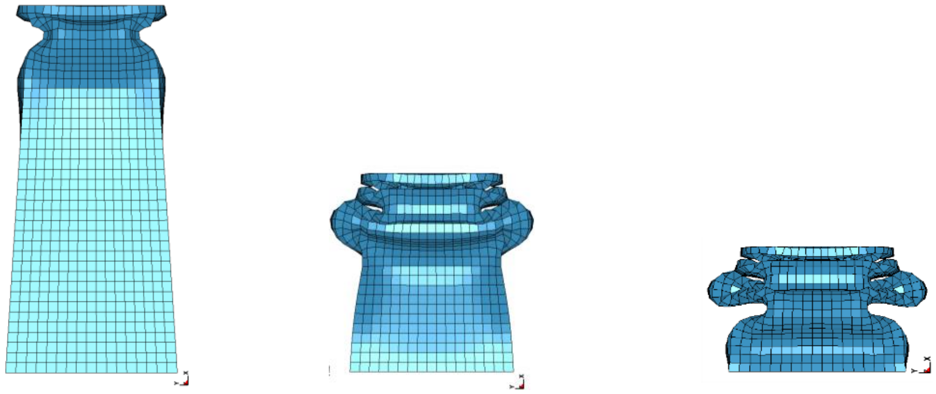

Figure 4. 6: Step collapse behavior of Specimen 1

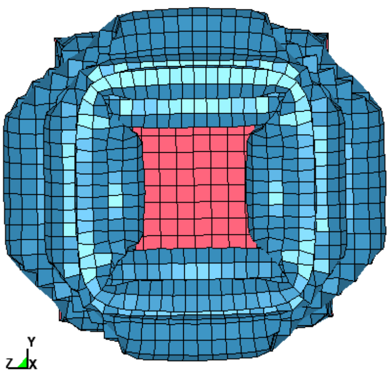

Figure 4. 7: Axial View of fully deformed shape of specimen 1 after impact

4.4.1 Results Comparison of Specimens with previous studies.

It is easier to analyze data using a graph, that is why the force – displacement data obtained in the simulation of this specimen is used to draw a curve which will help give a better picture in the mode and behavior of the specimen as the force is being applied as well as the variations in the results of this present study and that of previously established solutions. Figure 4.8 shows the graphical comparison of the Force – displacement curves.

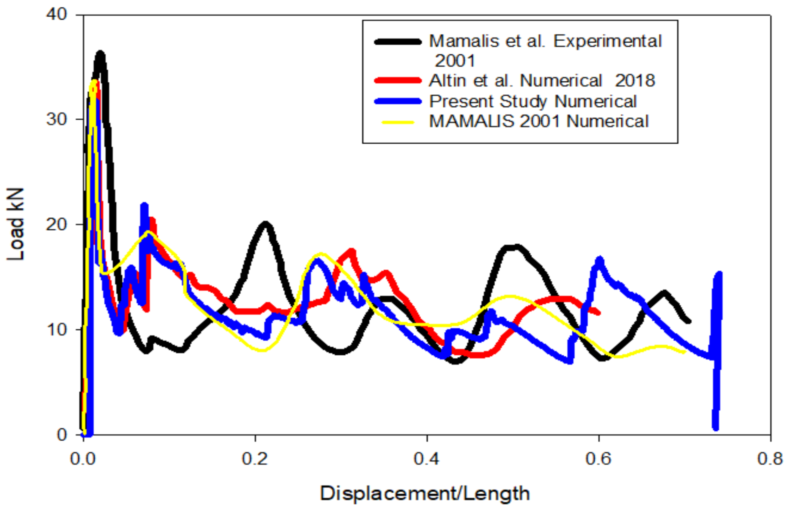

Figure 4. 8: Validation of Force - Displacement curve of specimen 1

According to the force – displacement graph of specimen 1 in Figure 4.8, it is observed that the numerical study of Mamalis et al 2001, Altin et al 2018 and the present study have similar tendencies with little variations but the variation of the experimental curve to that of the numerical studies are more obvious but still within acceptable range of performance as confirmed by Mamalis et al and Altin et al in their studies.

The degree of error or deviation from the experimental result is obtained using equation 4.1

$$\%\ \text{Error} = \frac{\text{Experimental value} - \text{Numerical Value}}{\text{Experimental value}} \text{ X } 100\% \qquad 4.1$$

The experimental value is the baseline to check the degree of accuracy of the numerical studies, therefore the performance parameters are assessed based on their convergence to the experimental values.

4.4.2 Total Energy Absorbed

The total energy absorbed is calculated using equation 2.8. According to the results of the total energy absorbed by specimen 1 in a deformation length of 75mm and the error obtained in the present study is less than 2%. The deviation of the total absorbed energy of specimen 1, 2, 3, and 4 from the experimental values are 1.8%, 14.2%, 23.43%, and 0.17% respectively. As regards to energy absorbed, specimen 4 has the least level of deviation.

4.4.3 Initial peak force

The present study has a lower error value. Meaning that the performance of specimen 1 in this present study in the aspect of initial peak force, it is closer to the experimental study than the previous studies. The deviation of the present study of specimen 1, 2, 3, and 4 from the experimental values are 6.21%, 15.85%, 14.38% and 26.87% respectively. The validation of the specimen 1 gives the lowest level of deviation from the experimental values of initial peak force.

4.4.4 Specific Energy Absorption

The specific energy absorbed (SEA) is calculated using equation 2.9. On the base of the specific energy comparison shows that the present study has a little above 2% error which is higher than the level of error of the previous studies but still within an acceptable range therefore the study can be furthered. The deviation of specimen 1, 2, 3 and 4 from the experimental values observed are 2.196%, 14.21%, 22.55% and 1.61% respectively.

4.4.5 Mean crush force

The mean crush force of specimen 1, 2, 3 and 4 in the validation study for this work has a maximum deviation from experimental values of 23.43% which is from specimen 3 and minimum error level of 0.17% which corresponds to specimen 4.

4.4.6 Crush force efficiency

In the Crush force efficiency column of Table 4.5 that there is only about 4.3% error deviation from the experimental result. And this shows less compared to previously established studies.

4.5 Graphical representations of specimen 2

Shown in Figure 4.9 and Table 4.3 are the finite element model and geometrical parameters of specimen 2 respectively.

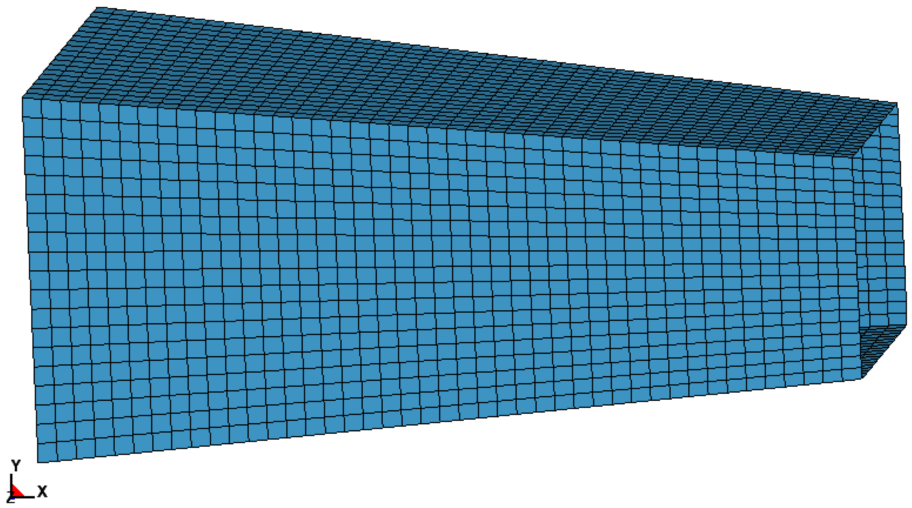

Figure 4. 9: Finite Element Model of Specimen 2

Table 4. 3: Geometrical and simulation characteristics of specimen 2

Geometrical and simulation characteristic	Values
Bottom Dimension	58.5x59.1
Top Dimension	35.7x36.4
Height (mm)	127
Wall thickness (mm)	1.47
Semi-apical angle (^{o})	7.5
Drop mass (kg)	60
Impact Velocity (m/s)	9.1
Number of Elements used by Mamalis et al	3300
Number of Element used by Altin et al	N/A
Number of Elements used in present study	3268

As shown in Figure 4.10, the collapse behavior of specimen 2 is not as smooth as specimen 1. The formation of folds are not concentric and there appears to be a bulge in one of the sides of the walls as seen in Figure 4.11.

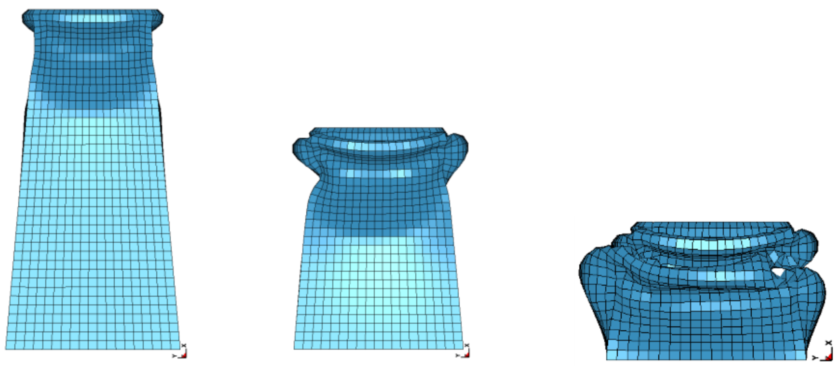

Figure 4.10: Collapse Behavior of specimen 2

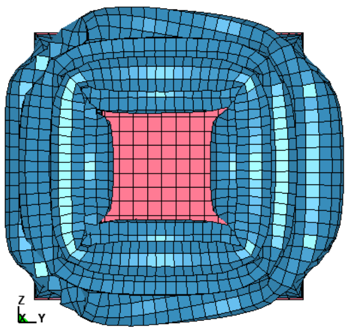

Figure 4.11: Fully deformed shaped of specimen 2 (front view)

According to the graph shown in Figure 4.12, all the curves have similar tendencies except for Mamalis experimental that has a bit of obvious deviation from the others but are still in good agreement with the others as the peaking and rising of the curves have similar behavior.

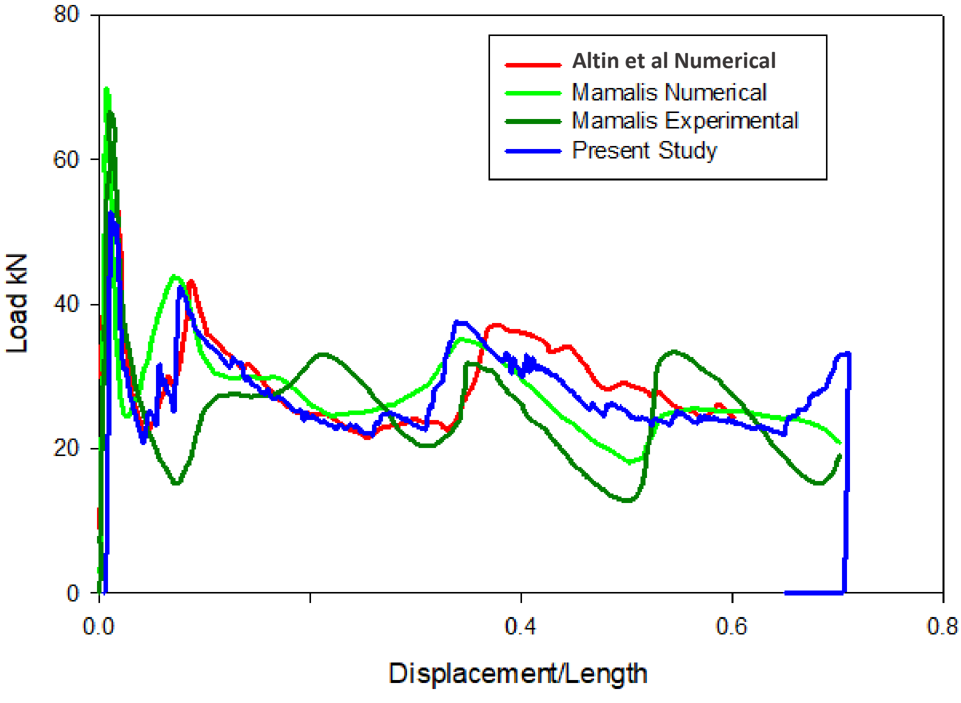

Figure 4.12: Graphical comparison of the Force - Displacement of specimen 2

Total energy absorption shows the deviation of accuracy from the experimental result and the already established solution of previous studies and this is of a magnitude of 14.2% error.

It is understood that the highest level of error in validation is in the initial peak force which gives about 15.9% deviation from the experimental result. This result can be improved by further meshing of the specimen with smaller elements.

4.6 Graphical representation of specimen 3

The image of the finite element model of specimen 3 is shown in Figure 4.13 and the geometrical and simulation characteristics used for the validation study of specimen 3 is given in Table 4.4.

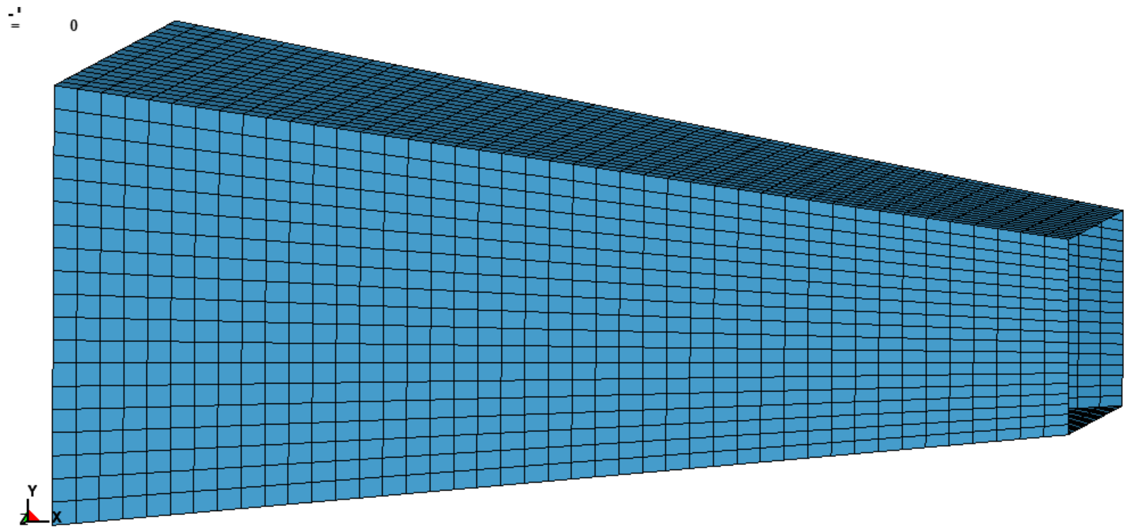

Figure 4.13: Finite Element model of Specimen 3

After the finite element simulation of specimen 3, the collapse modes are captured for 4 stages to better understand the collapse mode of specimen 3 under impact. This collapse modes is shown in Figure 4.14 and Figure 4.15.

Table 4. 4: Geometrical and simulation characteristics of specimen 3

Geometrical and simulation characteristics	Values
Bottom Dimension (mm)	55.8x57.2
Top Dimension (mm)	26.5x27.5
Height (mm)	127
Wall thickness (mm)	1.6
Semi Apical angle (°)	10
Drop Mass (kg)	60
Impact Velocity (m/s)	9.25
Number of Elements used by Mamalis et al	2000
Number of Elements used by Altin et al	N/A
Number of Elements used in present study	3182

The results obtained from simulation of specimen 3 is compared with the results of previously established solutions in literature. The Force – Displacement curve shown in Figure 4.16 shows similar crushing behavior with the numerical studies of previous works.

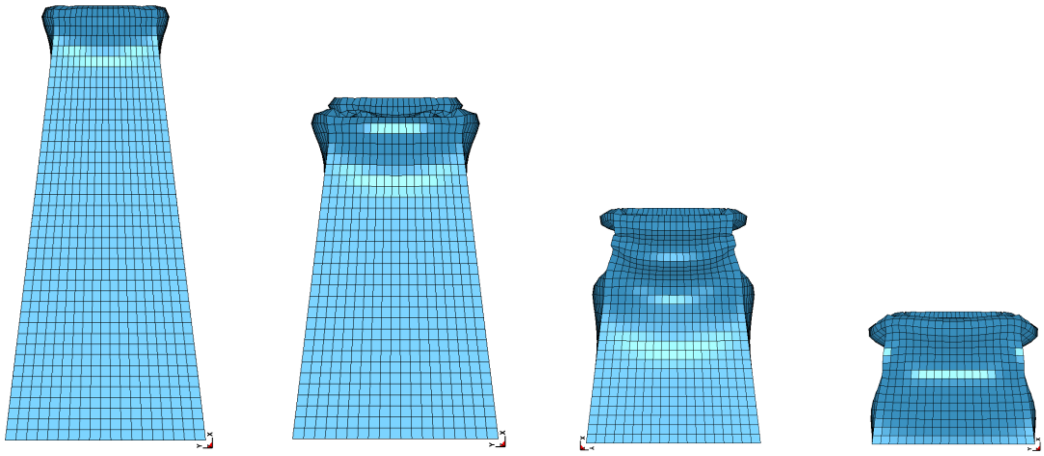

Figure 4.14: Collapse behavior of specimen 3

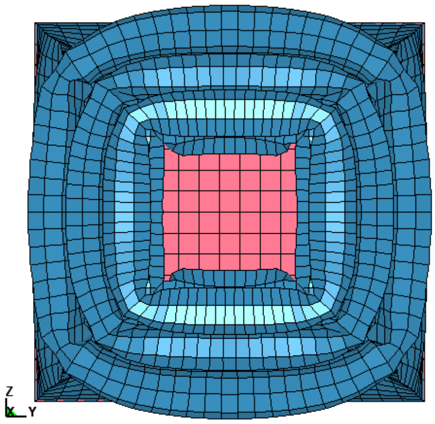

Figure 4.15: Final collapse shape of specimen 3 (Front view)

The performance of specimen 3 in the validation study is analyzed and a maximum deviation from the experiment is observed in the crush force efficiency comparison which yielded about 44.2% deviation. While the minimum deviation is recorded to be about 14.4%. These variations can be observed in Figure 4.16.

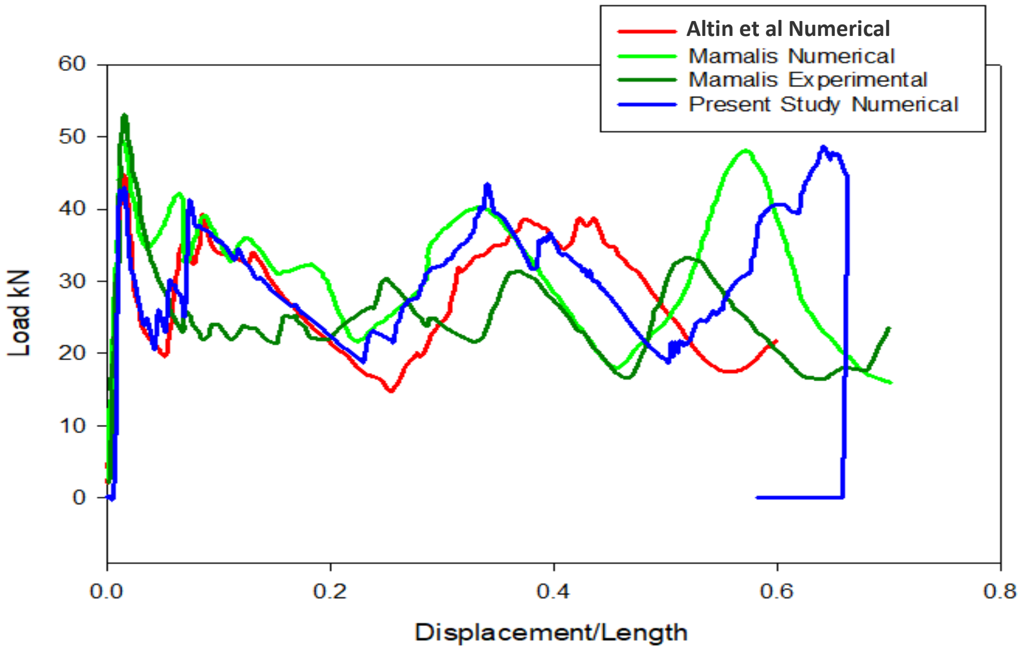

Figure 4.16: Graphical Comparison of force - Displacement of Specimen 3

4.7 Graphical representation of specimen 4

The finite element model of specimen 4 is shown in Figure 4.17 and the geometrical and simulation characteristics.

Table 4. 5: Geometrical and simulation characteristics of specimen 4

Geometrical and simulation characteristics	Values
Bottom Dimension (mm)	56.8x56.5
Top Dimension (mm)	11.7x11.6
Height (mm)	127
Wall thickness (mm)	1.52
Semi apical angle (^{o})	14
Drop Mass (kg)	60
Impact Velocity (m/s)	8.7
Number of elements used by Mamalis et al	4400
Number of elements used by M. Altin et al	N/A
Number Elements used in Present study	3344

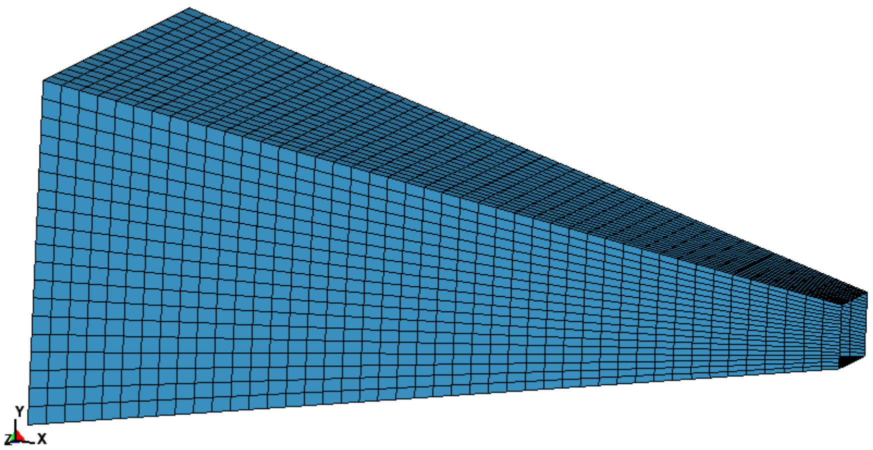

Figure 4.17: Finite Element Model of Specimen 4

Figure 4.18 and 4.19 illustrates the collapse behavior of specimen 4 under crushing. From the figures it is seen that specimen 4 experiences a stable collapse behavior with uniform fold formation on the four (4) walls. This effect is attributed to the smaller edge of specimen 4 as a result of its larger semi-apical angle

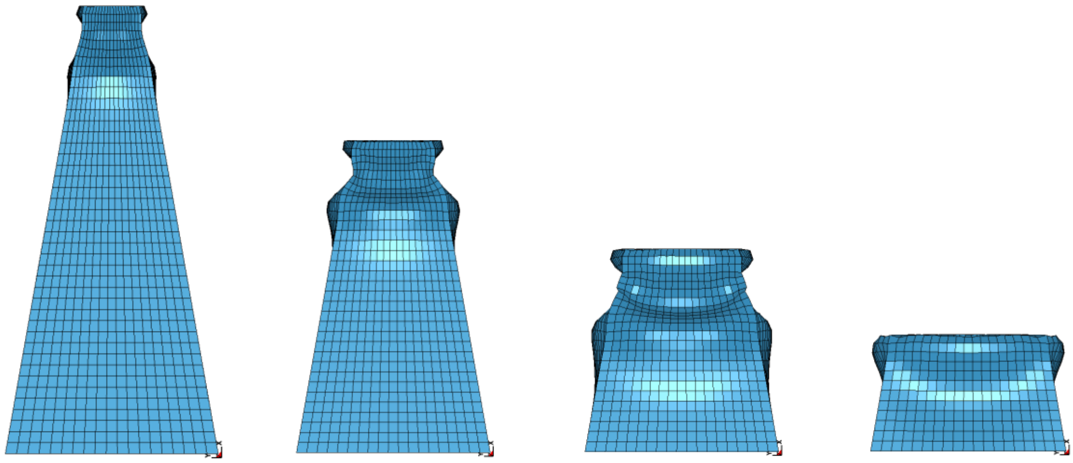

Figure 4.18: Collapse Behavior of Specimen 4

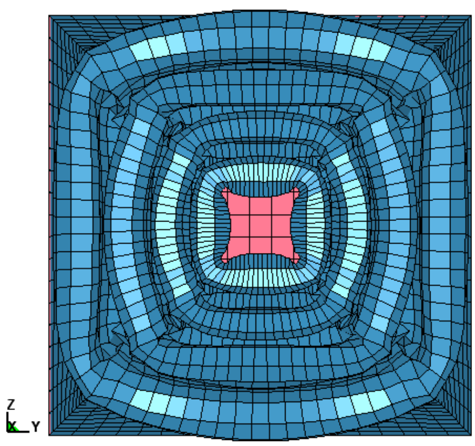

Figure 4.19: Final Deformed Shape of Specimen 4 (Front View)

Figure 4.20 shows the comparison of the load – displacement curve of the present study and the previously established solutions in literature.

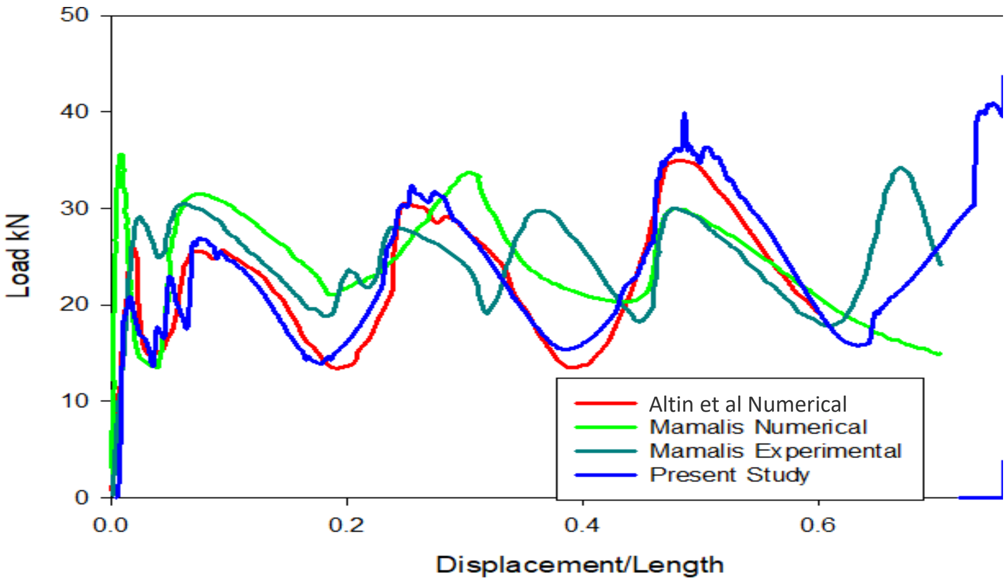

Figure 4.20: Comparison of force - displacement curves of specimen 4

Table 4.6 shows the numerical result of the present study of specimen 4 has only 0.2% mean crush force deviation from the experiment. From the results tabulated in Table 4.6, the validation of specimen 4 has a better agreement with the experimental results than the previous studies.

Validation results showed the lowest deviation from the experimental result was about 0.17%. Maximum deviation is for initial peak force of about 26% deviation from experimental result except for the crush force efficiency of specimen 2 which gives about 35.67%. This results deemed satisfactory therefore the present study was furthered to investigate the effect of velocity on the energy absorption characteristics of crash boxes.

Table 4. 6: Results of Validation Study

COMPARISON OF ENERGY ABSORBING CHARACTERISTICS OF MODEL WITH PREVIOUS STUDIES					
	Specimen	**1**	**2**	**3**	**4**
AUTHORS	**COMPARISON OF THE TOTAL ENERGY ABSORPTION**				
MAMALIS ET AL experimental	(kJ)	0.896	1.792	1.716	1.738
MAMALIS ET AL Numerical	(kJ)	0.91	2.011	2.061	1.812
	Error (%)	1.5	12.2	15	4.2
Altin Kilinc Numerical	(kJ)	0.894	2.034	1.93	1.585
	Error (%)	0.3	13.5	11.1	8.8
Present Study Numerical	(kJ)	0.880	2.046	2.118	1.741
	Error (%)	1.9	14.2	23.4	0.2
	COMPARISON OF THE INITIAL PEAK FORCE				
MAMALIS ET AL experimental	(kN)	36.5	63.37	50.43	29.3
MAMALIS ET AL Numerical	(kN)	33.44	68.41	52.82	35.98
	Error (%)	8.3	7.9	4.7	22.7
Altin Kilinc Numerical	(kN)	33.94	53.63	45.24	25.56
	Error (%)	8.3	15.3	10	12.7
Present Study Numerical	(kN)	34.233	53.329	43.18	21.428
	Error (%)	6.2	15.9	14.4	26.9
	COMPARISON OF THE SPECIFIC ENERGY ABSORPTION				
MAMALIS ET AL experimental	(kJ/kg)	5.517	6.642	6.672	8.675
MAMALIS ET AL Numerical	(kJ/kg)	5.6	7.455	8.011	9.043
	Error (%)	1.5	12.2	15	4.2
Altin Kilinc Numerical	(kJ/kg)	5.503	7.54	7.503	7.909
	Error (%)	0.3	13.5	11.1	8.8
Present Study Numerical	(kJ/kg)	5.395828	7.585647	8.174918	8.535287
	Error (%)	2.2	14.2	22.5	1.6
Mass (kg)		0.162533	0.26972	0.259085	0.203977

Table 4.6: Results of Validation Study (Continued)

COMPARISON OF MEAN CRUSH FORCE					
MAMALIS ET AL experimental	(kN)	11.94667	23.89333	22.88	23.17333
MAMALIS ET AL Numerical	(kN)	12.13333	26.81333	27.48	24.16
	Error (%)	1.6	12.2	20.1	4.3
Altin Kilinc Numerical	(kN)	11.92	27.12	25.73333	21.13333
	Error (%)	0.2	48.9	12.5	8.8
Present Study Numerical	(kN)	11.69333	27.28	28.24	23.21333
	Error (%)	2.1	14.2	23.4	0.2
COMPARISON OF CRUSH FORCE EFFICIENCY					
MAMALIS ET AL experimental	(%)	32.73059	37.70449	45.36982	79.08987
MAMALIS ET AL Numerical	(%)	36.28389	39.19505	52.02575	67.14842
	Error (%)	10.9	3.95	14.7	15.1
Altin Kilinc Numerical	(%)	35.1208	50.56871	56.88182	82.68127
	Error (%)	7.3	34.1	25.4	4.5
Present Study Numerical	(%)	34.15807	51.15416	65.40065	60.53968
	Error (%)	4.4	35.7	10.06	23.5

CHAPTER 5

ANALYSIS OF CRUSH BOX MODELS WITH DIFFERENT IMPACT VELOCITIES

The validation study shows a reasonable level of degree of agreement with already established solutions in literature. Therefore, it is ideal to move to the next phase of this study.

This project is aimed at analyzing the effect of impact velocity on the energy absorption characteristics of crash boxes using the model of Mamalis et al, 2001. As a case study; the models used in this project are identical with those of Mamalis et al, 2001 therefore, this chapter will be dealing specifically and directly with the procedures and methodology of the present study.

Shown in Table 5.1 are the geometrical parameters of the baseline specimens used in this project.

Table 5. 1: Details of baseline specimens used in this study

	Specimen 1	Specimen 2	Specimen 3	Specimen 4
Top dimensions (mm)	34.5 x 35.6	35.7 x 36.4	26.5 x 27.5	11.7 x 11.6
Base dimensions (mm)	50 x 51.9	58.5 x 59.1	55.8 x 57.2	56.8 x 56.5
Height (mm)	127	127	127	127
Wall thickness (mm)	0.97	1.47	1.6	1.52
Semi apical angle (^{o})	5	7.5	10	14
Drop mass (kg)	60	60	60	60
Impact velocity (m/s)	6.05	9.1	9.25	8.7

In this project the impact velocity was varied four (4) times for each specimen making a total of 16 runs.

While shown in Figure 5.1 are the finite element meshes of the four (4) specimens used in this study.

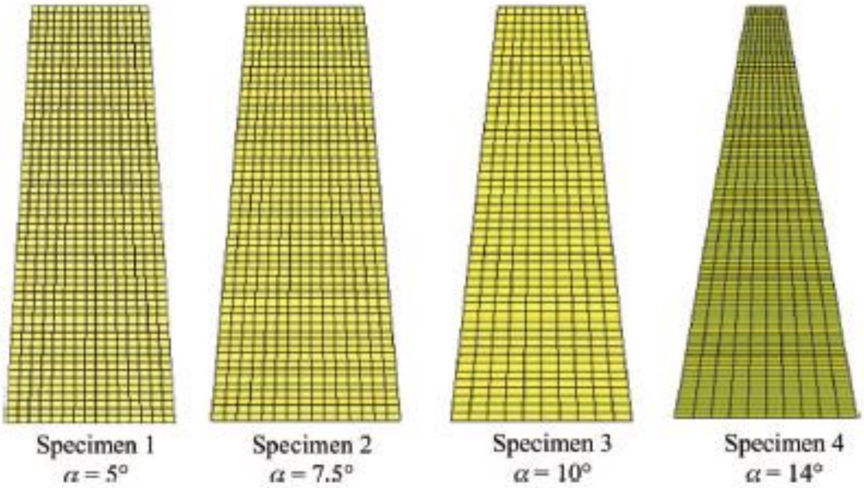

Figure 5. 1: Finite Element Models of the four Specimens

For the purpose of simplicity in computation and running times, Ls-Dyna is used to specify the thickness of the shell element, therefore a midplane is generated using hypermesh. The midplane is used in the simulations in hypermesh, the calculation is done using the midplane in the simulation as the midplane retains the geometrical shape and characteristics of the actual model. The midplane is calculated using Equation 5.1 and Figure 5.2 shown below

$$D_{midplane} = D_{tube} - t_{tube} \qquad (5.1)$$

Where $D_{midplane}$ is the Diameter of the midplane while D_{tube} is the Diameter of the tube and t_{tube} is the thickness of the tube.

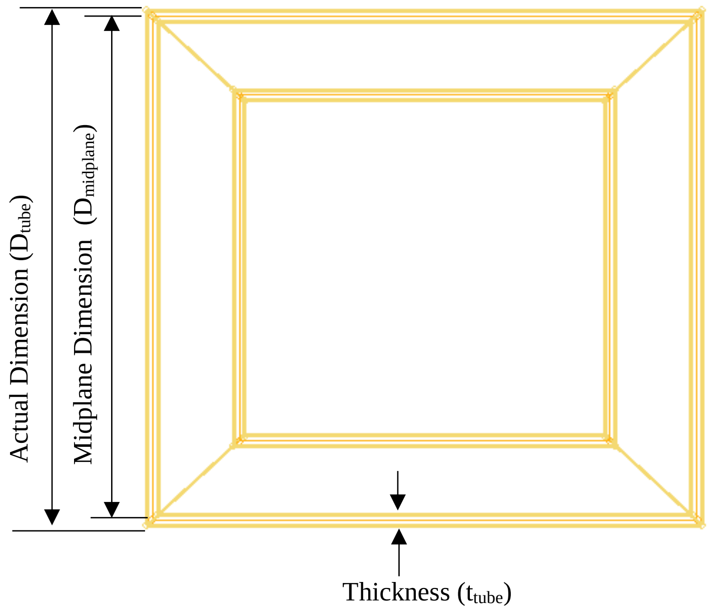

Figure 5. 2: Midplaning a model

5.1 Hypermesh Modeling Procedure of Specimen

In hypermesh, the “igs” format of the CAD model is imported as a geometry, after the importation of the “igs” file the midplane of the geometry is taken using the midplane command in the geometry taskbar as shown in Figure 5.3 below.

After the midplane is done correctly, the model is organized into two (2) parts as shown in Figure 5.4 using the “organize” command in the tool taskbar.

Figure 5.5 illustrates how the parts are identified and organized into components by ensuring that collector is selected and on the drop down menu “surfs” is selected and the desired destination component in which the part is to be moved into should be selected on the “dest component” field.

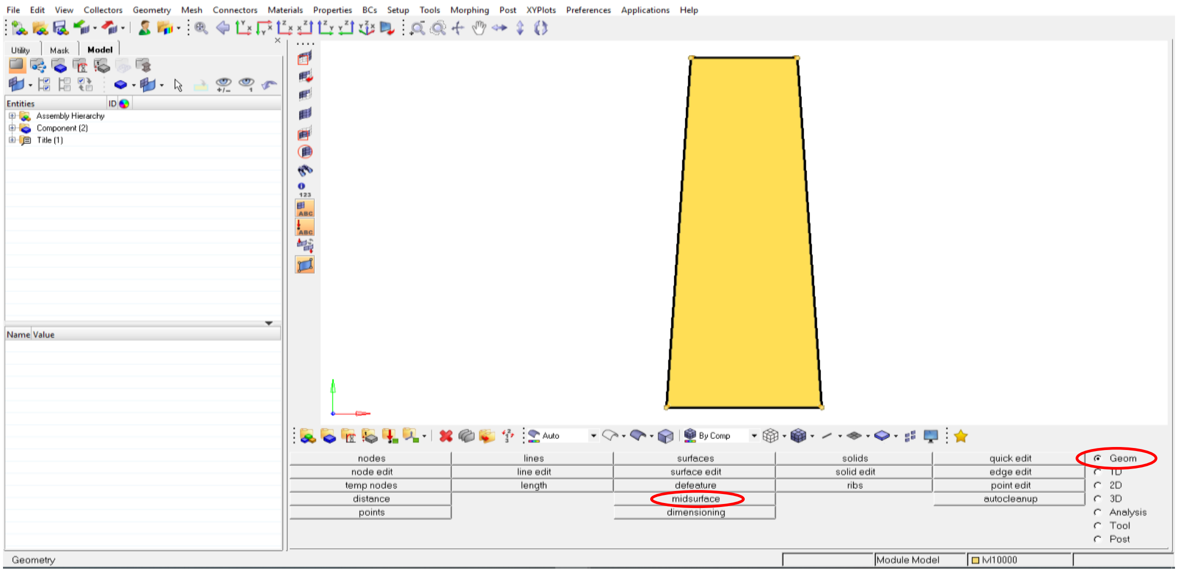

Figure 5. 3: Midplane command

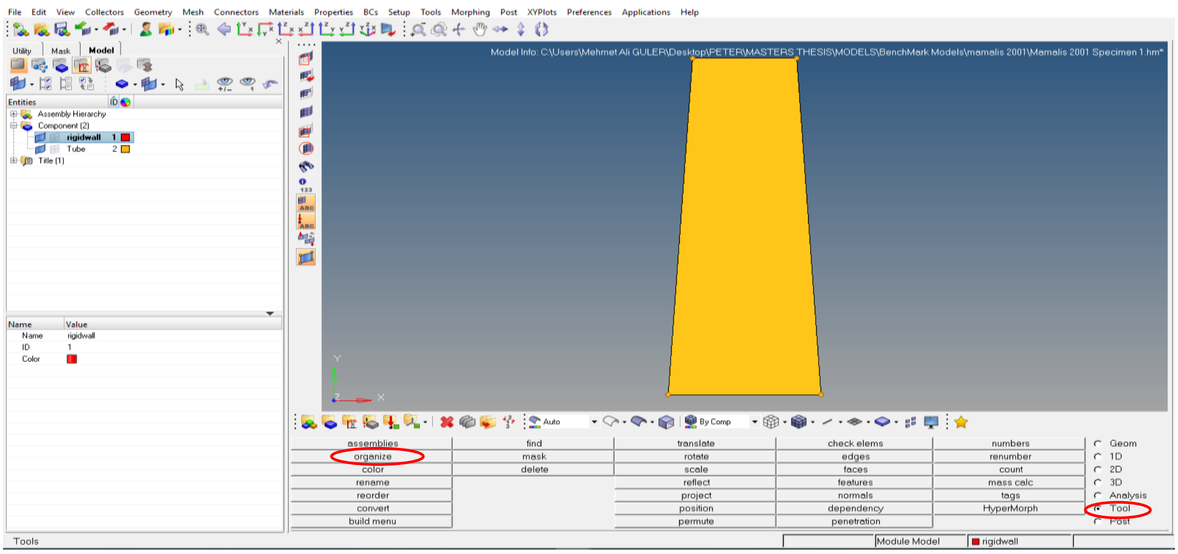

Figure 5. 4: Organize command in the tool task bar

Figure 5.6 shows the list of component created in which any part of the geometry can be placed.

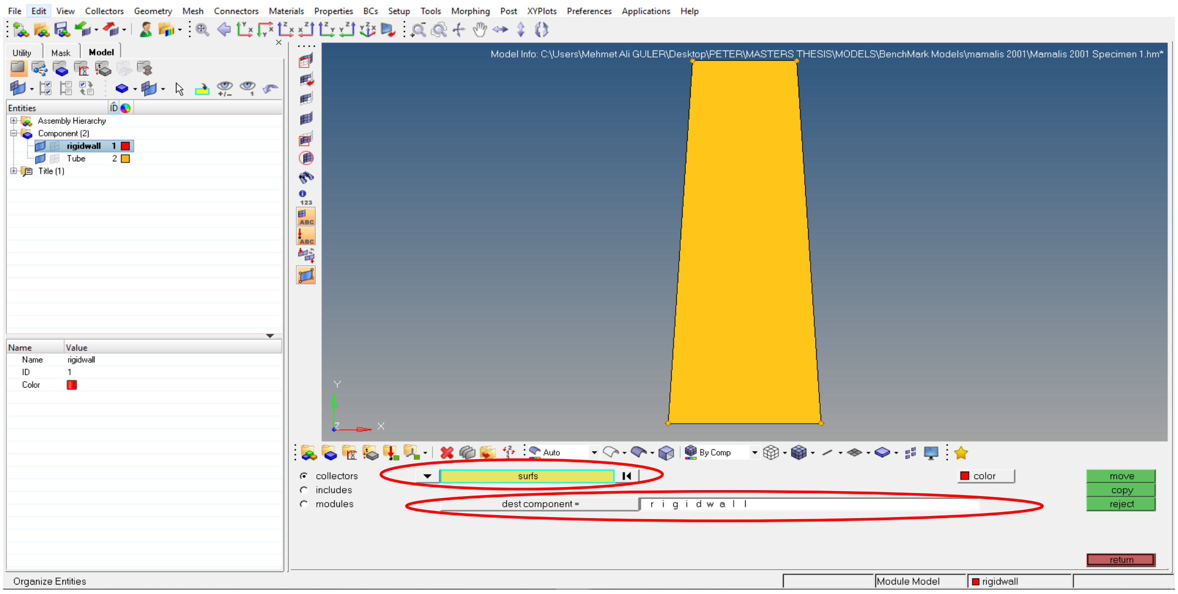

Figure 5. 5: Selection of parts into components

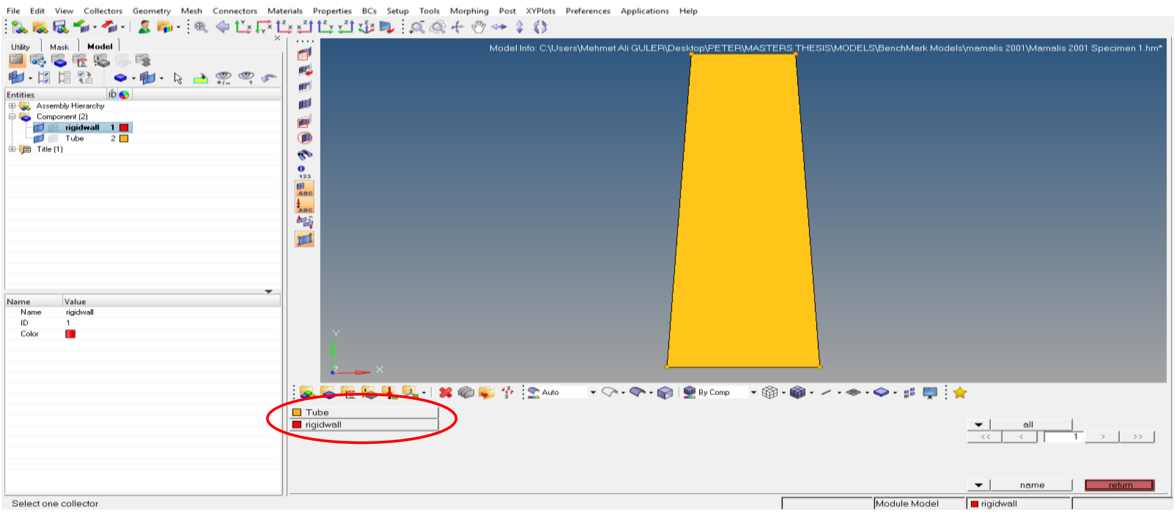

Figure 5. 6: List of component to select when organizing

Whenever a midplane command is used to obtain the midplane of a model, there is a tendency of some joints of the model to loose connectivity with other parts therefore, to ensure proper connectivity of the rigid wall and the tube, the “surface edit” command is used to trim and join free edges that are not properly connected, because for accuracy in obtaining the results it is important that all parts have nodal connectivity.

After connectivity of nodes is done, the “automesh” command is used in the 2D task bar as shown in the Figure 5.7 below.

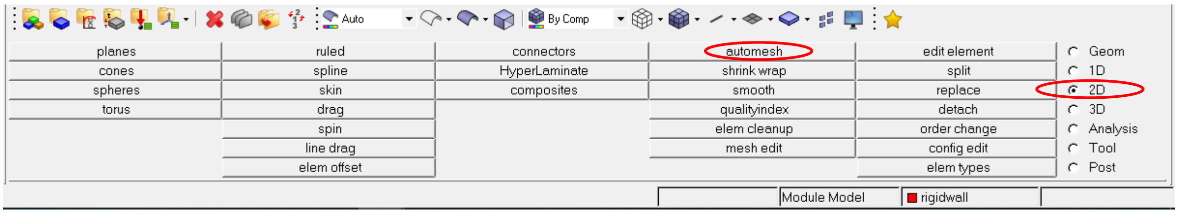

Figure 5. 7: Automesh command in the 2D tool bar

In the “automesh” command menu, “surface” should be selected because the mesh will be generated using the surface of the geometry selected, then the element size is taken to be 2.5mm (Altin et al, 2017) and quad elements are selected as shown in the Figure 5.8.

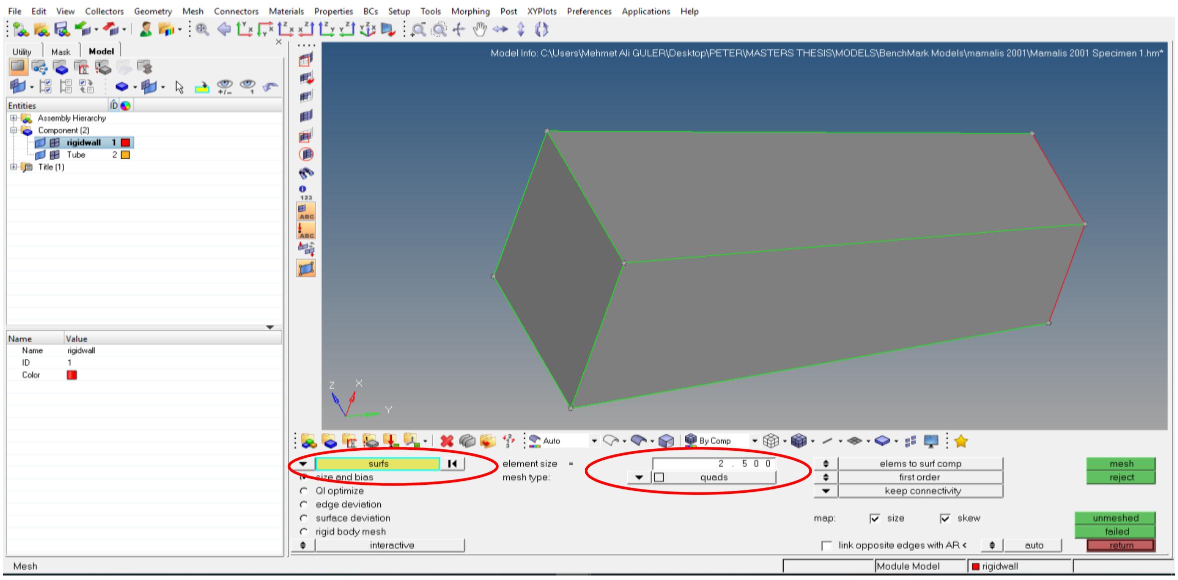

Figure 5. 8: Automesh setup

When the automesh command is setup, the mesh button must be clicked for the program to automatically generate the mesh of the geometry using the criteria specified by the user and displays the next screen shown in Figure 5.9.

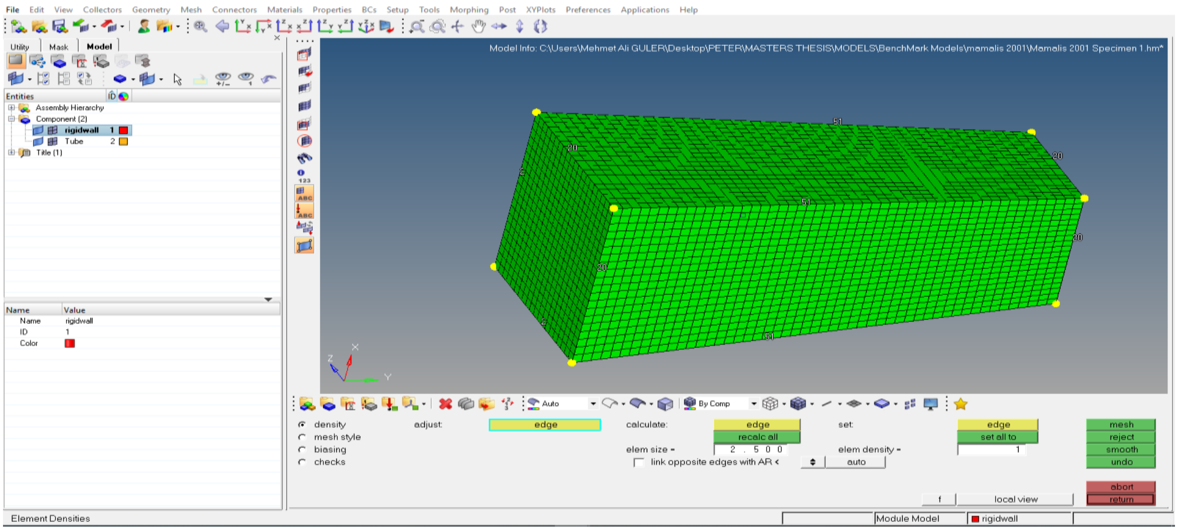

Figure 5. 9: Automeshed model

After meshing, element check is done and the elements and nodes are renumbered using the “renumber” command from the “tools” menu shown in Figure 5.10 below. From the renumber page, it is important that both elements and nodes are renumbered for all parts together to maintain nodal and elemental uniformity. A unique node is formed on the moving surface and it is numbered as “99999” so as to help Ls-Dyna identify the motion of the moving surface.

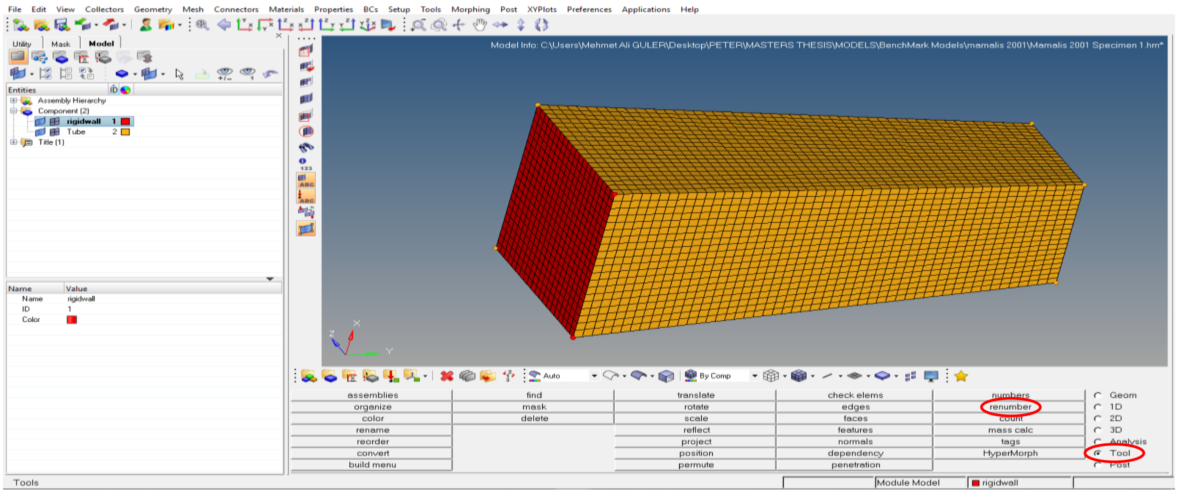

Figure 5. 10: Renumber command on the Tool menu

5.2 Ls-Dyna Pre-post

In Ls-Dyna Prepost, the thickness of the model is added, the material properties of all the parts are added, motion description of the moving wall is inputted, the contact definition is given and other miscellaneous are inputted to run the simulation.

5.2.1 *Mat

*MAT is a command in Ls-Prepost in which the parts are categorized into rigid and deformable parts. With this command, the material properties such as density, Poisson's ratio and Young's modulus are defined.

Being that in this project, only 2 parts are modeled and defined and these parts are made up of materials. Ls-Dyna has a vast array of material library which will not be discussed in this project because they are beyond the scope of this study.

Material type 024 and material type 020 is selected to be the materials of the tube and rigid wall respectively. This selection is made due to already established solutions from literature (A.G. Mamalis, 2001)

*MAT_PIECEWISE_LINEAR_PLASTICITY (MAT024) is used to describe the behavior of the deformable parts such as the tube (crash box).

*MAT_RIGID (MAT020) is the material type defined for the rigid wall. These material cards are shown in the Figure 5.11 and 5.12 below.

It is worth noting as stated in Chapter 2 that Ls-Dyna uses a system known as consistent unit system in which the units are not inputted but the values in its consistent magnitude as shown in Table 2.1.

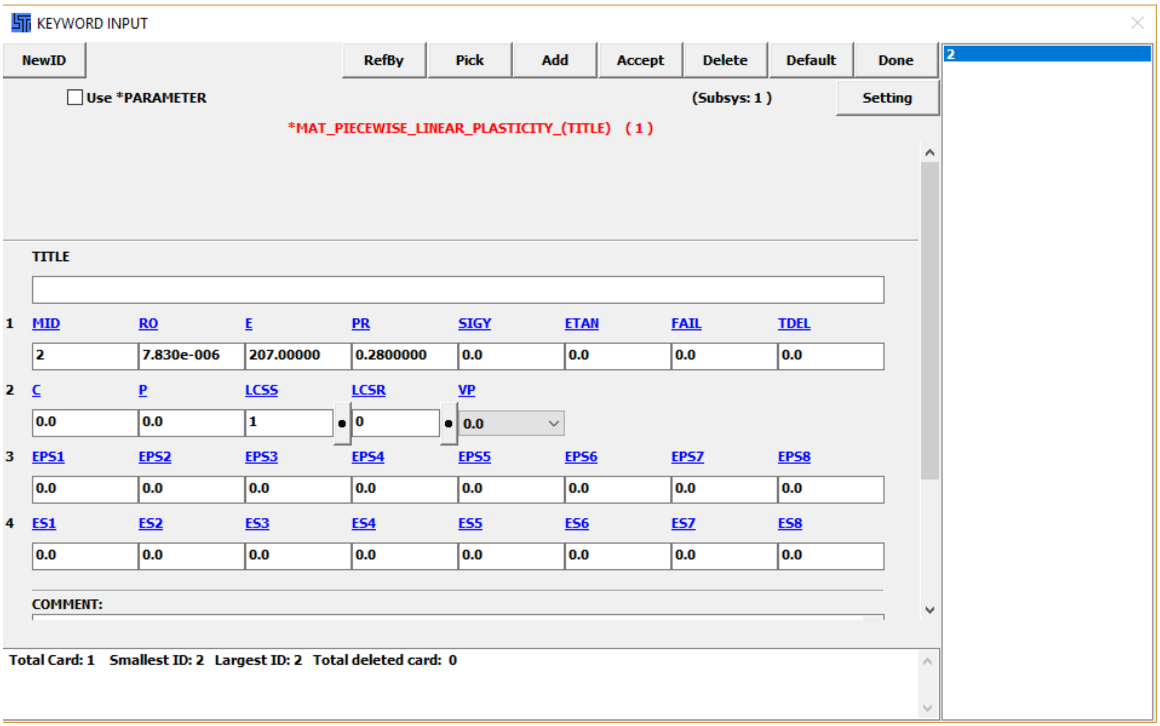

Figure 5. 11: Material card of MAT 024 for the crash box

The tube is modelled using “4 Node” shell element selected from the element library of Ls-Dyna. This selection is made because the “4 Node” shell element gives a better presentation of macroscopic mesh distortion.

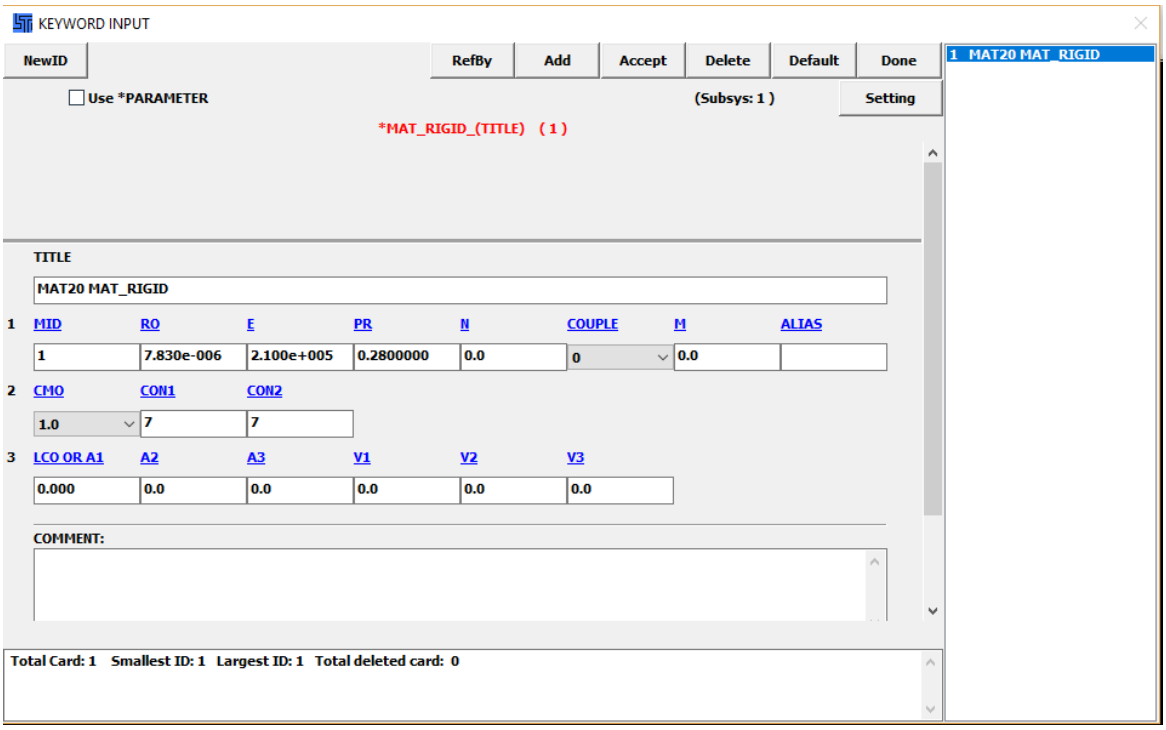

Figure 5. 12: Material card of MAT020 for the rigid wall

On the material card shown in Figure 5.11 and Figure 12, the fields MID, RO, E, and PR are the material I.D, Density, Modulus of Elasticity and Poisson's ratio respectively.

5.2.2 *Rgdwal

The motion of the moving wall is defined using the "*Rgdwal" keyword command *PLANAR_MOVING_FORCES. In this keyword, the velocity, the mass, the direction of motion is specified using the "XT and XH" system (where XT stands for the tail of the arrow of direction and XH stands for the head of the arrow of direction) of the moving wall is given. The keyword of the rigid wall motion is shown in Figure 5.13.

The "XT" and "XH" are used to define the direction of motion in the simulation run. The "XT" is usually indicative of the beginning of the direction vector, while the "XH" is indicative of the direction of the progression of the vector head as illustrated in Figure 5.14.

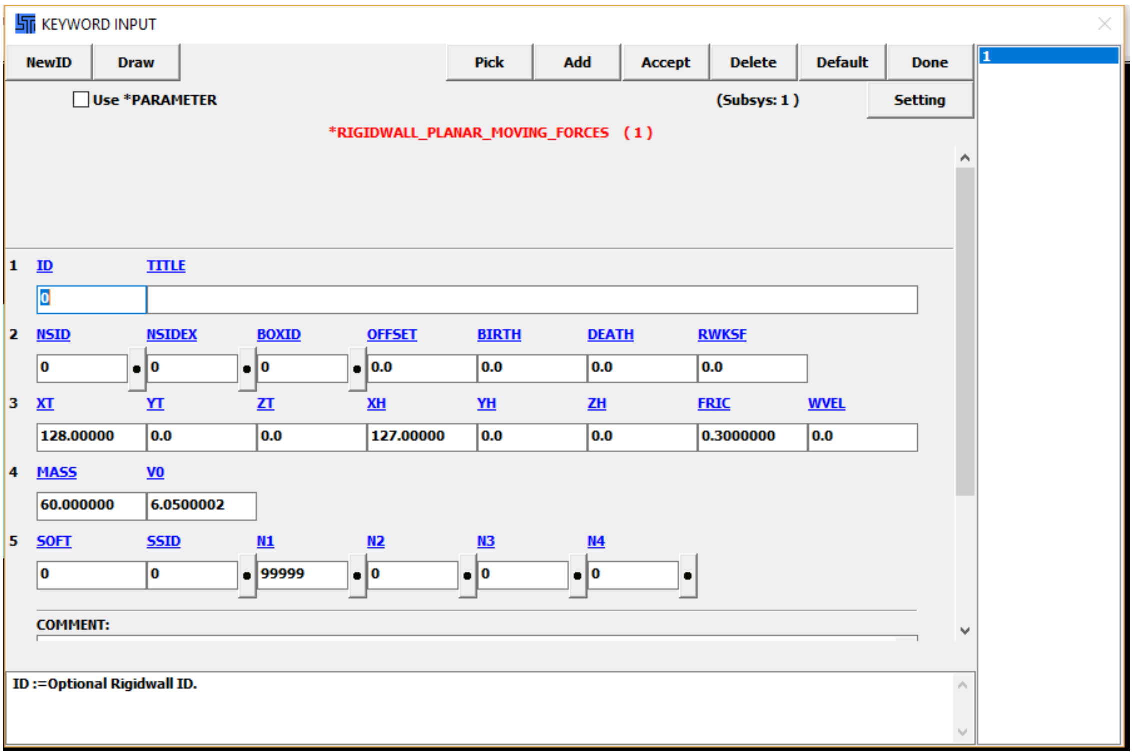

Figure 5. 13: Rigid wall motion keyword card

When XT is greater than XH, it means the direction of vector is to the left along the X axis while if XT is less than XH, the direction of vector is to the right.

Figure 5. 14: XH and XT illustration

5.2.3 *Contact

This key word command is used to give contact definition for the models. In this project, the "Automatic_Single_Surface" contact definition is used as illustrated in Figure 5.14.

The Static coefficient of friction and the dynamic coefficient of friction are entered in the fields titled "FS" and "FD" in Figure 5.14.

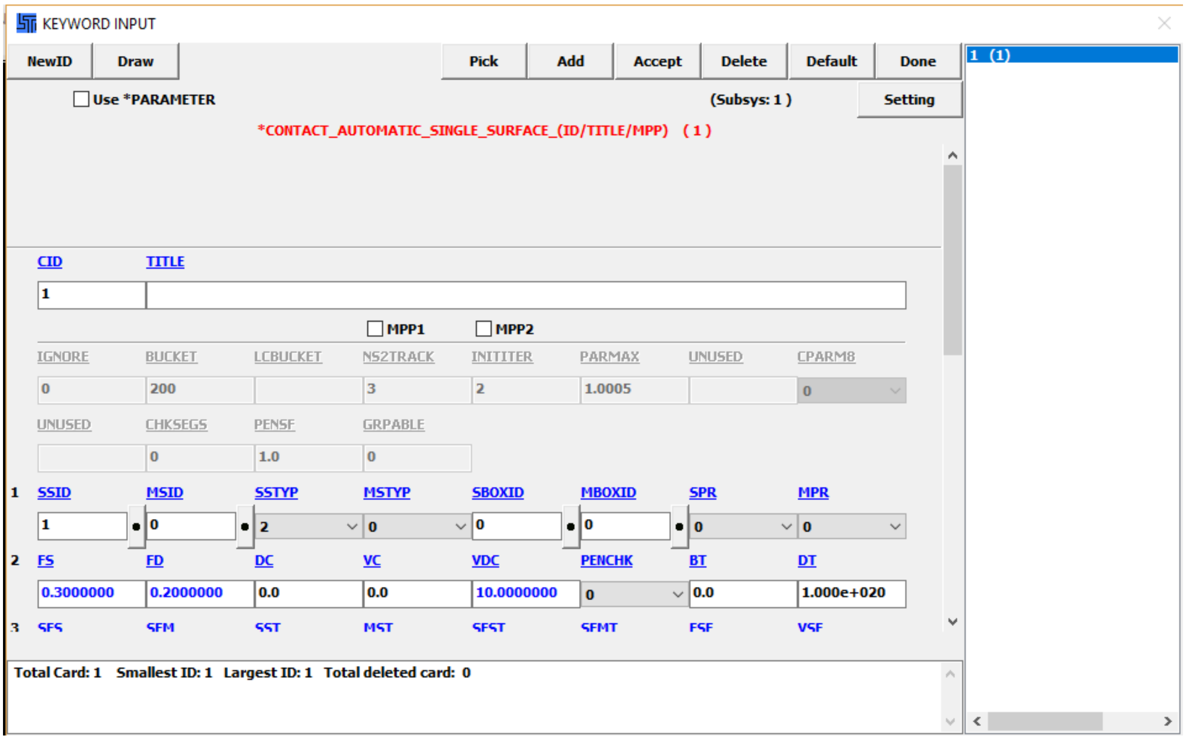

Figure 5. 15: Automatic single surface contact card

5.2.4 *Control

This card controls the condition needed for the simulation to terminate. In this project, the *control card uses the following conditions mentioned below to determine the run time of the simulation.

a) Contact
b) Energy
c) Shell
d) Termination
e) Time step

Figure 5.15 to 5.20 shows the cards for the contact, Energy, Shell, Termination and Time step respectively. The contact control card shown in Figure 5.15 is used to define the contact parameters for the run. While the energy control card is used to include hour glass energy.

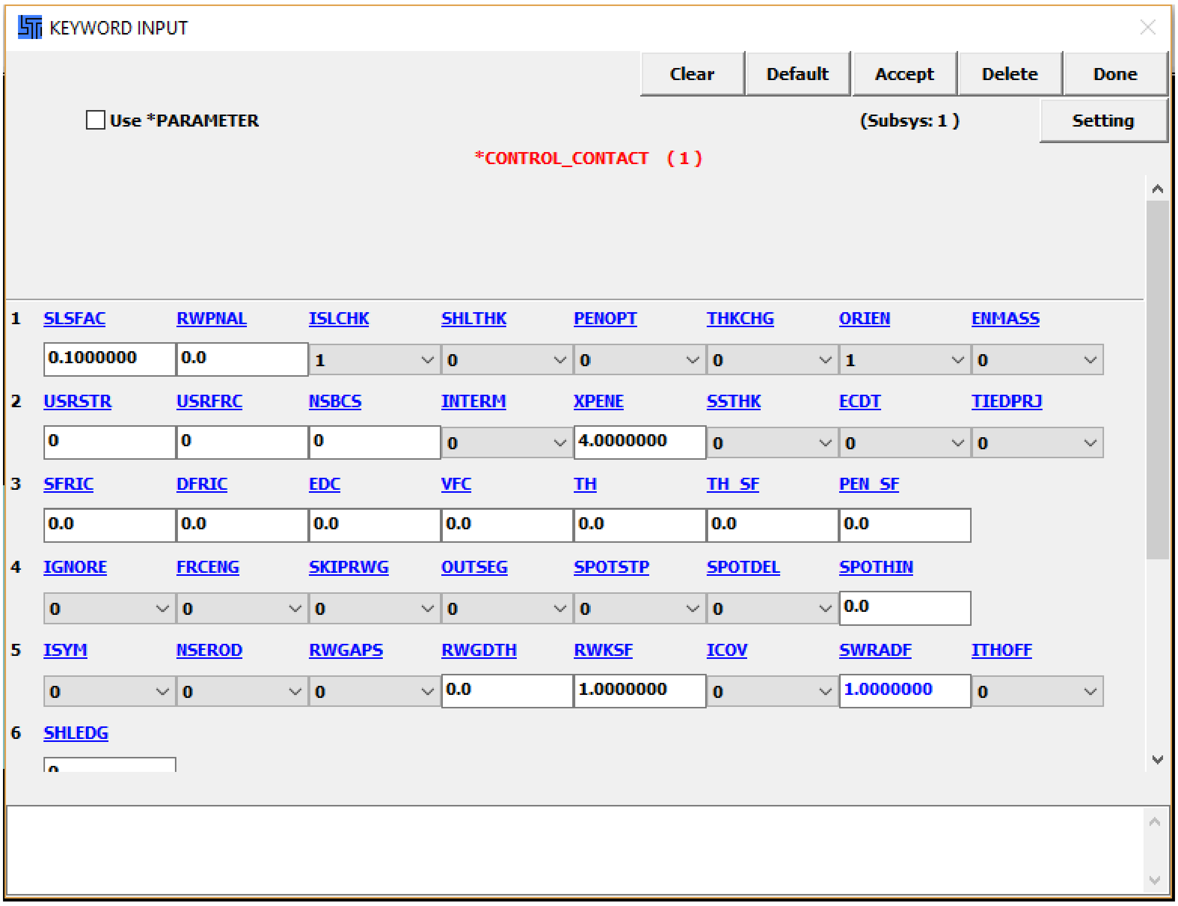

Figure 5. 16: Contact control in Ls Dyna keyword file

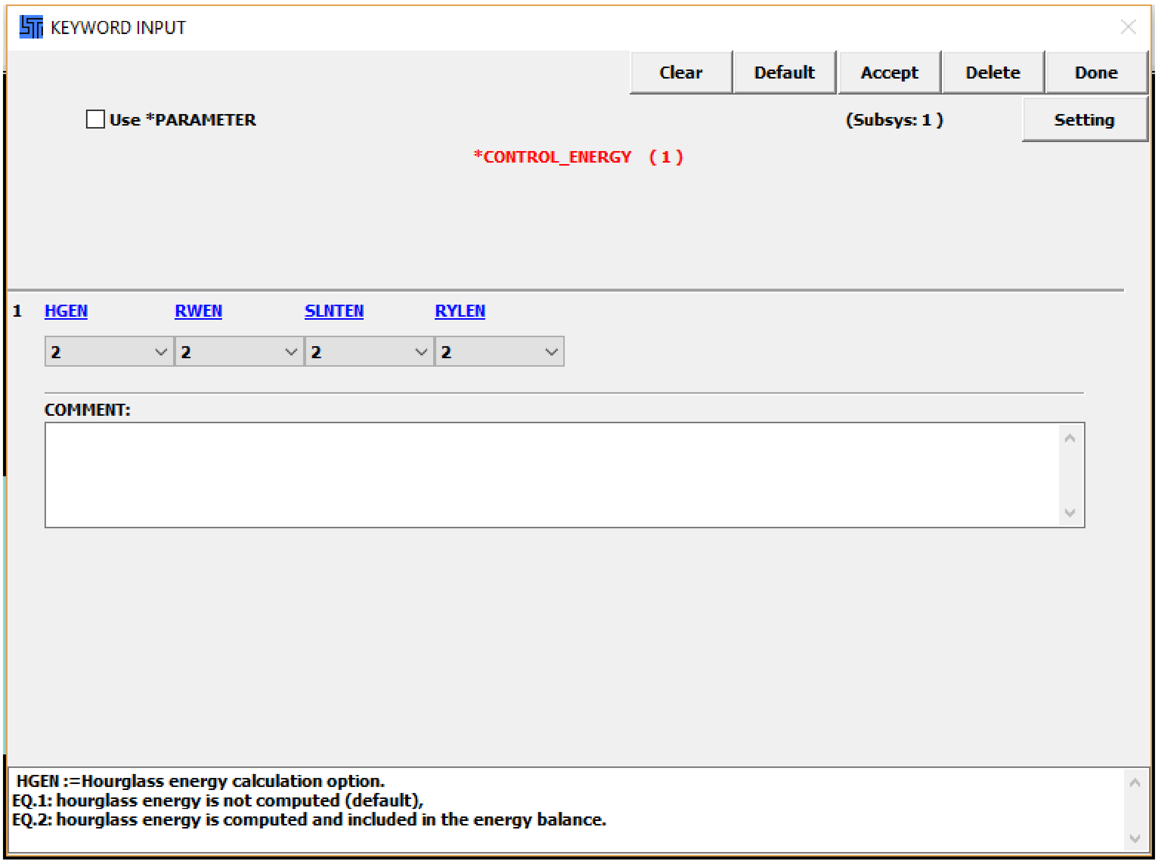

Figure 5. 17: Energy Control in Ls-Dyna keyword file

The hourglass is an energy free strain state that occurs in regions of a mesh containing one point integration of solids or shells.

The hour glass energy is computed and included in this energy balance analysis because of areas of concentrated loads during the crushing of the tube

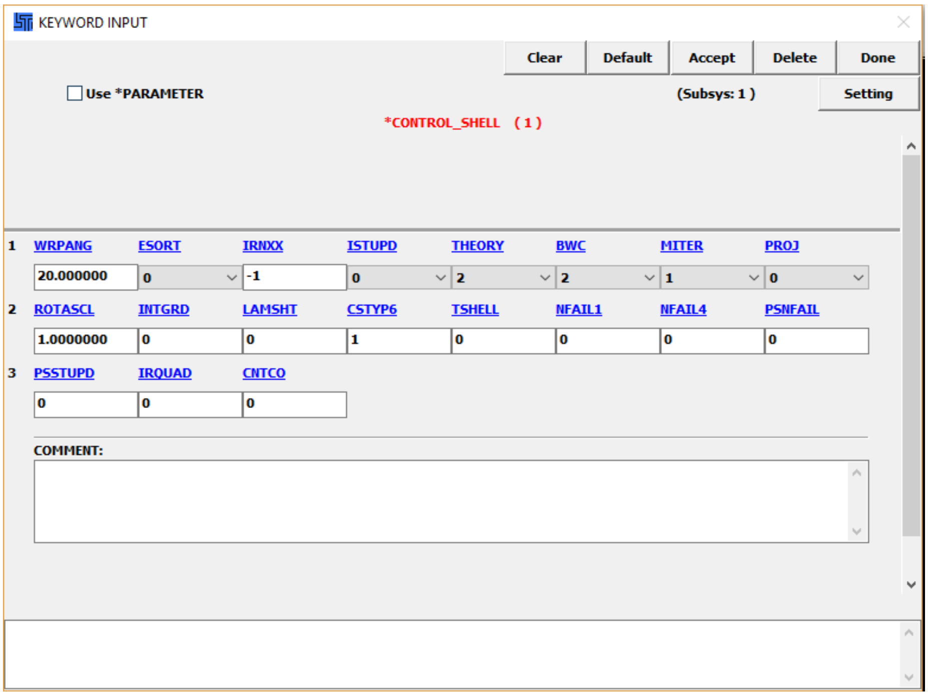

Figure 5. 18: Shell control

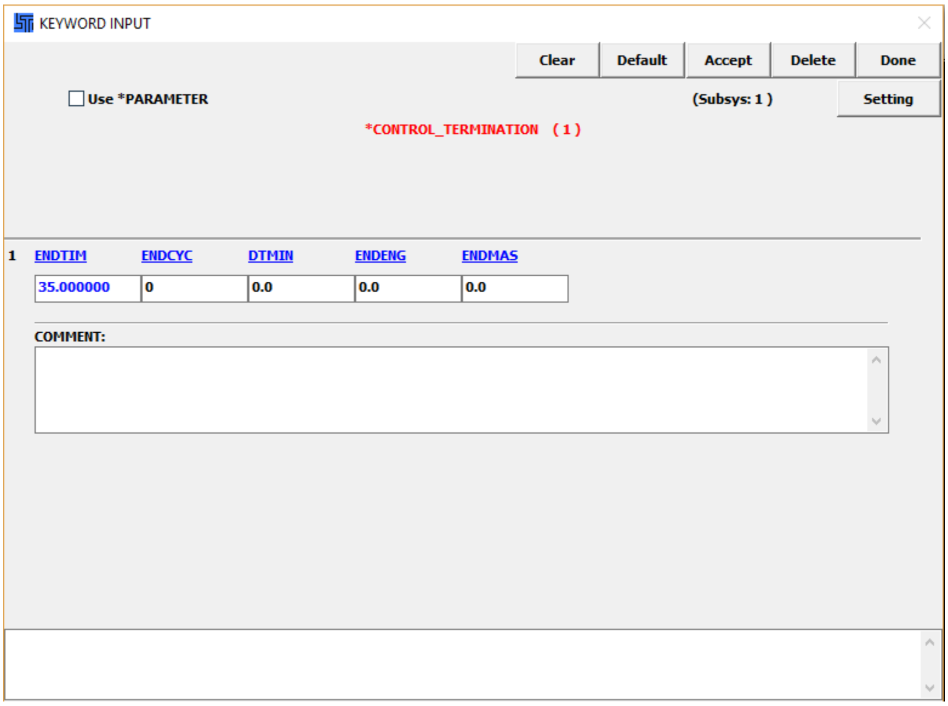

Figure 5. 19: Termination control

The termination control shown in Figure 5.18 is used to determine the condition for termination of the simulation when running.

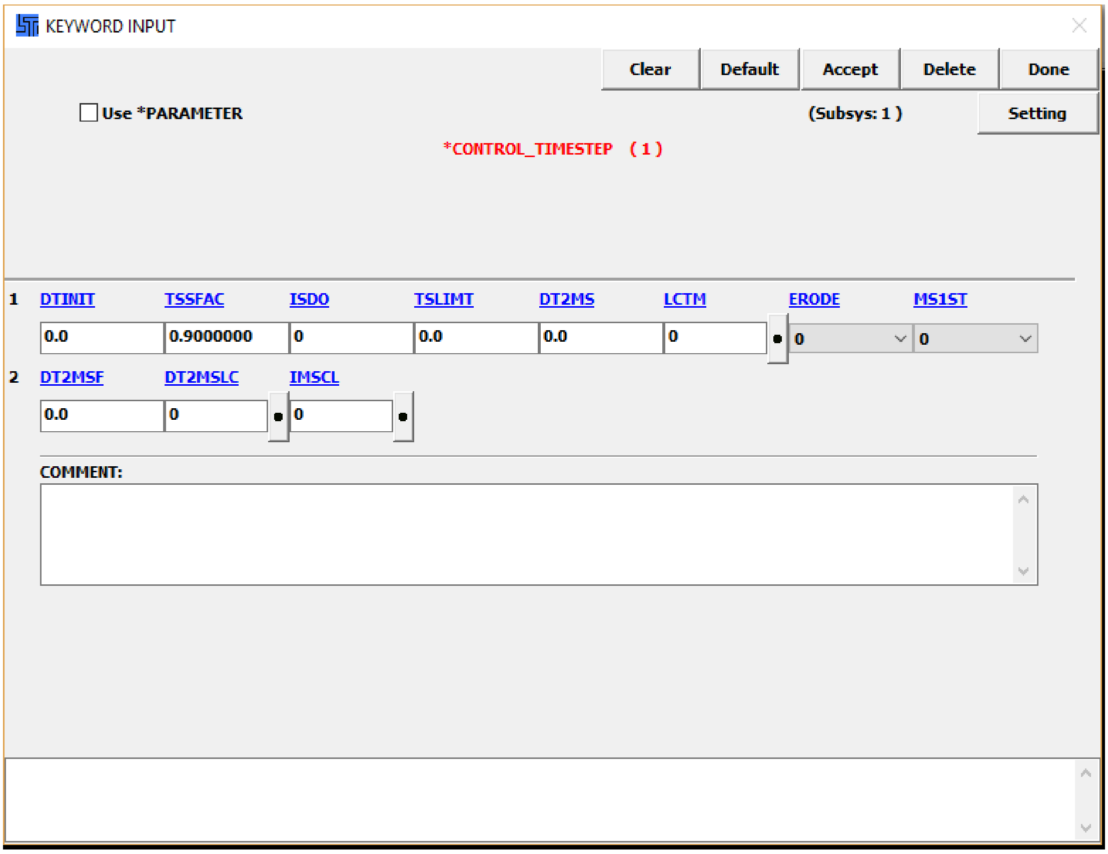

Figure 5. 20: Timestep control

5.2.5 *Define

This section is used to define and load the material property curves, velocity curves (if applicable). The defined curves can be plotted in this keyword as illustrated in Figure 5.20 and 5.21 which is a defined curve of the stress – strain curve of the mild steel obtained from literature (A.G. Mamalis, 2001) and was digitized using GetData graph digitizer.

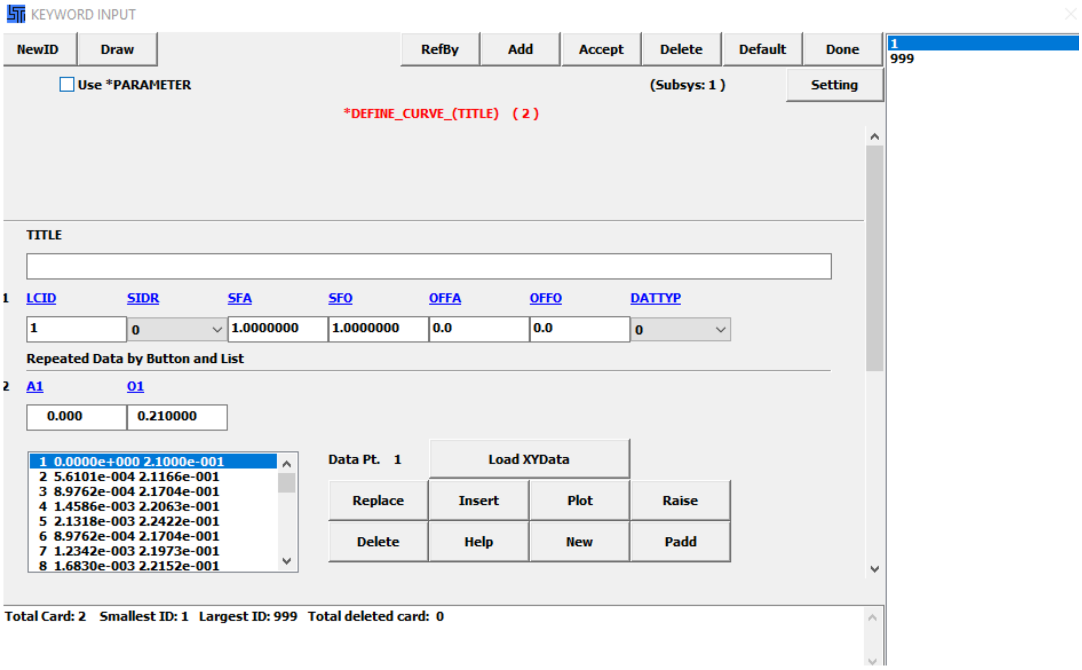

Figure 5. 21: Material property data card

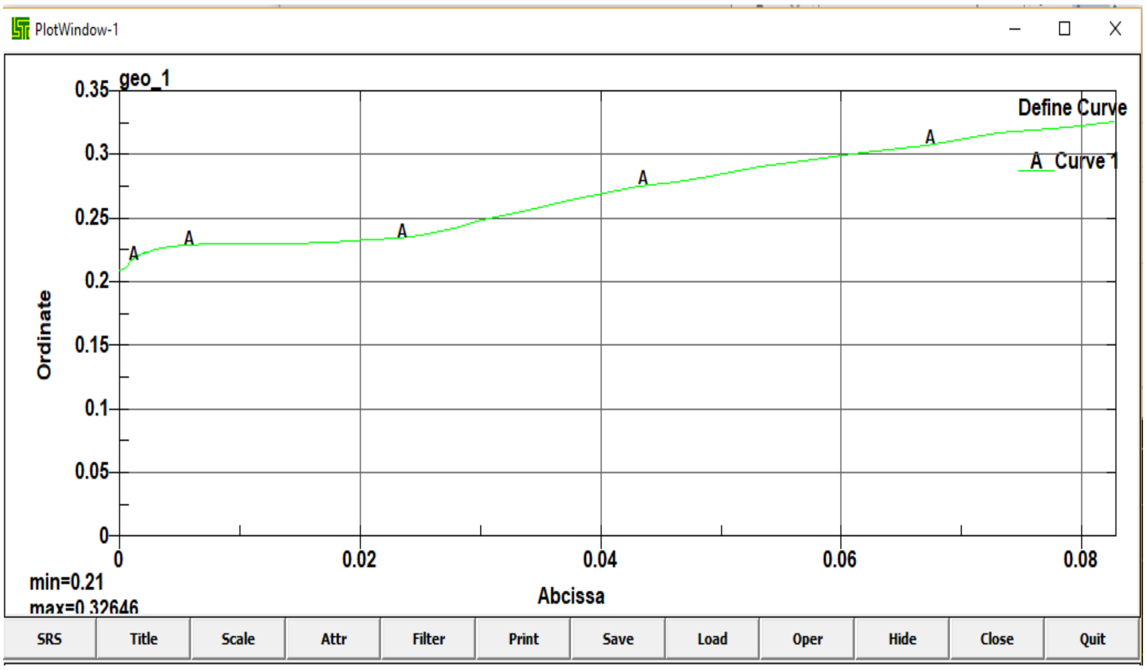

Figure 5. 22: Material stress – strain curve

5.2.6 *Part

The model is grouped into two (2) parts and must be given unique part identification number for easy referencing in Ls-Dyna. The *Part keyword is used to identify and connect the material to the geometry and section with its already defined material. This is shown in Figure 5.22 below.

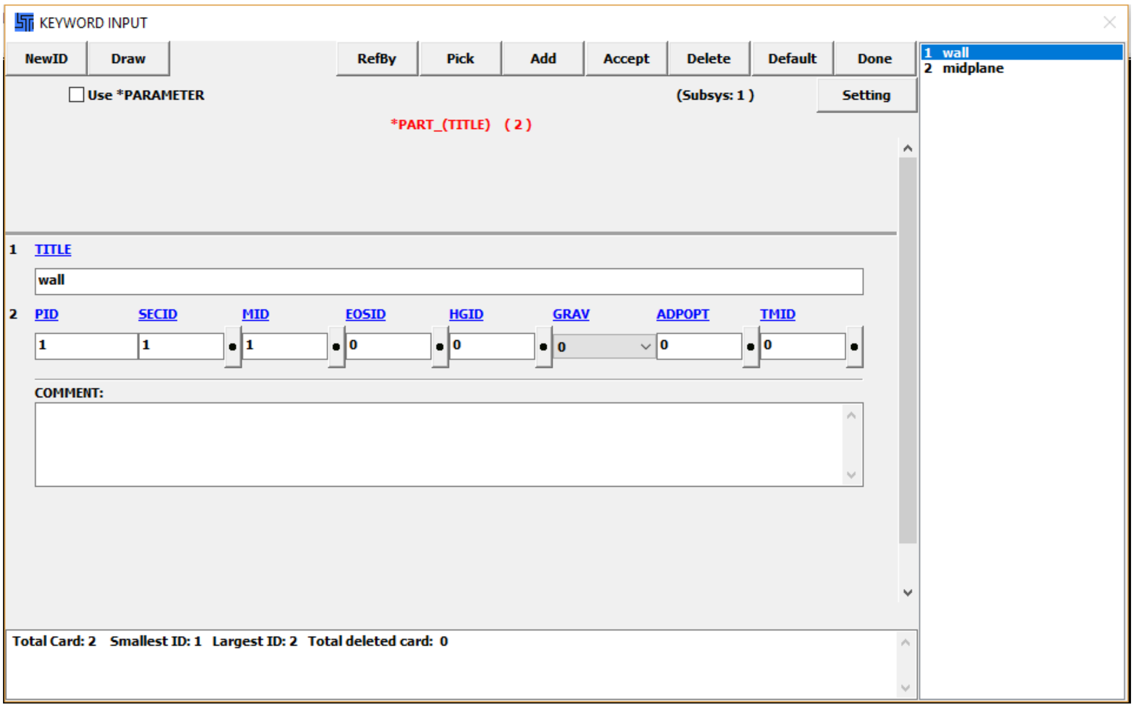

Figure 5. 23: Part title

5.2.7 *Section

Section keyword is used to add the thickness of each part identified as shown in Figure 5.24 below.

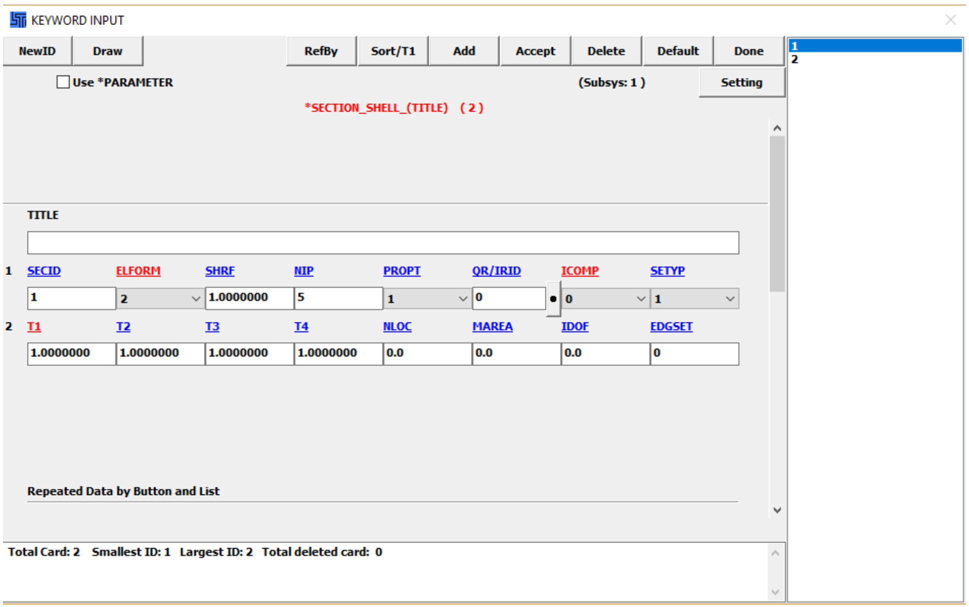

Figure 5. 24: Shell section card

5.2.8 *Set

This keyword is used to group parts together for the purpose of giving boundary conditions to a group of parts. The *set keyword card for this project is shown below in Figure 5.24.

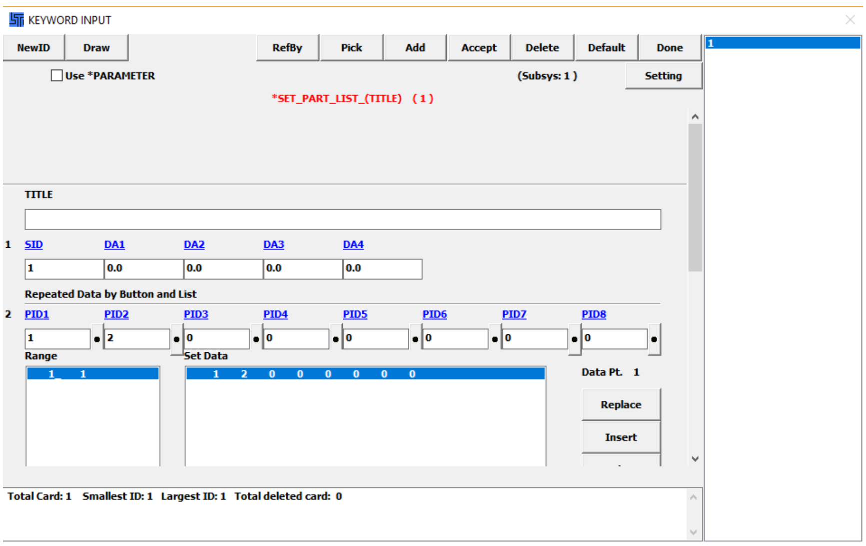

Figure 5. 25: Set part list card

After setting up all the keyword cards, the material card is saved as “sample_run.k” format. Before starting up the simulation in ls-dyna, it is important to save the “nodes_elements.k and “sample_run.k” in the same folder.

5.3 Ls-Dyna

The Ls-Dyna program is used for the finite element analysis using the “sample_run.k” file.

The “sample_run.k” file is inserted into Ls-Dyna and the number of CPU (NCPU) is selected depending on the number of cores of the computer being used. Figure 5.25 shows the startup page for file input in Ls-Dyna.

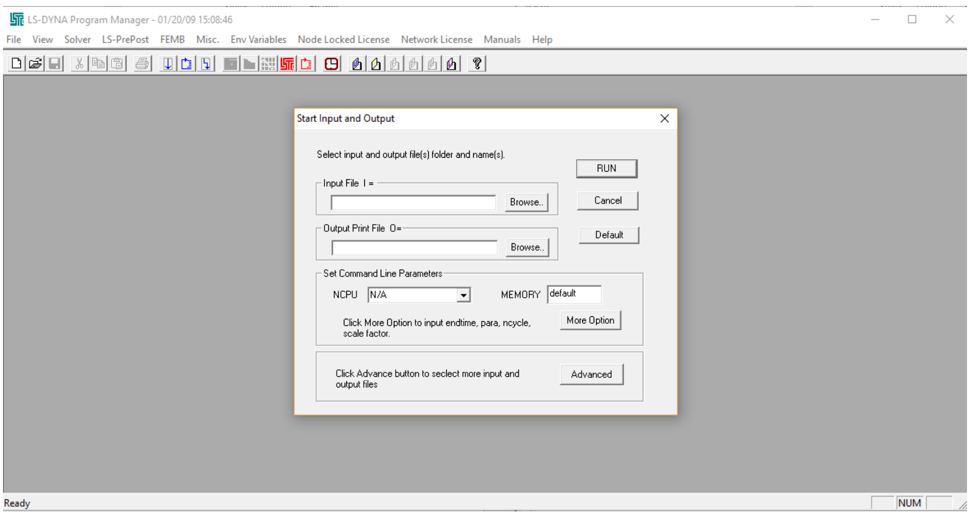

Figure 5. 26: Ls-Dyna interface

5.4 Post Processing

This is the user interface Ls-Dyna uses for results viewing. The Ls-Dyna simulation creates a file named “d3plot” which contains the results of the simulation ready for viewing in the post process. The “d3plot” file is opened on the pre-post to view the animation of simulation and also to gain access to the “ASCII” command to view Energy – time curve, Force – time and displacement – time curves. In order to further explain the post processing of Ls-Dyna, the first run is selected i.e the first run of the first specimen corresponding to the specimen of 5^{o} semi apical angle, 0.97mm wall thickness with 6.05 m/s velocity.

5.4.1 The Energy – time graph in Ls- Dyna post process

To obtain this graph, the "ASCII" command is clicked on the first menu list and the "matsum*" command is selected as shown in Figure 5.26 below. The matsum data are obtained from the tube.

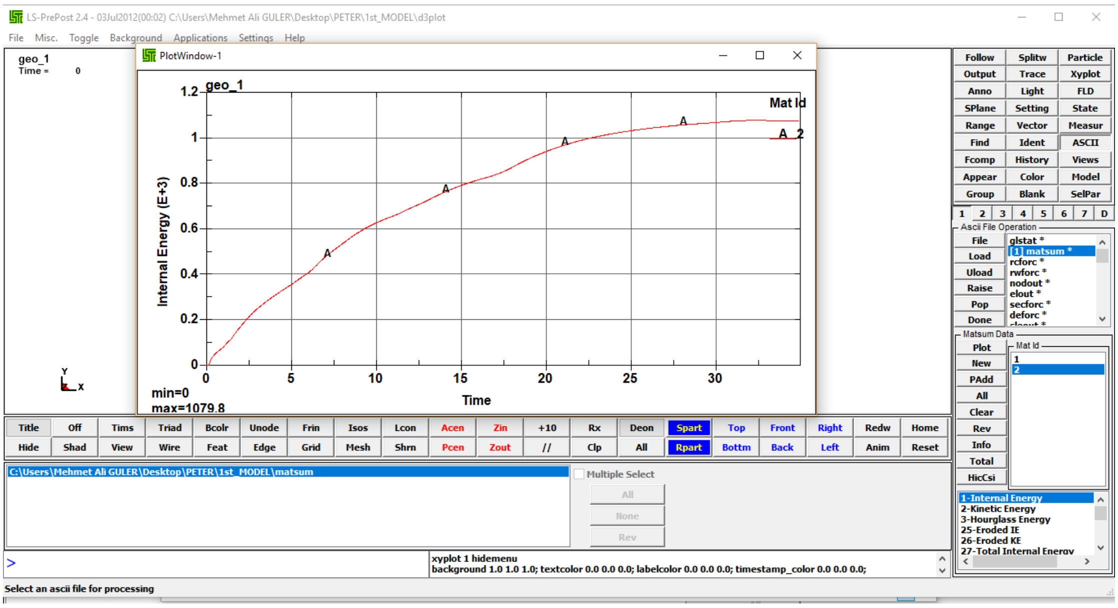

Figure 5. 27: Energy - time graph

5.4.2 The Force – time graph in Ls-Dyna post process

To obtain this graph, the “ASCII” command is selected from the first list menu, then the “rwforc” is selected then the load button is clicked to display the data processed titled “wall”; this is selected then the “x – force” is selected and finally the plot button is clicked to display the graph. This force – time graph is shown in Figure 5.27 below.

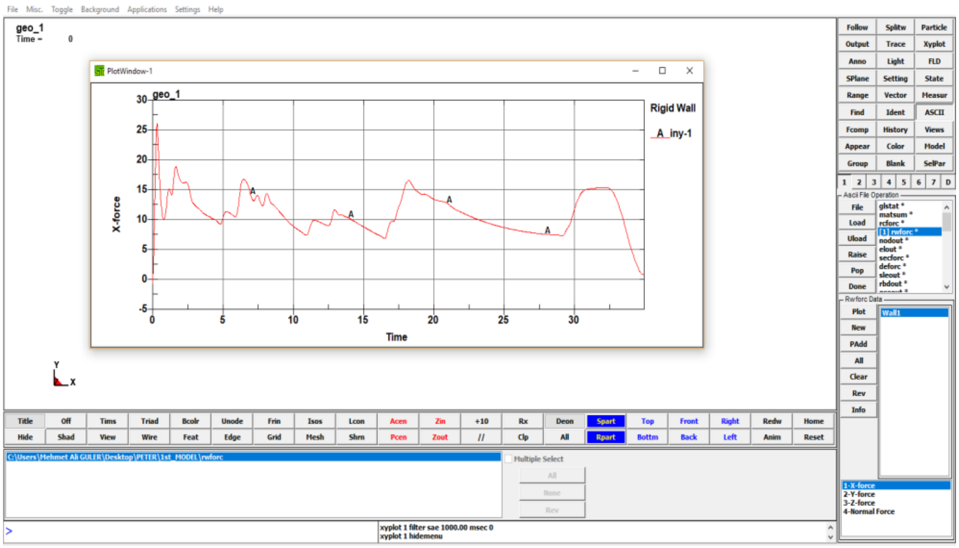

Figure 5. 28: Force - Time Graph in Ls-prepost

5.4.3 The Displacement – time graph in Ls-Dyna post process

The “ASCII” command is selected to show the ASCII files and the “nodout*” option is selected because this option records the movement of the node identified as “99999” on the moving surface. The process is shown in Figure 5.28 below.

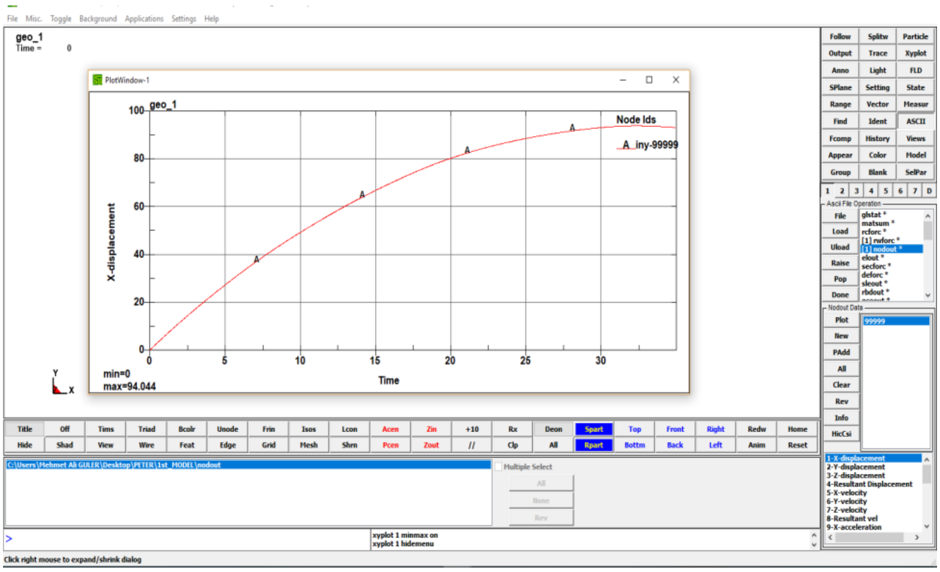

Figure 5. 29: Displacement - time graph in Ls- prepost

5.4.4 The Force – displacement graph in Ls- Dyna post process

To obtain this curve the “XYPLOT” command is selected, afterwards the Displacement – time and force – time graphs are loaded then used as “crossed” plot as described in Figure 5.29 below.

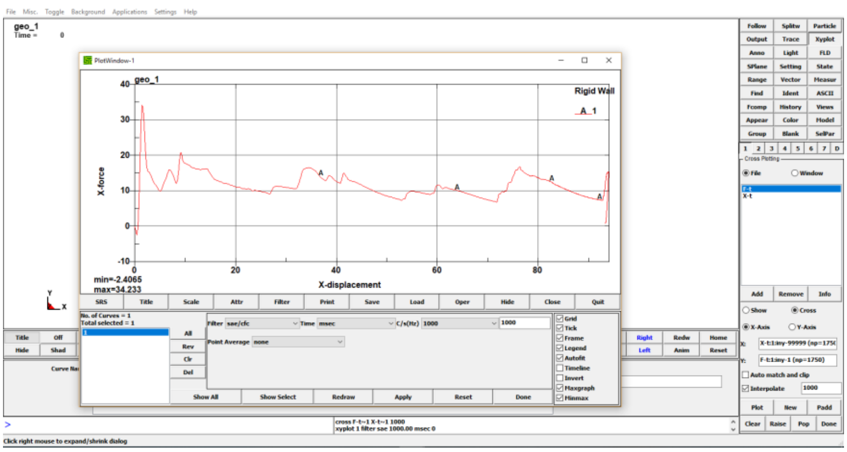

Figure 5. 30*:* Force - displacement graph displayed on ls-prepost

5.4.5 The Energy – displacement graph in Ls-Dyna post process

To obtain energy versus displacement curve the “XYPLOT” command is selected, afterwards the Displacement – time and energy – time graphs are loaded then used as “crossed” plot as described in Figure 5.30 below;

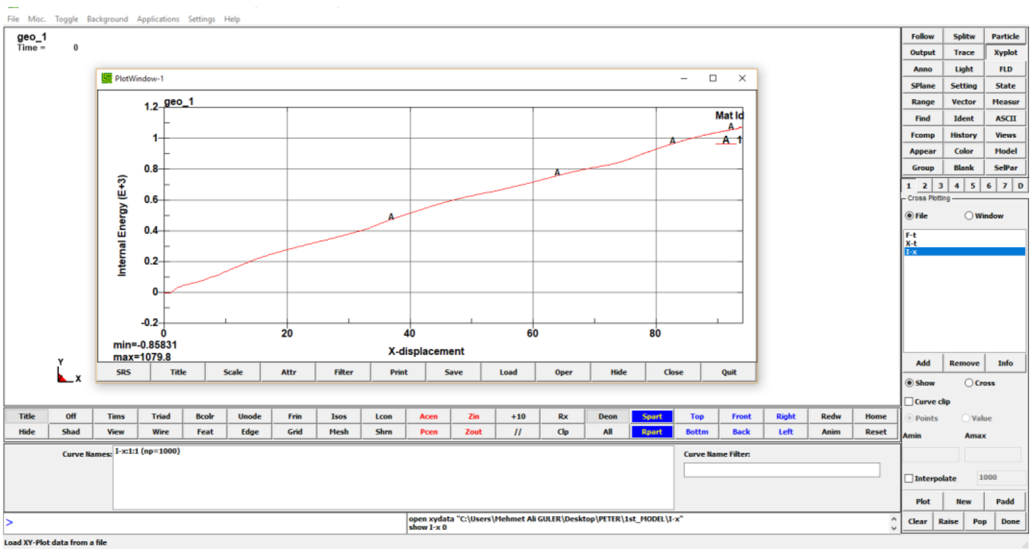

Figure 5. 31: Energy - displacement graph displayed on Ls-Prepost

5.4.6 Specimen mass calculation

The “d3hsp” records the mass of the parts used in the simulations. “notepad++” is used to read and open the “d3hsp” file so as to obtain the masses of the parts as shown in Figure 5.31.

```
***********************************************************

NOTE : For 2D axisymmetric problems the following
       masses are reported per radian.
       For 2D plain strain/stress problems the
       masses are reported per unit thickness.

summary of mass
moving rigidwalls              mass= 0.60000000E+02
part id   =        1   mass= 0.21834034E-01 rigid body
part id   =        2   mass= 0.16253299E+00 mass in rigid body= 0.22832381E-02

t o t a l  m a s s           = 0.60182083E+02
x-coordinate of mass center = 0.53118168E+02
y-coordinate of mass center =-0.25464006E+02
z-coordinate of mass center = 0.25000000E+02


***********************************************************
```

Figure 5. 32*:* Mass calculation from d3hsp file

5.5 Deformation modes of crash box

For the purpose of graphical display in this section, the deformation mode of the first specimen at 6.05m/s speed is captured at 8.1 ms, 18.2 ms and 34.7 ms and shown in Figure 5.32, 5.33, and 5.34 respectively.

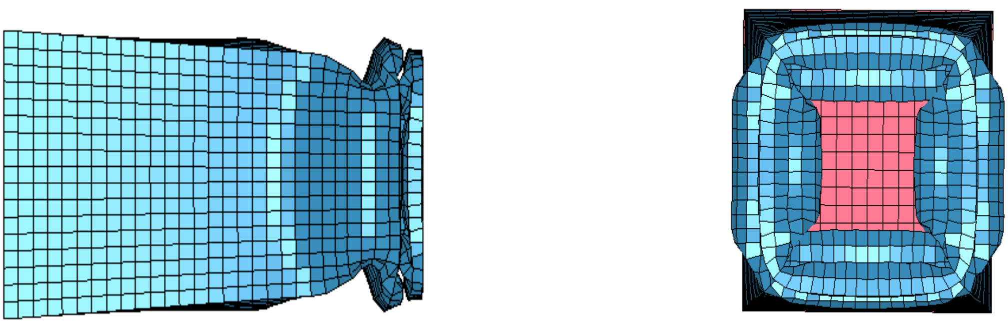

Figure 5. 33*:* Deformation mode of specimen 1 at 8.1 milliseconds during impact at 6.05m/s velocity.

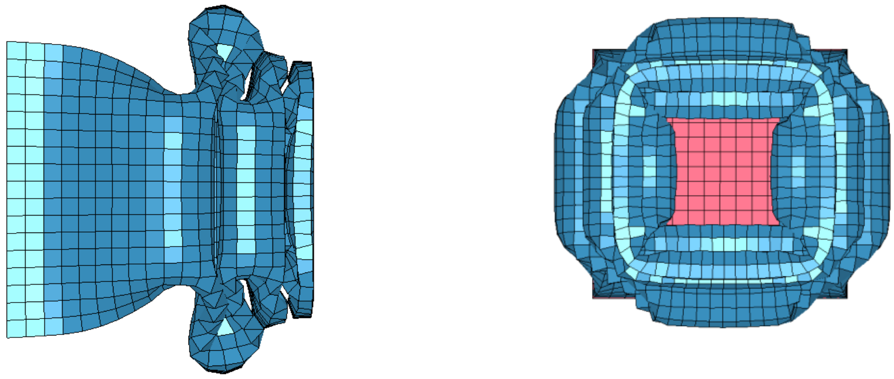

Figure 5. 34*:* Deformation mode of specimen 1 at 18.2 milliseconds during impact at 6.05m/s velocity

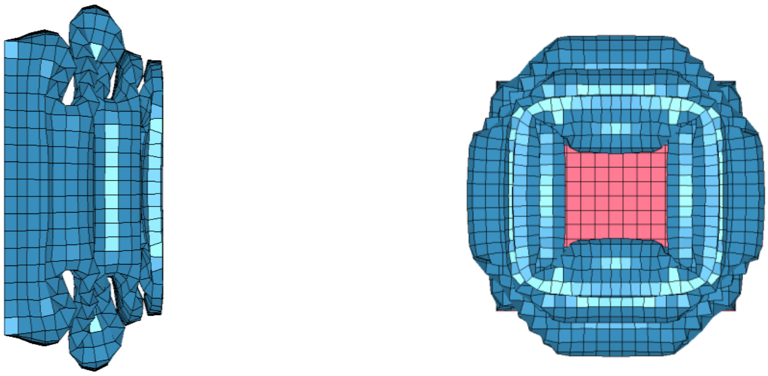

Figure 5. 35*:* Deformation mode of specimen 1 at 34.7 milliseconds during impact at 6.05m/s velocity

CHAPTER 6

RESULTS AND DISCUSSION

The analysis were conducted to determine EA (Energy Absorbed), SEA (Specific Energy Absorbed), mass, IPCF (Initial Peak Crush Force), Pm (Mean Crush Force) and CFE (Crash Force Efficiency). These parameters are used to judge the performance of a crash box thus are calculated and given in Table 6.1 below for all the specimens indicating their performances at various speed levels. The values of the result shown in Table 6.1 are obtained for a deformation length of 90mm for all specimen.

The above mentioned parameters are calculated using Equations 2.8 to 2.11 given in chapter 2, except the mass that is recorded by the Ls-Dyna d3hsp file.

6.1 Force – displacement and Energy absorbed - displacement curves

In this section the force – displacement curves are drawn using the data obtained from simulation. These curves are shown in Figure 6.1 – 6.4 for specimen 1, 2, 3 and 4 respectively. This graphs are used to understand the relationship of the crush force with displacement as the crushing progresses along the axis of the tube.

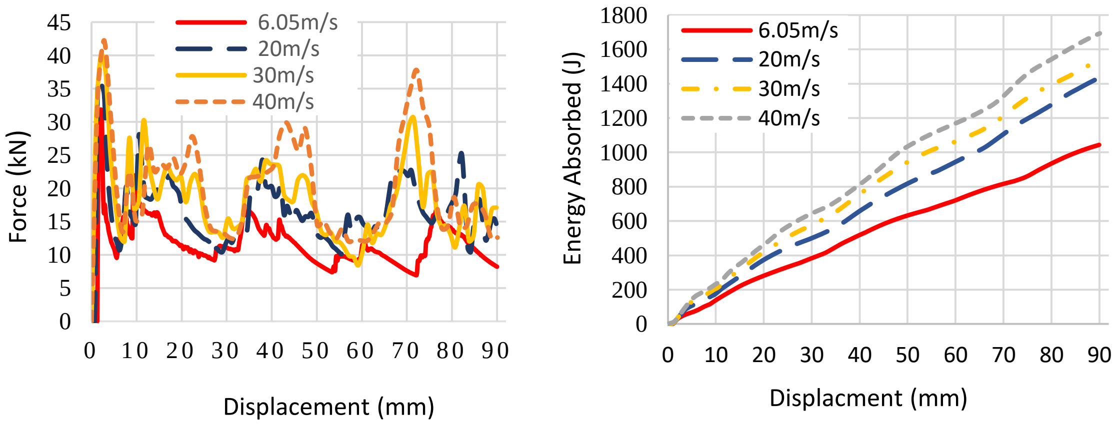

Figure 6. 1: Force – displacement and EA - displacement graph for specimen 1 at various speed

Table 6. 1: Performance parameters of specimens under various speed

		Specimen 1		
Velocity (m/s)	**6.05**	**20**	**30**	**40**
Initial peak force (kN)	34.233	36.547	40.166	42.265
Maximum Force (kN)	34.233	36.547	40.166	42.265
Absorbed energy (j)	1079.8	1435.9	1539.8	1692.4
Specific absorbed energy (j/kg)	6551.53	8707.2	9342.5	10268.4
Mean force (kN)	11.998	15.95	17.11	18.80
Crush force efficiency (%)	35.05	43.63	42.6	44.49
		Specimen 2		
Velocity (m/s)	**9.1**	**20**	**30**	**40**
Initial peak force (kN)	53.329	57.497	62.966	66.102
Maximum Force (kN)	53.329	57.497	68.191	84.091
Absorbed energy (j)	2427.2	2712.35	2973.5	3202.2
Specific absorbed energy (j/kg)	8873.3	9913.7	10868.21	11704.11
Mean force (kN)	26.97	30.14	33.039	35.58
Crush force efficiency (%)	50.58	52.42	48.45	42.31
		Specimen 3		
Velocity (m/s)	**9.25**	**20**	**30**	**40**
Initial peak force (kN)	43.18	47.124	50.379	53.226
Maximum Force (kN)	48.648	61.953	68.151	84.191
Absorbed energy (j)	2525.1	2938.7	3113.9	3318.3
Specific absorbed energy (j/kg)	9593.071	11164.37	11829.97	12606.51
Mean force (kN)	28.057	32.6522	34.599	36.87
Crush force efficiency (%)	57.673	52.71	50.77	43.79
		Specimen 4		
Velocity (m/s)	**8.7**	**20**	**30**	**40**
Initial peak force (kN)	21.428	21.609	22.236	22.352
Maximum Force (kN)	39.77	42.569	61.087	69.296
Absorbed energy (j)	2020.4	2107.7	2276.2	2426.4
Specific absorbed energy (j/kg)	9719.79	10139.78	10950.4	11672.99
Mean force (kN)	22.45	23.42	25.29	26.96
Crush force efficiency (%)	56.45	55.01	41.40	38.91

The first peaks of the 4 runs for specimen 1 occurred before 5mm displacement which is the elastic region before the first fold was formed at about 5mm displacement after which there was a drop in force until a new fold was formed.

The last peak force in the force – displacement curve of all the runs of specimen 1 shown in Figure 6.1 is higher for the 40m/s impact velocity due to strain hardening as the material crumbles axially the strain working becomes saturated.

In the force – displacement curve of specimen 1 shown in Figure 6.1 above, the run at 6.05m/s and 20m/s are having similar characteristics with an offset on the run of 20m/s due to increased force but the behavior of the force along the axial direction of the tube as the crushing progresses is similar while the 30m/s and 40m/s runs are slightly similar.

The energy absorbed increases as the crushing progresses along the axis of the crash box. The energy absorption levels are higher at higher speed levels. This behavior is accounted for by the reason of the requirement of higher magnitude forces to cause the walls of the crash box to collapse.

For specimen 1, at 6.05m/s there is a total energy absorbed of about 1.1kj while at 40m/s impact velocity the total amount of energy absorbed is about 1.7kj.

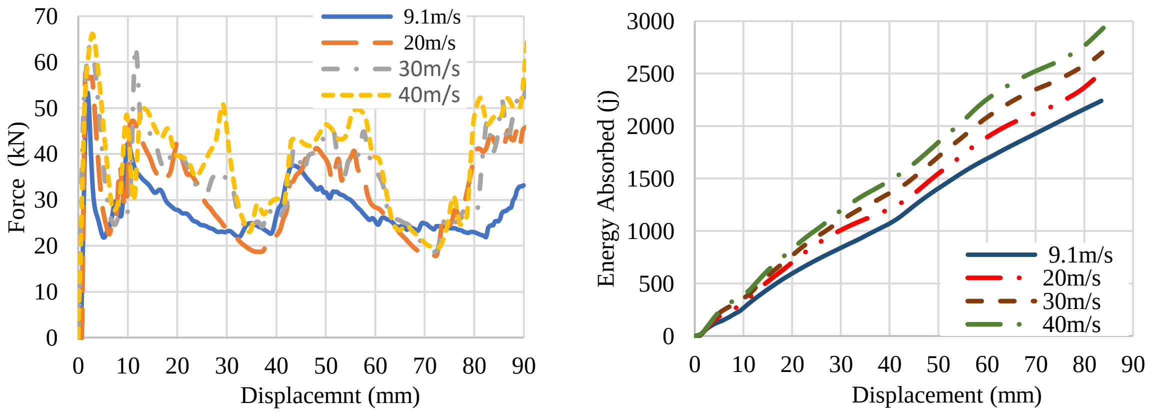

Figure 6. 2: Force – displacement and Energy Absorbed – Displacement curves of specimen 2 under various speed

The continuous increasing peaks of the forces along the axial displacement is a strong indication of strain hardening which is caused by large plastic deformation. Strain hardening causes higher peaks due to the dislocation and movement of the crystal structure of the material as the crushing progresses.

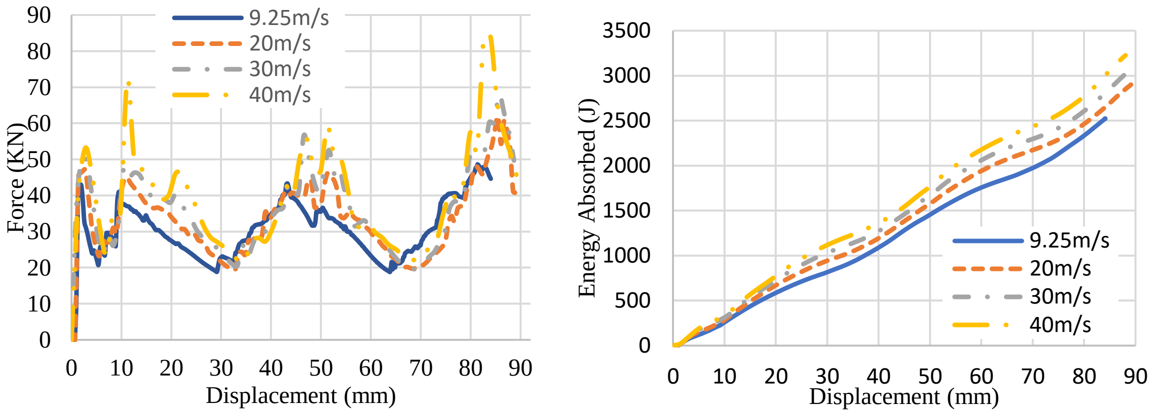

Figure 6. 3: Force – displacement and Energy absorbed - displacement graph for specimen 3 at various speed

As the crash box is being crushed, the dislocation and movements of the crystals of the materials increases and therefore causes a level of saturation of newly formed dislocations. The newly formed dislocations acts as resistance to further dislocation which becomes physical observed as the materials resistance to further plastic deformation therefore causing a demand for more force to continue the crushing of the crash boxes. This behavior is more noticeable on the Force – Displacement curves of specimen 4 shown in Figure 6.4.

As the crushing continues the peaking of the forces increases alongside meaning more force is required to initiate crumbling of the formed fold of the walls of the crash box because the material of the crash box used in this study is Mild Steel AISI 1021 which possesses strain hardenability.

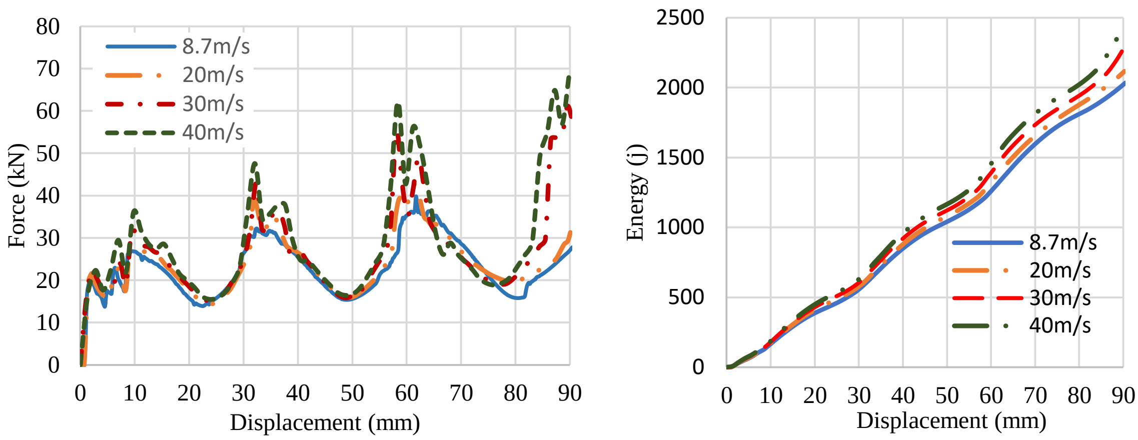

Figure 6. 4: Force - displacement and Energy absorbed – displacement graph of specimen 4 at various speed

The force – displacement curves of all the specimen in a total of 16 runs (4 runs for each specimen) shows that there are critical points as the tubes are being crushed axially. These points are the peaking and valleys of these curves.

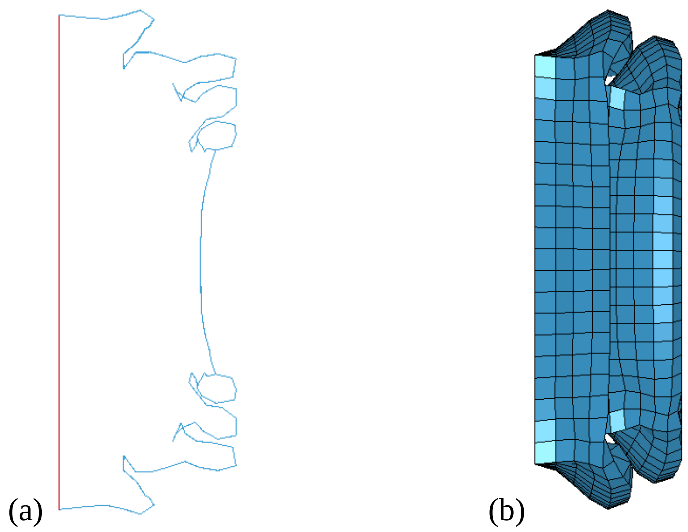

Figure 6. 5: Fold pattern of specimen 3 at 40m/s impact velocity (a. model feature line view and b. model shadow and mesh view.

The peaking and valley points of each specimen are almost same for the four (4) runs done. On a general note, the peaking indicates the initiation of a collapse of the walls of the crash boxes. While the valleys on the graphs indicates a new formation of fold.

This means that the number of visible peak and valley corresponds to the number of fold formed during the crushing of the crash box. Specimen 3 is used to illustrate this concept in Figure 6.5. For an impact velocity of 40m/s, specimen 3 has 4 folds formed which corresponds to the number of peaking and valley of specimen 3 shown in Figure 6.3.

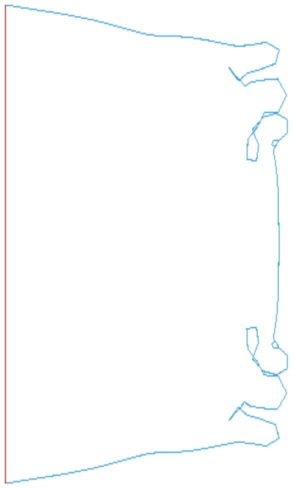

(a)

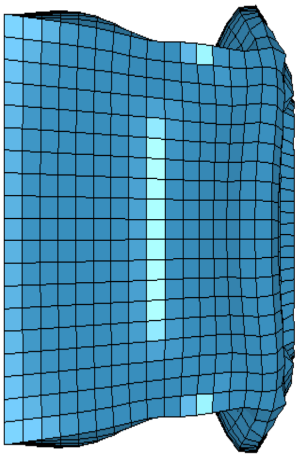

(b)

Figure 6. 6: Fold pattern of specimen 3 at 9.25m/s impact velocity (a.) model feature line view and (b) model shadow and mesh view.

Figure 6.6 illustrates the folds formed corresponding to the number of peaks found in the curve shown in Figure 6.3.

The 9.25m/s impact velocity curve of specimen 3 in Figure 6.3, there are 3 fully developed and half developed peaks and on Figure 6.6a there are 3 fully developed folds and a newly developed fold.

6.2 Energy absorbed – time curves

The energy absorbed - time curves shown in Figure 6.7 through 6.10 shows that as the impact velocity increases the time decreases for the crash box to absorb the kinetic energy at a faster rate. This behavior is same for all the four specimens.

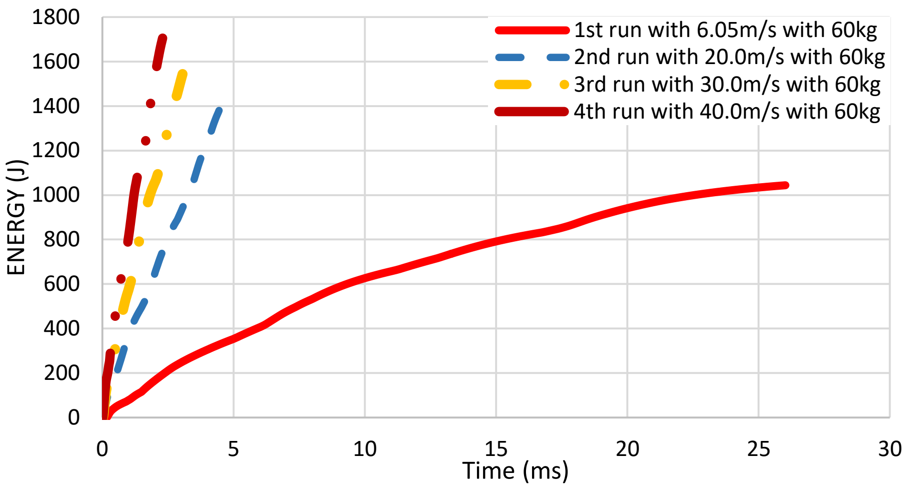

Figure 6. 7: Energy - time curve for specimen 1 at various speed

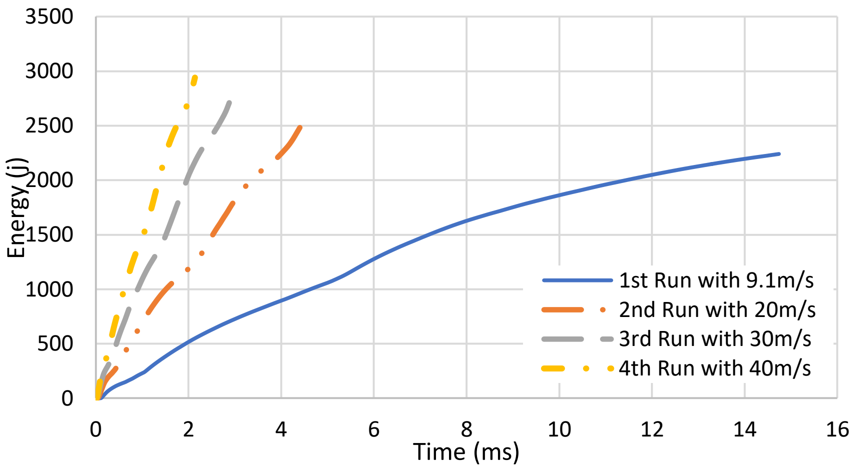

Figure 6. 8: Energy - time graph for specimen 2 under various speed

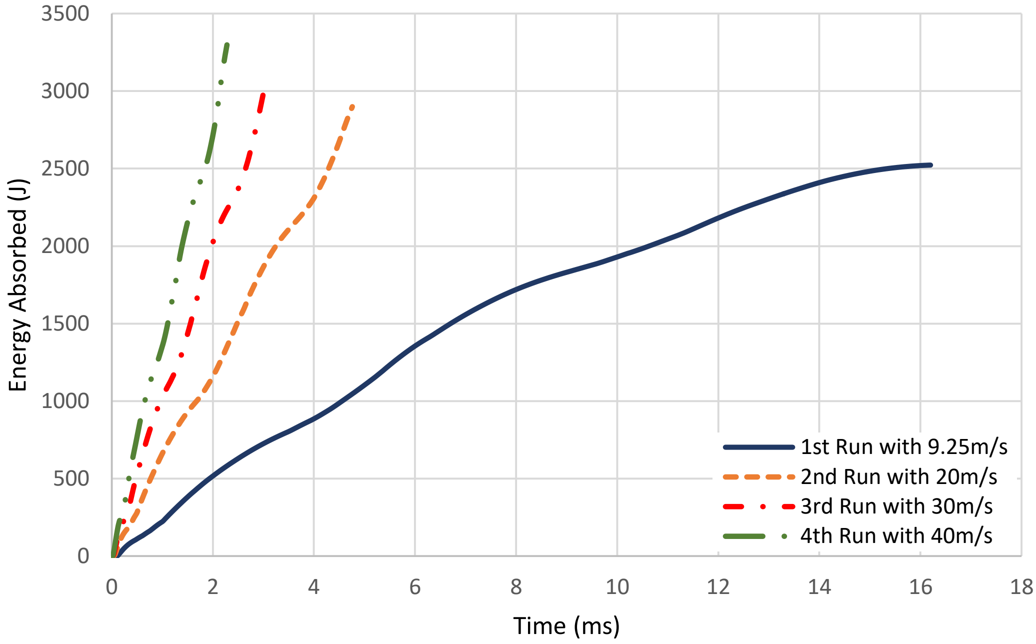

Figure 6. 9: Energy - time graphs for specimen 3 at various speeds

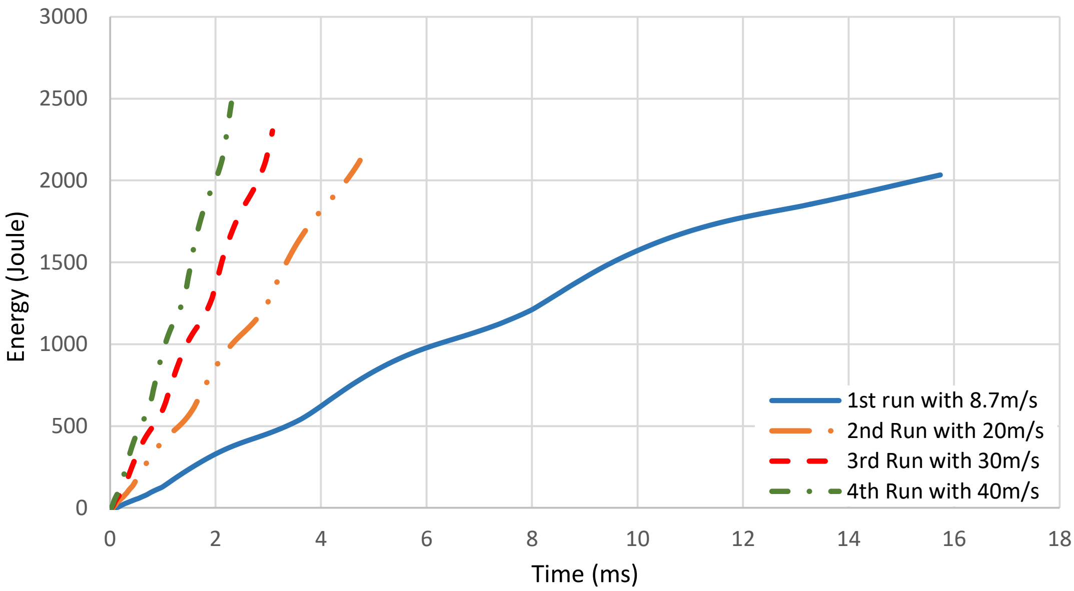

Figure 6. 10: Energy - time graphs of specimen 4 at various speed

6.3 Displacement – time curves

These curves are used to understand the relationship of the displacement of the crushing processes with time. Figure 6.11 showed that at low speed of 6.05m/s the curve tend to be parabolic but for higher impact velocity the curves tend to possess more linear characteristics

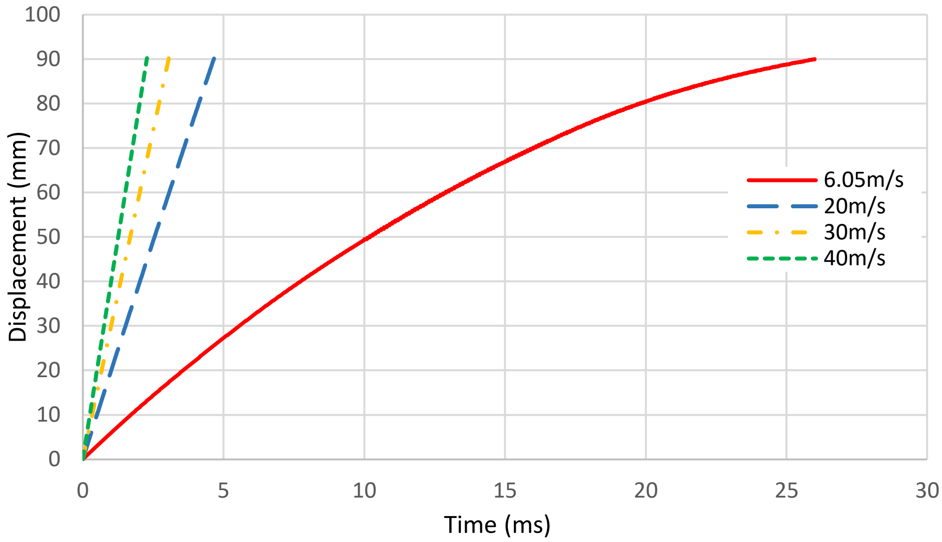

Figure 6. 11: Displacement - time graph at various speed for specimen 1

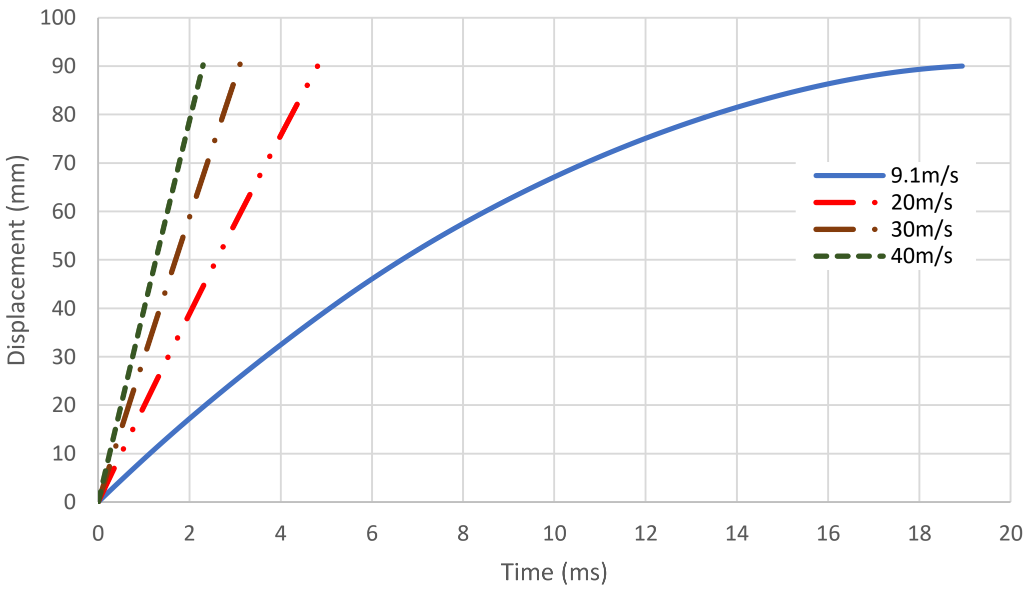

Figure 6. 12: Displacement - time graph for specimen 2 under various speed

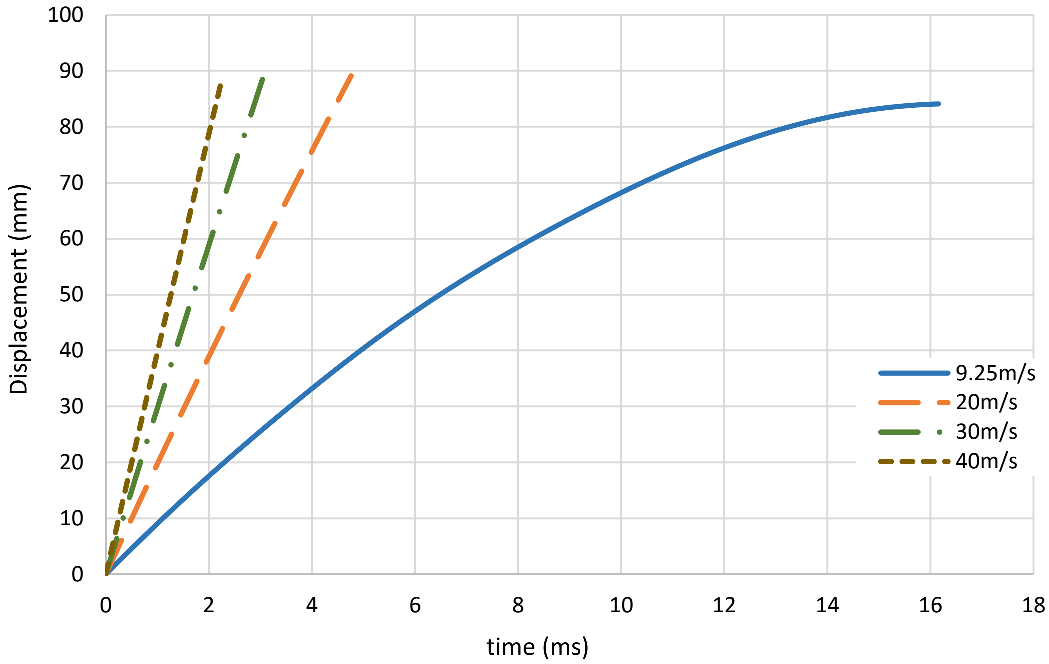

Figure 6. 13: Displacement - time graph for specimen 3 at various speed

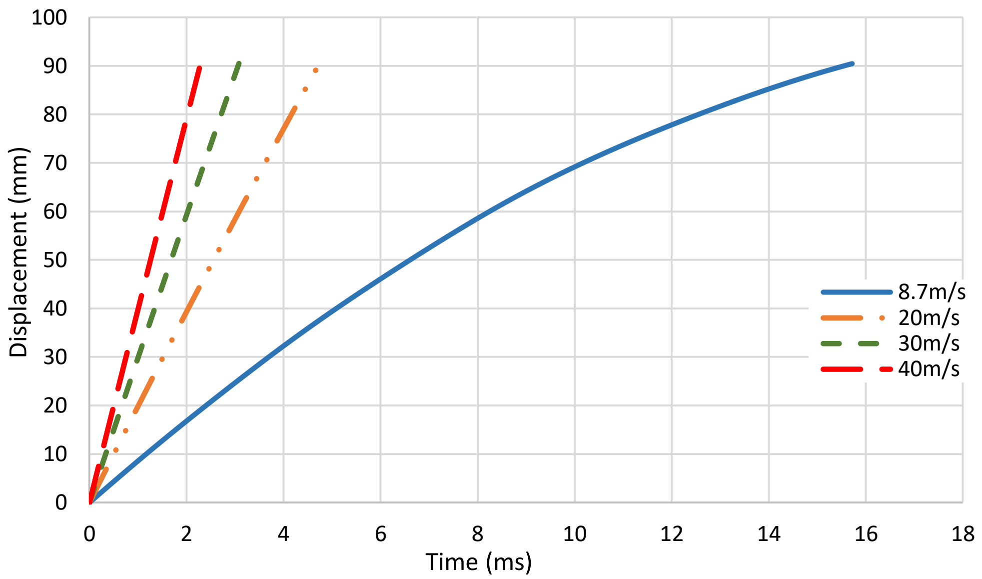

Figure 6. 14: Displacement - time graphs of specimen 4 at various speed

6.4 Velocity – time curves

The velocity – time graph of specimen 1 to specimen 4 is given in Figures 6.17 to 6.20 shown below.

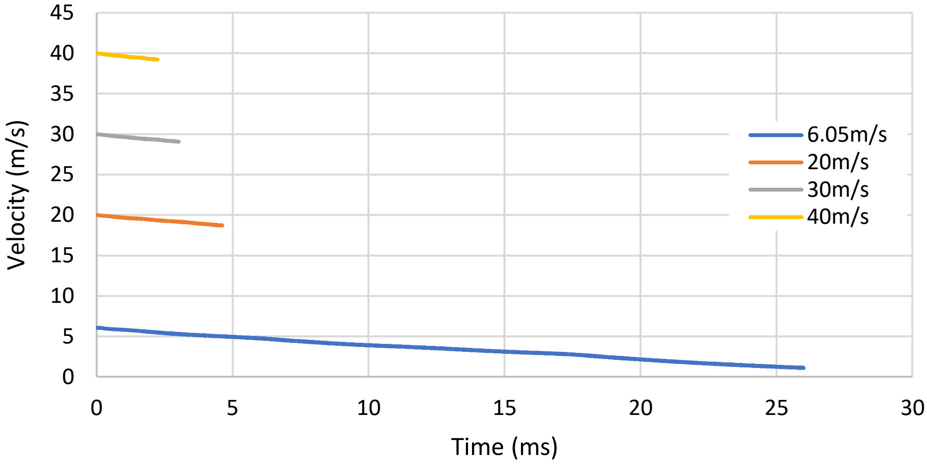

Figure 6. 15: Velocity - time graph of specimen 1 at various speed

The velocity – time curve of specimen 1 given in Figure 6.17 above is taken at a deformation length of 89.5mm. At 89.5mm a 6.05m/s moving wall is not on a complete stop but having a velocity of 1.16m/s. While at higher speed levels the moving wall crushes the tube completely and some scenarios the tube was crushed backed beyond the rigid wall in the simulation.

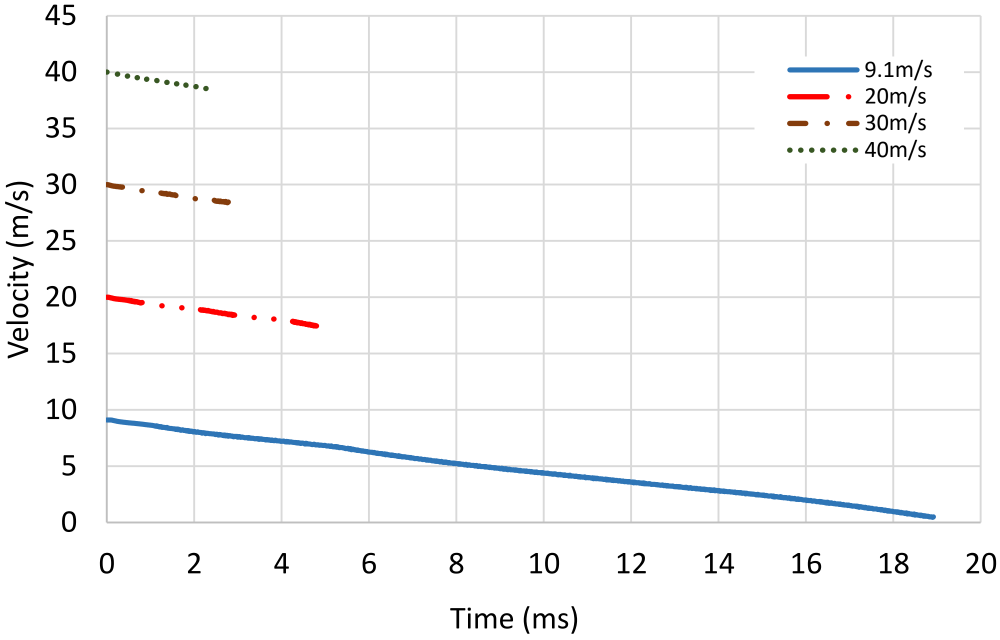

Figure 6. 16: Velocity - time graph for specimen 2 under various speed

The velocity – time curves of all the four (4) specimen shown in Figure 6.17 through 6.20 reveals that the at higher speed, the deformation length of the crash box becomes insufficient to absorb all the impact energy. This conclusion is drawn as at the end of deformed length and in some cases the whole specimen, the rigid wall continues to propagate its motion.

In order to gain better performance under high speeds, it is proposed that the length and thickness of the crash box must be increased in order for the crash box to be capable to absorb the impact energy without the rigid wall moving beyond the length of the crash box.

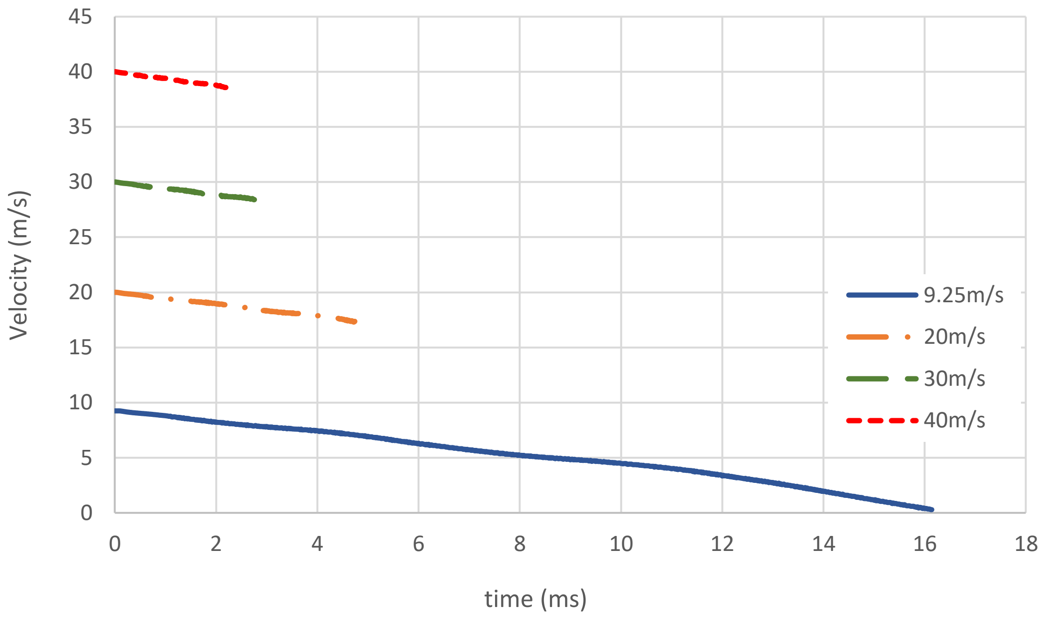

Figure 6. 17: Velocity - time graph of specimen 3 at various speed

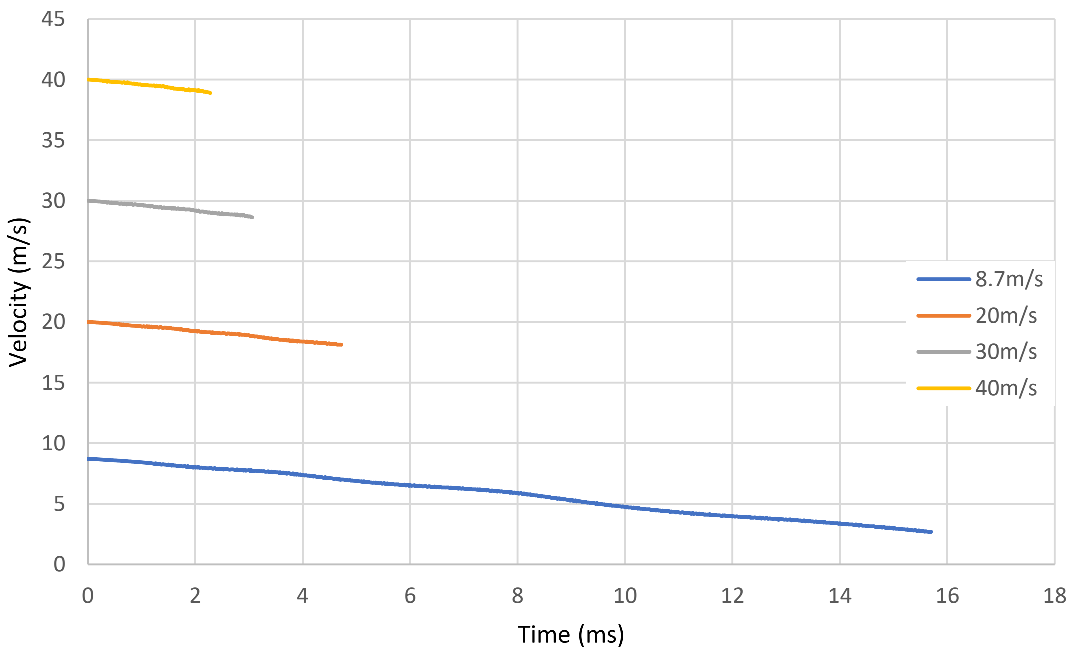

Figure 6. 18: Velocity - time graphs of specimen 4 at various speeds

6.5 Force – time curves

The force – time curves is needful in understanding the impulse and response of the crash box under different speeding condition.

Figure 6.21 to 6.24 is the force – time curves of specimen 1 to 4 respectively. These curves possesses similar behavior as the speed increases the time needed to complete the crushing decreases and the force wavelength decreases as the speed increases. Meaning the frequency of the fluctuating magnitude of the forces increases as the speed increases.

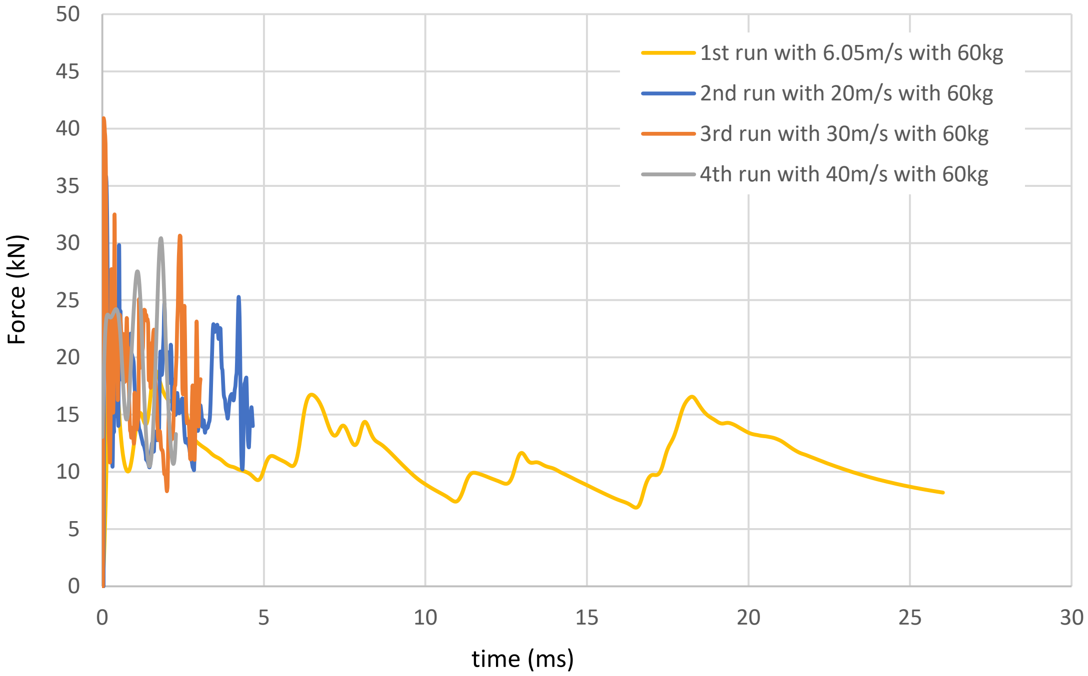

Figure 6. 19: Force - time graph of specimen 1 at various speed

From the force – time curves given in Figures 6.21 to 6.24, the peaking of the forces increases in magnitude and the rising and falling slopes become steeper as the speed increases. This is due to the rapid collapse of the walls of the tube during fold formation when impacted at high speeds.

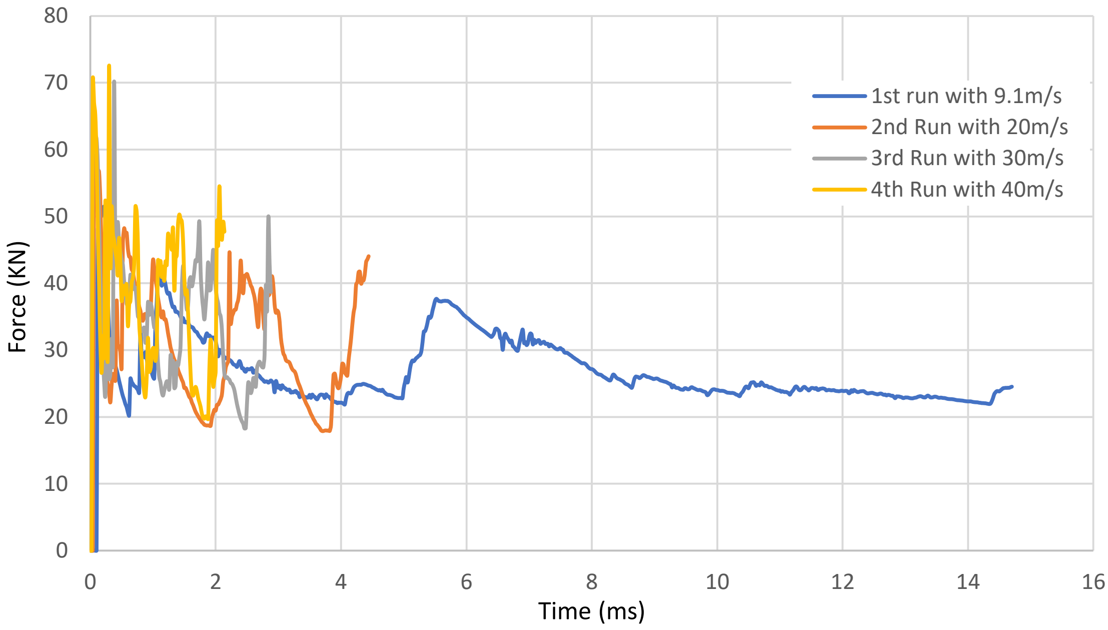

Figure 6. 20: Force - time curve for specimen 2 under various speed

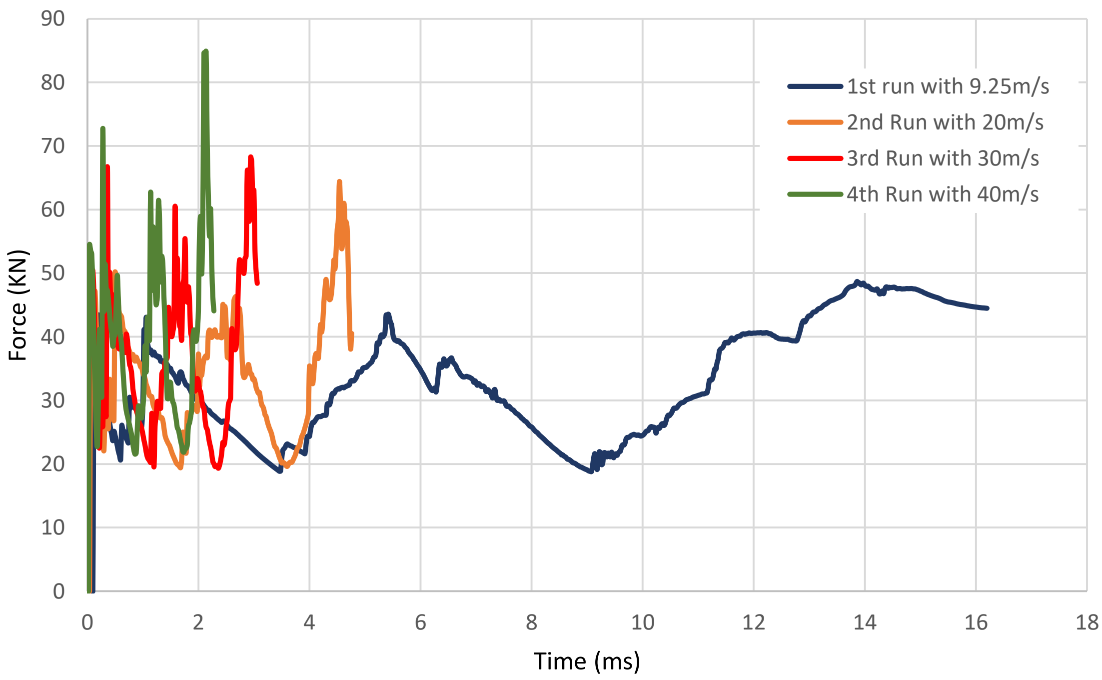

Figure 6. 21: Force - time graphs for specimen 3 at various speeds

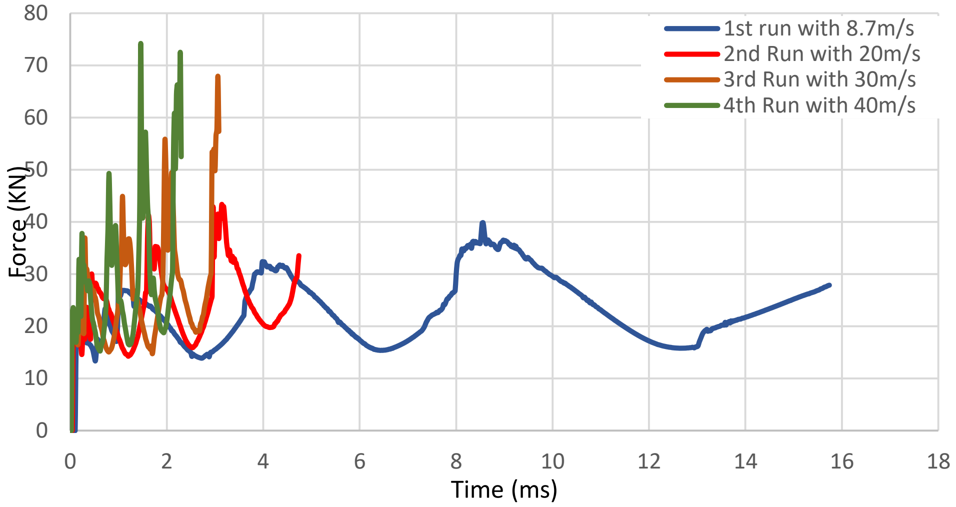

Figure 6. 22: Force - time graph for specimen 4 at various speed

6.6 Analysis of the performance of the specimens at various speed levels using principal crushing parameters.

In this sub section, the performance of the specimens used in this study will be analyzed. This analysis is done using principal parameters such as absorbed energy (Figure 6.27).

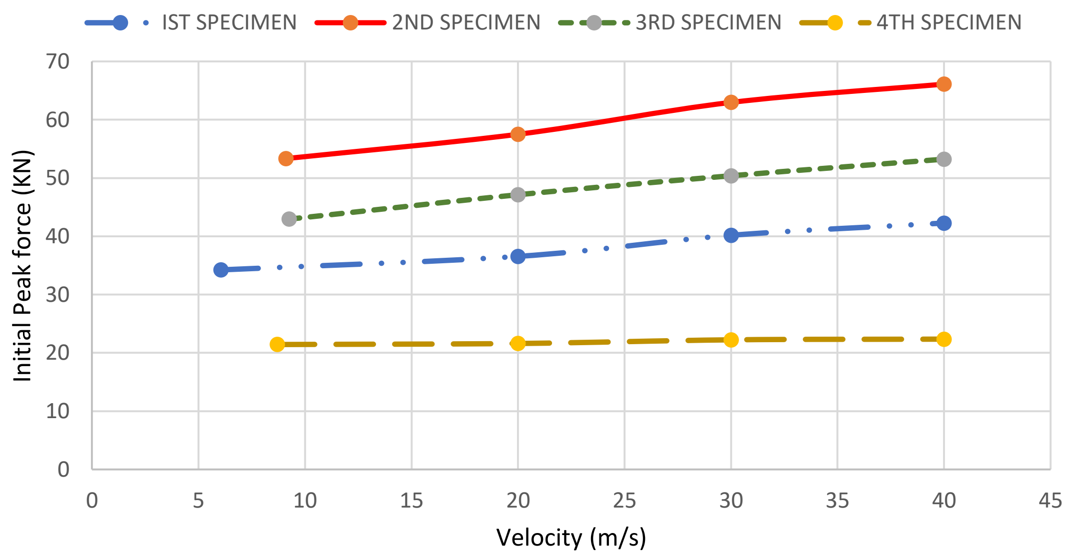

Figure 6. 23: Initial peak force - velocity graph of all four (4) specimen

Specific energy absorbed (Figure 6.28), initial peak force (Figure 6.25), mean crush force (Figure 6.26) and crush force efficiency (Figure 6.29) as discussed in Chapter 2.

As found from literatures, it is desirable for the initial peak force to be minimized as much as possible in order to enable quick initiation of plastic deformation to absorb the crash energy as much as possible without transferring the force to the occupant compartment of the vehicles.

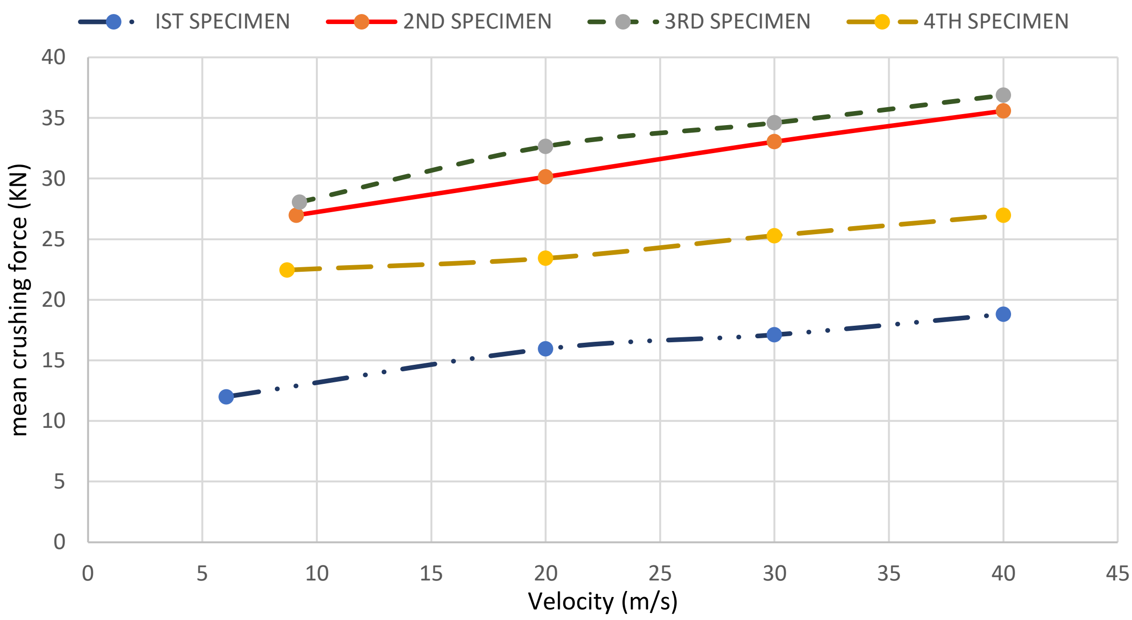

Figure 6. 24: Mean crush force - velocity curve for all four (4) specimen

Figure 6.23 shows that specimen 2 consistently has the highest initial peak force for all the velocity levels. This indicates that the geometrical parameters of specimen 2 will always yield a high initial peak force irrespective of the velocity and it will increase as the velocity increases. While specimen 4 appears to have the lowest initial peak force for all velocity levels and has little increase as the velocity increases and this can be attributed to the geometry of specimen 4 because all the specimen are made of same materials.

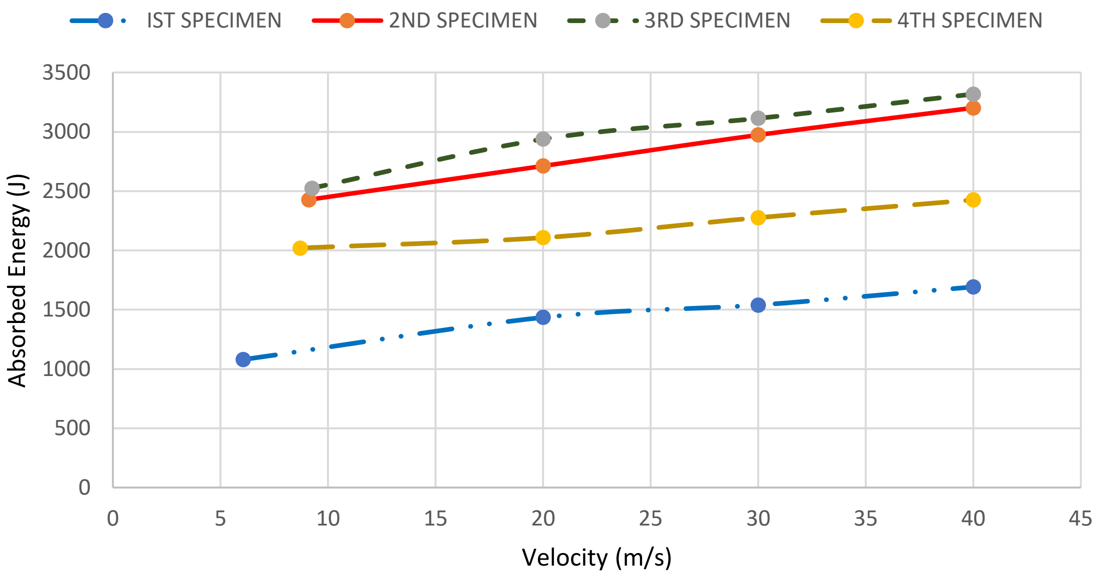

Figure 6. 25: Absorbed energy - velocity curve for all four (4) specimen

One of the obvious geometrical characteristics of specimen 4 is the large semi apical angle. This shows that semi apical angle has a large role in the effect of the initial peak force of crash boxes because it enables a quick and uniform collapse behavior of the specimen.

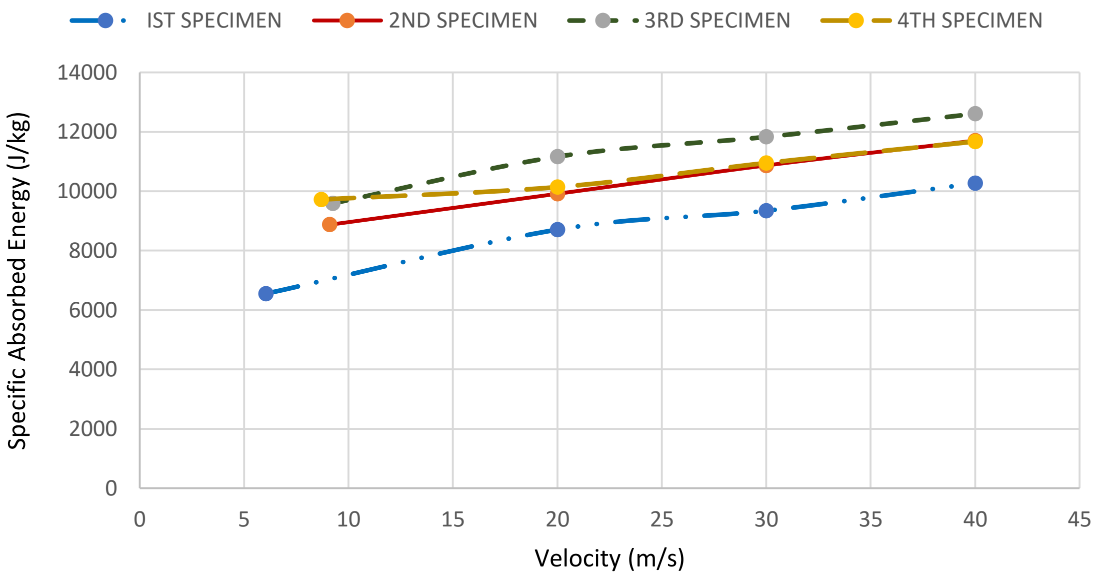

Figure 6. 26: Specific absorbed energy - velocity curve for all four (4) specimen

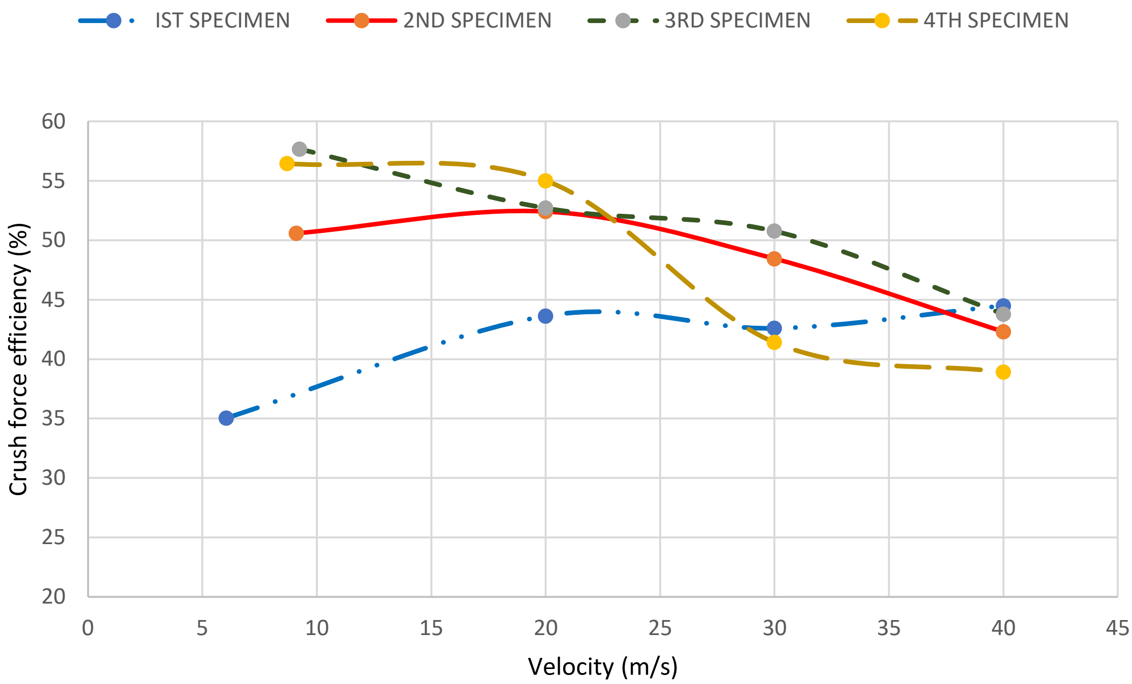

Figure 6. 27: Crush force efficiency - velocity curves for all four (4) specimen

An understanding of the percentage change in performance parameters of the crash box is important and vital to this study. Therefore, Table 6.2 highlights the percent change in performance of the specimen as they are tested under four (4) different speeds.

The change is calculated using the corresponding parameter at the initial simulation speed (6.05, 9.1, 9.25 and 8.7 m/s for specimen 1, 2, 3, and for respectively) and final simulation speed (40 m/s) using Equation 6.1 shown below.

$$\% \text{ Change} = \frac{\text{Final Value} - \text{Initial Value}}{\text{Initial value}} \text{ X } 100\% \qquad (6.1)$$

Table 6. 2: Percent change of crushing parameters with increased velocity

	SPECIMEN 1	SPECIMEN 2	SPECIMEN 3	SPECIMEN 4
Initial peak force % change	23.5	23.95	23.3	4.3
Absorbed energy % change	56.73	31.90	31.41	20.095
SEA % change	56.73	31.90	31.41	20.095
mean force % change	56.73	31.90	31.41	20.095
CFE % change	26.95	-16.35	-24.07	-31.08

6.7 Discussion of results

From the simulations, it is observed that the specimens plastically deform progressively in their axial direction beginning from the points of impact as seen in Figure 5.33 – 5.35. All the specimen were observed to undergo similar pattern of plastic deformation and folding.

From the force – displacement curves shown in Figure 6.1 – 6.4, it is observed that for all the specimen, before an initial peak force was reached, the material behaved elastically until a peak force was reached which an immediate rapid drop of force was observed, these regions are usually between 3mm to 5mm displacement for all the specimen. The rapid dropping is also followed by subsequent peaking of the forces which connotes post crumbling phases that follows due to the mode of collapse of the specimen.

Specimen 2 is observed to have the highest peak load consistently for all the velocity levels analyzed, as shown in Figure 6.23.

Specimen 4 is observed to have the lowest peak force level consistently for all the levels of impact velocity analyzed. This is due to the smaller top dimension where the moving wall impacts, therefore the crash box required less force to initiate a deformation.

A high initial peak force demands that more force needs to be exerted on the crash box before it can deform plastically. This is not really desirable in crash box designs as the initial peak force needs to be as small as possible to prevent a force transfer to the vehicle occupant compartment.

From Table 6.2, specimen 2 has the highest initial peak force increase of about 23.95% between a speed test of 9.1m/s to 40m/s.

The velocity – time graphs (Figure 6.17-6.20) showed that at speeds lower than 10m/s, the crash boxes experiences a decreasing velocity as the crush proceeds until the targeted point of termination. But for speed levels higher than 10m/s, the specimens experienced a sudden collapse mode, hence there are little or no reduction in the impact velocities until the crushing process is completed to the end.

The energy – displacement curves (Figure 6.1 – 6.4) shows that for all the specimens, an increased velocity yield an increase in absorbed energy. This assertion is confirmed using Figure 6.25 to visually assess the behavior of the specimens in absorbing energy as the speed increases. This is logically acceptable because as the speed increases, the momentum increases which yields more kinetic energy available for absorption. This shows that as the speed increases, the specimens will keep absorbing energy until they reach their energy absorption limit which is a factor of material property and geometry.

According to the absorbed energy – velocity curve shown in Figure 6.25 and Figure 6.26, specimen 3 has a superior performance in absorbing energy. But as regards to crush force efficiency, specimen 3 has superior performance while specimen 1 has the poorest performance at low speeds but as the impact velocity increases to about 40m/s specimen 1 showed a superior performance while specimen 3 is next in performance. The change in crush force efficiency for all the specimen studied dropped as the impact velocity increases except for specimen 1. The following points are observed.

1. Energy absorption increased slightly, this slight increase is expected due to the material property of the mild steel. Only strain rate dependent material properties may change the energy absorption (Strain hardening). The rupture of the structure didn’t allow greater energy levels.
2. The loads increased as the impulse increased due to higher impact velocity. The increase is about 30% which is tolerated for injury. Further improvement of the designs and materials may lead to lower levels of peak loads.

3. Specimen 3 gave superior performance in energy absorbed, specific energy absorbed, and mean load. Specimen 3 gave the second best performance as regards to CFE at high impact velocities.

CHAPER 7
CONCLUSION

This study has established an analytical solution to understanding the relationship of velocity to the performance of crash boxes. It reveals that the performance of crash boxes is affected by velocity, as seen in previous chapter. The peak loads for all the specimen has an increment within the range of 4 to 24% (Table 6.2) from low speeds to high speeds.

An increase in velocity means increase in momentum which is a direct relation of impulse (the product of force with time). So as the velocity increases, momentum increases and therefore the impact force increases causing the specimen to be more resilient to deformation.

Specimen 2 appeared to have the highest peak load for all speed levels and has a 16.6% drop in crush force efficiency.

Specimen 4 has the lowest peak force with an absorbed energy within the range of 2kj to 2.5kJ (Figure 6.25). Specimen 4 experienced an adverse drop in crush force efficiency performance as the impact velocity increased and became the least effective crash box at impact velocity above 40m/s but a better performance was observed at low speeds (Figure 6.27).

Velocity has little effect on the initial peak force of specimen 4 but has obvious effect on the initial peak force of specimen 1, 2 and 3. While for specific absorbed energy and energy absorbed parameters, specimen 3 is observed to have superior performance and followed by the 4^{th} specimen in the specific absorbed energy.

On this note, it is concluded that specimen 3 is the most effective specimen under the conditions of this study. Depending on the critical factor of design, an engineer may choose either specimen 3 for energy absorption criterion or specimen 4 for superior initial force performance.

Increase in the number of crash boxes will increase the absorbed energy for higher velocities. For higher velocities it is enough to increase the number of boxes since peak load can be tolerated.

7.1 Recommendations

This study has shown that the behavior of crash boxes at high speeds shows a high degree of unreliability of only 2 crash boxes fitted in vehicles for the purpose to absorb the crash energy in the event of a crash therefore; It is recommended that the automobile be fitted with more numbers of crash boxes to increase the possibility of higher levels of energy absorption.

Thicker crash boxes with lightweight materials are recommended for better energy absorption performances.

7.2 Draw Back of Present Study

The present study had the following challenges and draw backs listed below;

a. Unavailability of funds for experimentation
b. Unavailability of an excellent processing machine (Computer) for simulations.
c. Advance knowledge of the software and programs used in this study.
d. Insufficient advance knowledge of crash mechanics

7.3 Future Studies

a. Further study can be done to evaluate and find an optimum design geometry between specimen 3 and specimen 4 for combined superior performance.
b. A change of material, materials like aluminum are good candidates.
c. A change of geometrical parameters such as the cross section, change from Square to circular
d. Increase the thickness of the walls of the tubes.
e. Use filler materials to fill the void of the tubes.

REFERENCES

A. Taştan, E. Ü. (2016). Optimum Crashworthiness Design Of Tapered Thin Walled Tubes With Lateral Cutouts. *Thin Walled Structures*, 543-553.

A.G. Mamalis, D. M. (2001). Finite Element Simulation Of The Axial Collapse Of Thin Wall Square Frusta. *İnternational Journal Of Crashworthiness*, 155-164.

A.I. RADU, C. C. (2015). Study of Current State of Crash Testing. *Engineering Sciences, 8*, 31-36. Retrieved April 27, 2019

A. Eyvan. (2014). Axial crushing behavior and energy absorption efficiency of corrugated tubes. *Materials and Design*, 1028-1038.

Altair Hyperworks. (n.d.). *Hypermesh Overview and Capabilities*. Retrieved from Altair Hyperworks: https://altairhyperworks.com/product/hypermesh

ANCAP. (2018). *Safety Testing Explained*. Retrieved from ANCAP SAFETY: https://www.ancap.com.au/safety-testing-explained

College of Engineering and Applied Science. (n.d.). Retrieved from http://www.colorado.edu/engineering/CAS/courses.d/IFEM.d/: http://www.colorado.edu/engineering/CAS/courses.d/IFEM.d/

Crash Test: Vehicle Safety and Accident Prevention. (2019, April 27). *History of Car Safety*. Retrieved from Crash Test : http://www.crashtest.org/history-car-safety

Dassault Systemes. (n.d.). *CATIA shape the world we live in*. Retrieved from Dassault Systemes: https://www.3ds.com/products-services/catia/

E. Acar, M. A. (2011). Multi-objective crashworthiness optimization of tapered thin-walled tubes with axisymmetric indentations. *Thin-Walled Structures* , 94-105.

G.M Nagel, D. P. (2004). Dynamic Simulation and Energy Absorption of Tapered Tubes Under Impact Loading . *International Journal of Crashworthiness*, 389-399.

GetData Graph Digitizer. (n.d.). *About GetData Graph Digitizer*. Retrieved from GetData Graph Digitizer Web site: http://getdata-graph-digitizer.com/

Guohua Zhu, Z. W. (2017). Experimental And Numerical İnvestigation İnto Axial Compressive Behaviour Of Thin Walled Structures Filled With Foams And Composite Skeleton. *İnternational Journal Of Mechanical Sciences*, 104-119.

Isabel Duarte, M. V.-O. (2015). static and dynamic axial crush performance of in-situ foam filled tubes. *Composite structures*, 128-139.

LSTC. (n.d.). *About Ls-Dyna*. Retrieved April 27, 2019, from Livermore Software Technology Corporation: http://www.lstc.com/products/ls-dyna

M. Costas, D. M. (2016). Axial crushing of aluminum extrusions filled with PET foam and GFRP. *Thin Walled Structures*, 45-57.

Mahshid Mahbod, M. A. (2018). Energy Absorption Analysis Of A Novel Foam Filled Corrugated Composite Tube Under Axial And Oblique Loadings. *Thin Walled Structures*, 58-73.

Mehmet A. Guler, M. E. (2010). The Effect Of Geometrical Parameters On The Energy Absorption Characteristics Of Thin Walled Structures Under Axial İmpact Loading. *International Journal of Crashworthiness*, 377-390.

Mohan, P. (n.d.). *Introduction to Vehicle Crashworthiness.* Retrieved from CRASH: http://crash.ncac.gwu.edu/pradeep/lecture2.html

Murat Altin, Ü. K. (2017). Investigation of combined effects of cross section, taper angle and cell structure on crashworthiness of multi-cell thin walled tubes. *International Journal of Crashworthiness*.

Murat Altin, Ü. K. (2017). Investigation of combined effects of cross section, taper angle and cell structure on crashworthiness of multi-cell thin-walled tubes. *International Journal of Crashworthiness*.

Sami E. Alkhatib, F. T. (2017). Collapse behaviour of thin walled corrugated tapered tubes. *Engineering Structures*, 674-692.

T. Hirano, A. Y. (1980). *U.S.A Patent No. 4 190 276.*

world health organızatıon . (2019, april 26). *vıolence and ınjury preventıon: global status report on road safety 2018*. Retrieved from world health organızatıon : https://www.who.int/violence_injury_prevention/road_safety_status/2018/en/

X. Zhang, H. Z. (2013). Energy absorption of multi-cell stub columns under axial compression. *Thin-Walled Structures*, 156-163.

Y Nakazawa, K. T. (2005). Development of crash box for passenger car with high capability for energy absorption. *8th International Conference on Computational Plasticity,* (pp. 577-580). Barcelona, Spain.: COMPLAS VIII, CIMNE.

Y. Xiang, M. W. (2014). Key Performance Indicators of Tubes and Foam filled Tubes used as energy absorbers. *thin walled structure*.

Z. Kazanci, K. B. (2012). Crushing and crashing of tubes with implicit time integration. *International Journal of Impact Engineering* , 80-88.

Zonghua Zhang, S. Z. (2011). comparisons of honeycomb sandwich and foam-filled cylindrical columns under axial crushing loads. *thin walled structures*, 1071-1079.